DLR-IB-RM-OP-2017-115

# High Fidelity Modelling for High Altitude Long Endurance Solar Powered Aircraft

## Master's Thesis

Jongseok Lee

Deutsches Zentrum
für Luft- und Raumfahrt

|  |  |
|---|---|
| Institut für Robotik und Mechatronik | BJ.: 2017<br>DLR-IB-RM-OP-2017-115 |

# MASTERARBEIT

# HIGH FIDELITY MODELLING FOR HIGH ALTITUDE LONG ENDURANCE SOLAR POWERED AIRCRAFT

|  |  |  |
|---|---|---|
| Freigabe: | Der Bearbeiter: | Unterschriften |
|  | Jongseok Lee |  |
|  | Betreuer: |  |
|  | Tin Muskardin<br>Dr. Konstantin Kondak |  |
|  | Der Institutsdirektor |  |
|  | Dr. Alin Albu-Schäffer |  |

Dieser Bericht enthält 86 Seiten, 56 Abbildungen und 20 Tabellen

|  |  |  |  |
|---|---|---|---|
| Ort: Oberpfaffenhofen | Datum: 13.11.2017 | Bearbeiter: Jongseok Lee | Zeichen: |

Eidgenössische Technische Hochschule Zürich
Swiss Federal Institute of Technology Zurich

Autonomous Systems Lab
Prof. Roland Siegwart

Master Thesis

# High Fidelity Modelling for High Altitude Long Endurance Solar Powered Aircraft

**Autumn Term 2017**

**Supervised by:**
Tin Muskardin & Dr. Konstantin Kondak
Philipp Oettershagen & Thomas Stastny

**Author:**
Jongseok Lee

# Declaration of Originality

I hereby declare that the written work I have submitted entitled

**High Fidelity Modelling for High Altitude Long Endurance Solar Powered Aircraft**

is original work which I alone have authored and which is written in my own words.[1]

**Author(s)**

| | |
|---|---|
| Jongseok | Lee |

**Student supervisor(s)**

| | |
|---|---|
| Philipp | Oettershagen |
| Thomas | Stastny |

**Supervising lecturer**

| | |
|---|---|
| Roland | Siegwart |

With the signature I declare that I have been informed regarding normal academic citation rules and that I have read and understood the information on ’Citation etiquette’ (`https://www.ethz.ch/content/dam/ethz/main/education/rechtliches-abschluesse/leistungskontrollen/plagiarism-citationetiquette.pdf`). The citation conventions usual to the discipline in question here have been respected.

The above written work may be tested electronically for plagiarism.

Place and date

Signature

---

[1] Co-authored work: The signatures of all authors are required. Each signature attests to the originality of the entire piece of written work in its final form.

# Contents

**Preface** v

**Abstract** vii

**Symbols** ix

**1 Introduction** 1
- 1.1 Background and motivation 1
- 1.2 Objectives and scope 2
- 1.3 Flying robots 3
- 1.4 Outline of the thesis 5

**2 Local Aircraft System Identification for Elektra 1** 7
- 2.1 Data gathering 8
- 2.2 Nonlinear flight path reconstruction 11
  - 2.2.1 Process and measurement models 11
  - 2.2.2 Forward and backward extended Kalman filter 14
  - 2.2.3 Iterative extended Kalman smoothing - offline 16
  - 2.2.4 Iterative extended Kalman smoothing - online 17
  - 2.2.5 Results of flight path reconstruction 18
- 2.3 Aerodynamic model identification 20
  - 2.3.1 Linear aerodynamic model identification 20
  - 2.3.2 Nonlinear aerodynamic model identification 22
- 2.4 Aerodynamic model validation 23
  - 2.4.1 Linear model validation 23
  - 2.4.2 Nonlinear model validation 27
- 2.5 Limitations and future works 30

**3 System identification tool box and its application to Penguin BE** 33
- 3.1 Overview of two step method 33
- 3.2 System Identification tool box 34
- 3.3 Penguin BE local system identification 36
  - 3.3.1 Data gathering 37
  - 3.3.2 Reconstruction of path 38
  - 3.3.3 Parameter identification and validation 40
- 3.4 Limitations and recommendations 44

**4 Global Aircraft System Identification for Elektra 1** 45
- 4.1 Incremental model update scheme 46
- 4.2 Flight test design and data gathering 48
- 4.3 Parameter identification with VLM simulation 48
- 4.4 Correction model identification 50
- 4.5 Correction model validation 54

4.6 Limitations and future works . . . . . . . . . . . . . . . . . . . . . . . 59

**5 Conclusion** **61**

**Bibliography** **66**

**A Supplementary materials** **67**
A.1 More results on Elektra 1 path reconstruction . . . . . . . . . . . . . . 67
A.2 Penguin BE UAV local system identification . . . . . . . . . . . . . . . 68

**B Project definition** **71**

# Preface

This master thesis research has been conducted within flying robots group at Robotics and Mechatronics Center (DLR) as an external master thesis. First and foremost, I would like express my gratitude to Dr. Konstantin Kondak for accepting me as a peer and supporting me during my stay at DLR. I also owe so much to Dipl. Tin Muskardin for being an excellent supervisor. I learned a lot from the countless discussions and meetings. Furthermore I would like to sincerely thank my ETH supervisors Philipp Oettershagen and Thomas Stastny for many discussions and ideas despite the long distance. I could not have realized this thesis without them and I learned a great deal from them.
I would like to express my gratitude to the supervising professor Prof. Roland Siegwart for the encouragement at both the intermediate and the final defence. My gratefulness also goes to Dr. Christian Ott, the head of "Analysis and Control of Advanced Robotic Systems" department and Prof. Alin Albu Schaffer, the director of "Institute of Robotics and Mechatronics".
Most importantly I would like to thank my family and friends for the encouragement and love during my studies. I feel so fortunate for the every interactions and bonds I had and will be having with them.

# Abstract

High Altitude Long Endurance (HALE) platforms are the aerial platforms capable of flying in the stratosphere for long periods of time. This master thesis presents aircraft system identification procedures geared towards such fixed wing platforms where aerodynamic forces and moments are parametrically modelled with so-called stability and control derivatives. The first part of the thesis addresses local system identification procedures intended for controller synthesis at low altitude flights whereas the second part of the thesis deals with a preliminary study on a new global system identification method.

The local system identification procedure is based on the two step method, which offers flexibility regarding the aerodynamic structure. Therefore, it is suitable for the development of a system identification tool chain for various fixed wing platforms. Various system identification experiments have been conducted to collect flight test data. The parameters for the estimation of aerodynamic forces and moments are then found through an optimization procedure. Such parameters have been validated using a validation set from flight test data and their applicability for controller synthesis has been demonstrated.

Global system identification typically requires the collection of flight test data at multiple points in the flight envelope and often, is combined with extensive Computational Fluid Dynamics (CFD) solutions as well as wind-tunnel experiments. Such an approach is time consuming and costly. This thesis presents a new method to overcome the limitations of the current methodology by applying a parameter search on VLM-based (Vortex Lattice Method) dynamic simulations of aircraft system identification manoeuvres and correcting the estimated models with available flight test data. The current study shows improvements in fidelity with decrease in Root Mean Squared Error (RMSE) by factor 0.2 and 0.5 for x-axis and z-axis forces in body frame respectively, while reducing the effort for obtaining a model with similar fidelity.

# Symbols

## Symbols

| | |
|---|---|
| $u, v, w$ | x-axis velocity, y-axis velocity, z-axis velocity |
| $p, q, r$ | roll, pitch and yaw rates |
| $\phi, \theta, \psi$ | roll, pitch and yaw angle |
| $X, Y, Z$ | x-axis force, y-axis force, z-axis force |
| $L, M, N$ | x-axis moment, y-axis moment, z-axis moment |
| $h$ | altitude |
| E[ ] | expectation operator |
| $x_{AP}$ | measured state x from airdata probe |
| $x_{est}$ | estimated state x |
| $x_{GPS}$ | measured state x from GPS |
| $x_{KF}$ | estimated state x from Kalman filter |
| $x_{IMU}$ | measured state x with IMU |
| $x_m$ | measured state x |

## Acronyms and Abbreviations

| | |
|---|---|
| AP | Air-data Probe |
| CFD | Computational Fluid Dynamics |
| DLR | Deutschen Zentrums für Luft- und Raumfahrt |
| HALE | High Altitude Long Endurance |
| ETH | Eidgenössische Technische Hochschule |
| EKF | Extended Kalman Filter |
| GOF | Goodness Of Fit |
| GPS | Global Positioning System |
| IEKF | Iterative Extended Kalman Filter |
| IEKS | Iterative Extended Kalman Filter and Smoother |
| IMU | Inertial Measurement Unit |
| NRMSE | Normalised Root Mean Squared Error |
| RMSE | Root Mean Squared Error |
| TIC | Theil's Inequality Coefficient |
| UAV | Unmanned Aerial Vehicle |
| VLM | Vortex Lattice Method |
| WV | Wind Vane |

# Chapter 1

# Introduction

This thesis was accomplished within the Flying Robots Group of the Robotics and Mechatronics Center at DLR in collaboration with the Fixed Wing Aerial Robotics Group of the Autonomous Systems Lab at ETH Zurich

Within the flying robots group at Robotics and Mechatronics Center, research has been focusing on fixed wing solar electrical platforms capable of stratospheric flight for a long period of time. These High Altitude Long Endurance (HALE) platforms have potential to provide an alternative solution to satellite technologies by operating above the clouds at a lower cost than satellites while offering flexibility and maintainability. Thus, the future applications for these platforms can possibly range from mobile communication networks to long term observations and environmental measurements [1]. Elektra 2 in figure 1.1 is an example of such HALE platforms. The topic of this master thesis is high fidelity aerodynamic modelling via aircraft system identification for such fixed wing platforms.

## 1.1 Background and motivation

System identification has been chosen as the primary tool for high fidelity modelling of HALE platforms. Aircraft system identification is the process of building mathematical models of an aircraft based on measurements. The typical aircraft system identification problem involves determining the mathematical models of aerodynamic forces and moments by identifying unknown aerodynamic parameters from measurements of inputs and outputs. The outcome of the aircraft system identification is a model valid over a known region in the flight envelope with specific uncertainty bounds. Due to the nature of the approach where traditional modelling techniques are combined with data from real flight, aircraft system identification tends to result in a highly accurate model.

The main motivation for the current project stems from practical considerations of field robotics where the gap between the theory and practice is being challenged. Currently, the Flying Robots Group uses a flight dynamics model from geometry based approach where the aerodynamic database is created using the vortex lattice method(VLM) [3]. However, the low fidelity of this type of dynamic model limits its usage in controller synthesis, as the model offset from reality is typically too great for robust offline tuning of control parameters which can then be useful in flight. Consequently, the tuning of the control parameters is done manually in flight which often consumes weeks of flight experiments. More importantly, HALE platforms have wide ranges of operation and therefore, gain scheduling over different regions of flight envelope is perhaps required. Thus, manual in-flight tuning may not be a feasible option. In summary, the main motivation for a high fidelity aerodynamic

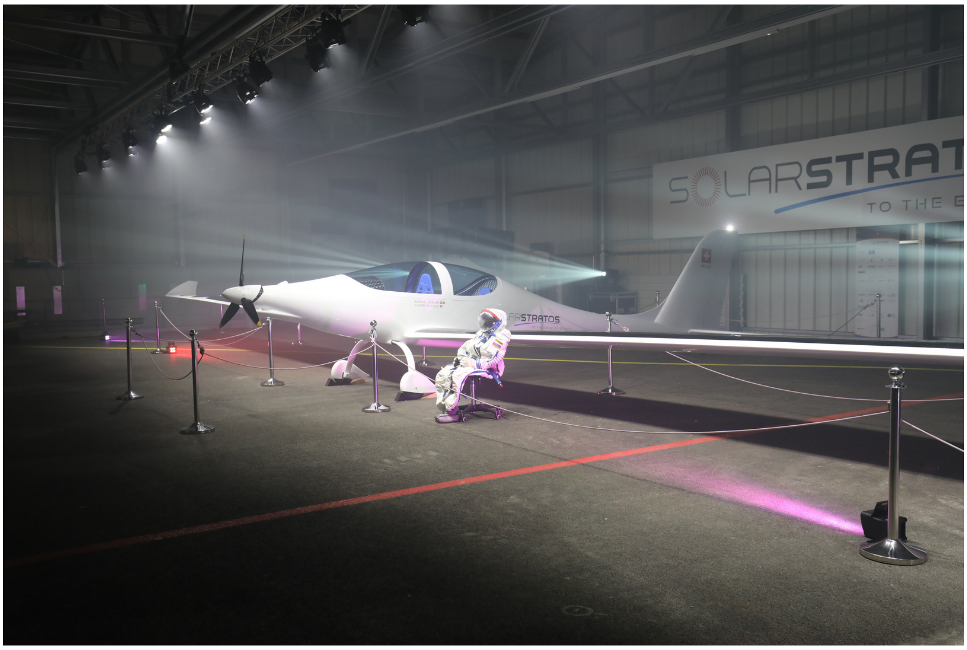

Figure 1.1: Elektra 2 from SolarStratos roll out [2].

model is reducing the amount of effort or even avoiding the in-flight tuning of the control parameters.

Additionally, high fidelity models of fixed wing platforms can be integrated into on going research for HALE platforms at DLR. In particular, simulation of stratospheric mission and model based control for landing on moving platforms [4, 5] are important milestones for research on HALE platforms. In close cooperation with Elektra Solar GmbH (a spin-off from DLR) and SolarXplorers SA (project SolarStratos [2]), the flying robots group is involved in the development of highly efficient drives, avionics components, payloads and autonomy functionalities for autonomous and optionally piloted solar high-altitude platforms and missions including the development of manned solar aircraft, called Elektra 2, for stratospheric flight. The initial verification of such developments require simulation of stratospheric mission. Furthermore, high fidelity model of the aircraft can be used to improve the landing of aerial vehicles on the moving platforms - a novel landing system that can increase payload capacity and operation availability of HALE platforms by removing the landing gear.

## 1.2 Objectives and scope

The main objective of current study is the development of a high fidelity aerodynamic model and modelling procedures which can reduce the amount of effort or even avoid in-flight tuning of the control parameters for HALE platforms. Accomplishment of this objective requires solving following challenges or sub-objectives.

- Local system identification to obtain a mathematical model of high fidelity level for HALE platforms which is valid over one region of flight envelope.

- Global system identification to obtain a mathematical model of high fidelity level for HALE platforms which is valid over the entire flight envelope.

Local aircraft system identification is a well defined research area where typical challenges arise from practice due to differences in system specifications and reliability. In this line of argument, application of aircraft system identification techniques to different fixed-wing platforms offers different practical challenges. In the context of current project, a locally valid mathematical model of an aircraft must serve as a first step towards high fidelity modelling for HALE platforms that is valid globally and can be of practical use for controller synthesis.

Typical global system identification involves gathering of data at multiple points of flight envelope, mainly with respect to altitude and mach number. Yet, such approach is time consuming and costly as it requires series of long flight test campaign. An alternative is incremental model update where aerodynamic database from the wind tunnel is updated with available flight test data in which the functional dependencies between different aerodynamic sources are mapped through polynomial expressions. Such methods are limited in its usage as extensive wind-tunnel tests and CFD computation with highest fidelity levels are required. The main challenge in the current project is to combine recent advances in system identification and dynamic CFD simulations to reduce the development time and efforts.

Currently, HALE platforms are not available for flying at DLR and therefore the fixed wing platforms in this master thesis research are limited to Elektra 1 and Penguin UAV where longitudinal motion of Elektra 1 would be the main subject for local and global system identification. Furthermore no high altitude flights are conducted which limits the scope to low altitude. Yet, current research must serve as a first step towards stratospheric flight for HALE platforms such as Elektra 2 as the methods being developed in this project must be validated at low altitudes first with readily available platforms. Within the scope of the thesis the global identification methods are applied to operating points outside the "nominal" flight conditions which were used to derive the model, but still constrained at low altitude. In others words, low altitude flight with variations in true airspeed were used to study the overall concept by applying the methods to other velocity points in the flight envelope.

## 1.3 Flying robots

Elektra 1 [6] is a single seat, solar powered composite aircraft developed by Elektra Solar GmbH with high aspect ratio of 14.70 (see figure 1.2). The main geometric parameters of Elektra 1 are: MTOW = 300kg, wing area S = 8.2m$^2$, wing span b = 13m and the mean aerodynamic chord c = 0.81m. The moment of inertia has been provided by the manufacturer. Elektra 1 is equipped with various sensors for its optionally piloted mode and measurements for system identification. In particular MTi 100-series provide complete MEMS based IMU, VRU, AHRS and GNSS where it provides acceleration and angular rate measurements in addition to magnetometer measurements to estimate the orientation of the aircraft. GNSS provides latitude, longitude and altitude measurements. Additionally, PSS-8 airdata probes located at the right wing provides measurements for true airspeed. Overall measurements are available at 50Hz whereas IMU measurements are sampled at 400Hz respectively. The aircraft has commonly used control surfaces namely aileron, elevator and rudder while thrust is provided by an electric motor driving a propeller. Wireless LAN is used for communication with the ground station. The software for the real time computer running QNX Neutrino RTOS is automatically generated from MATLAB/Simulink models through auto-code generation.

Penguin BE [7] in figure 1.3 is an electric UAV from UAV Factory Ltd. with a high wing and negative V-tail configuration. The main geometric parameters of Penguin UAV are: MTOW = 21.5kg, wing area S = 0.841m$^2$, wing span b = 3.298m and

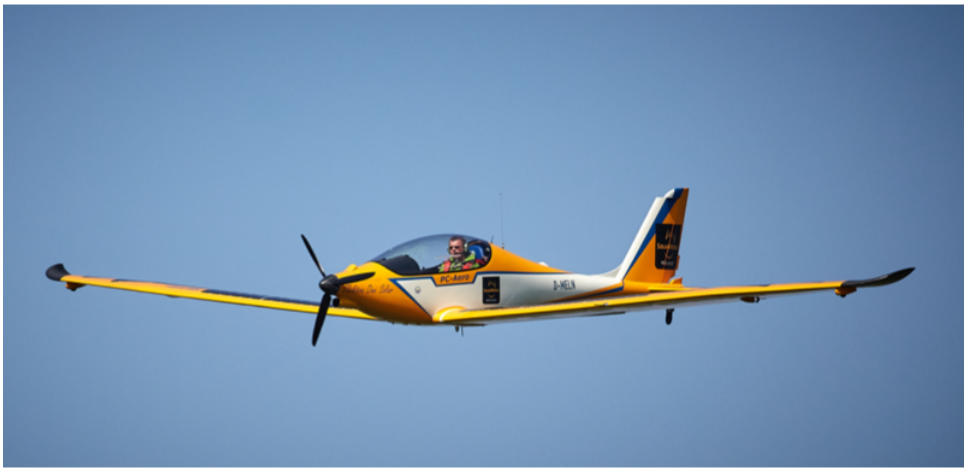

Figure 1.2: Elektra 1 in flight

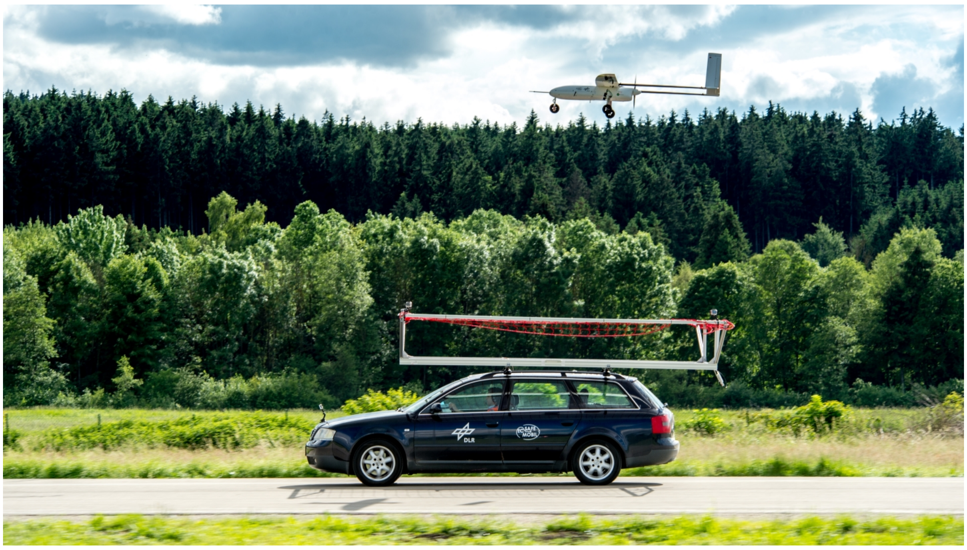

Figure 1.3: Penguin UAV landing on the moving car

the mean aerodynamic chord c = 0.32m. The mass and the moment of inertia were computed using mass point measurements. Penguin BE is the aerial platform for the research on novel landing systems and thus, the UAV is equipped with various sensors by DLR for navigation and control. Particularly, Penguin UAV is equipped with 3DM-Gx3-25 IMU from MicroStrain, PSS-8 airdata probe and Novatel FlexPak6 RTK receiver and antenna. 3DM-Gx3-25 IMU collects linear acceleration, angular velocity and orientation of the aircraft at the sample rates of 100 Hz whereas PSS-8 airdata probe located near the tip of the fuselage, measures true airspeed and temperature at the sampling rate of 20 Hz. Highly accurate differential GPS from NovAtel collects latitude, longitude and altitude measurements at the rate of 20 Hz. Overall, the measurements are available at 20Hz. The UAV has aileron and ruddervator (negative V-tail) for its control surfaces while the trust is provided by a geared brushless DC motor with 19×11 inch propeller in push configuration. Similar to Elektra 1, wireless LAN is used for communication with the ground station and the software for the real time computer is automatically generated from

MATLAB/Simulink models through auto-code generation.

## 1.4 Outline of the thesis

Chapter 2 presents the local aircraft system identification for Elektra 1. The description of the local system identification toolbox can be found in chapter 3 where its application to Penguin BE is highlighted. The chapter 4 presents the global aircraft system identification for Elektra 1.

# Chapter 2

# Local Aircraft System Identification for Elektra 1

This chapter presents the local aircraft system identification applied to symmetric motion of Elektra 1. The result of the local aircraft system identification is a parametrized aerodynamic model which is valid over the neighborhood of the known region or trim point where the data has been gathered. The development of a mathematical model with sufficient fidelity for Elektra 1 would facilitate not only controller synthesis and nonlinear flight simulation at low altitude, but also serve as a stepping stone towards the global system identification and consequently, an assistance to gain-scheduling and simulation of the entire stratospheric mission.

The two step method is an equation error method in the time domain where the external force and moment acting on the aircraft are reconstructed from flight data (step one) and the aerodynamic derivatives are identified by applying the least squares method on the reconstructed force and moment (step two). This method does not involve the minimization of errors which are directly computed from the aircraft states. The advantages of two step method over output and filter error methods are (1) flexibility for the selection of the nonlinear aerodynamic model structure [8, 9, 10] (the equation error approach allows rapid investigation of various model structures through the linear projection of feature space in optimization process [8, 10]) and (2) extensibility to incremental model update scheme. Moreover, studies have shown that the accuracy of aerodynamic models from these approaches yield comparable results to the output error method [11]. Yet its optimization through the least squares method is susceptible to the noise and therefore, two step method requires both estimation and smoothing of the aircraft states, force and moment through extensive data compatibility check [10]. A frequency domain approach has not been considered due to the difficulty in producing chirp and Pseudo Random Binary Sequence (PRBS) signals for manned aircraft. Furthermore, time domain methods are the most appropriate and direct when one is looking for real time physical parameter estimates for the nonlinear aerodynamic models. [10]

Local aircraft system identification is a well defined research area and there are several well regarded texts on aircraft system identification. Among them, [10] is one of the widely accepted text for time domain approaches and is used as a main reference for this work. Additionally, an overview and theoretical foundations can also be found in [12, 13] whereas practical examples of two step method can be found [9, 8]. Yet, typical challenges in aircraft system identification stem from differences in system specifications and reliability [12, 10]. Therefore, the main contribution of the work presented in this chapter is application of two step method to a new aerial platform Elektra 1, and development of a custom tool chain for

aircraft system identification within the Flying Robots Group for their research on HALE platforms.
The experiment design (section 2.1), application of the two step method (section 2.2 and 2.3), validation of the aerodynamic model (section 2.4), limitations and recommendations (section 2.5) are presented sequentially in this chapter.

## 2.1 Data gathering

An overview of data gathering from designing and performing the experiments, and recording of system inputs and outputs can be found in [10, 12]. The conventions are as follows: $u$ and $w$ are the x-axis and z-axis linear velocities along the body axes. $q$ is the y-axis angular velocity about the body axes and de is the elevator deflection. The angle of elevator deflection is defined positive when its trailing edge is deflected upwards. $X$ and $Z$ are x-axis and z-axis force along the body axes whereas $M$ is y-axis moment around the body axes.

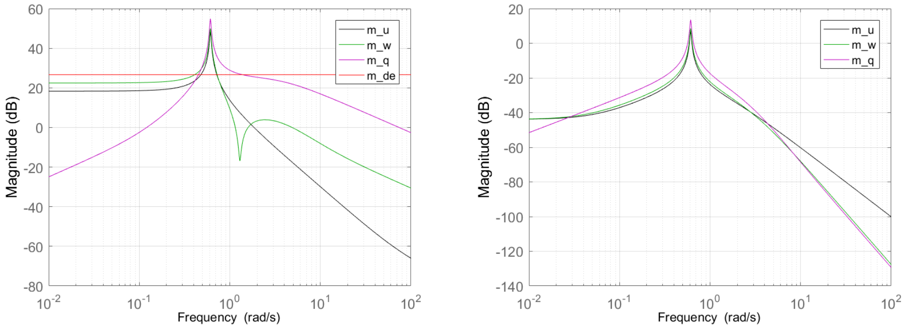

Figure 2.1: Pitching moment derivatives w.r.t elevator (left) and throttle (right)

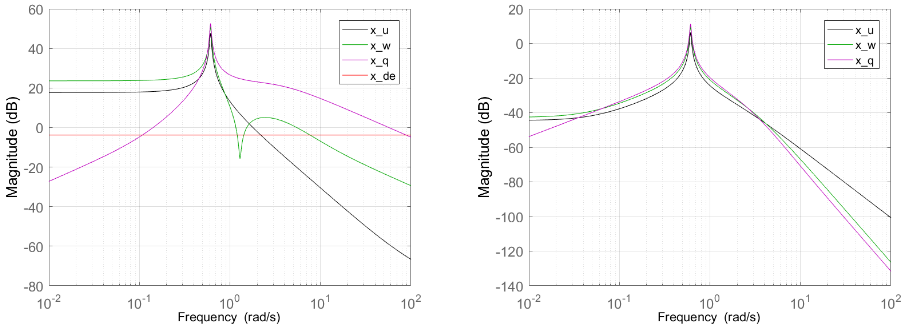

Figure 2.2: X-axis force derivatives w.r.t elevator (left) and throttle (right)

The parameters to be identified are stability and control derivatives of the aircraft (see [14] for their definitions). One of the key criteria in experiment design is the collection of data that contains enough information about the parameters to be identified. In other words, such parameters must have a dominant influence in the collected time histories of the aircraft motion. According to [15] a derivative is considered identifiable when its term has a magnitude of at least 10% of the largest term's magnitude and such analysis requires frequency response magnitudes of the various parameters are plotted as a function of the input signal frequency as shown in figures 2.1, 2.2 and 2.3.

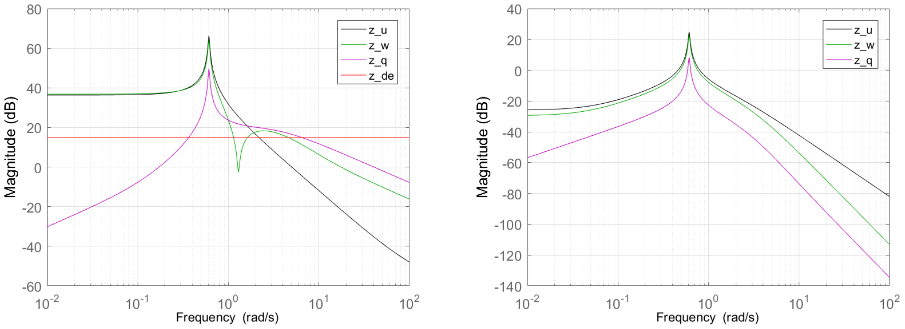

Figure 2.3: Z-axis force derivatives w.r.t elevator (left) and throttle (right)

Note that a geometry based modelling method [3] has been used to compute the a priori model of Elektra 1 aircraft. The frequency response magnitudes of the longitudinal derivatives with respect to elevator and throttle in figures 2.1, 2.2 and 2.3 have been computed from such a priori aerodynamic model with the method proposed in [10]. According to [10] the regions of identifiability typically lie between 0.1 rad/s and 1 rad/s (corresponds to phugoid) and also, between 1 rad/s and 10 rad/s. This is in alignment with the results shown in figures 2.1, 2.2 and 2.3. It can be observed from these figures that the parameters are identifiable via elevator commands with the frequencies around 0.1 rad/s and 8 rad/s, and via throttle commands with the frequencies around 2.3 rad/s. Typical time domain inputs such as pulse, DLR3211 [10] and doublet are chosen with specific time steps and magnitude such that the energy of the input signals are maximized in the region around the required frequencies. See figures 2.4, 2.5 and 2.6. Note that these inputs signals are designed taking the inaccuracies of the a priori model. Consequently the bandwidth where the energy of the input signals are maximized, are chosen in range of 0 rad/s to 2 rad/s for phugoid and 2 rad/s to 12 rad/s for short period.
The control derivative $X_{de}$ is the parameter that shows a constant negative value over all the frequencies (see figure 2.2). Furthermore $X_{de}$ is not identifiable using the designed input signals (see figures 2.4, 2.5 and 2.6 for the designed input signals). This is because its magnitude is always below 10% of the largest term's magnitude over the selected bandwidth for the input design. According to [14] $X_{de}$ represents the axial force due to the elevator which captures the contribution of the tail plane drag and lift. Assuming negligible drag of the tail plane and relatively small deflection of the elevator, the term $X_{de}$ is considered to have non-significant effect to the force in x-axis along the body axes.

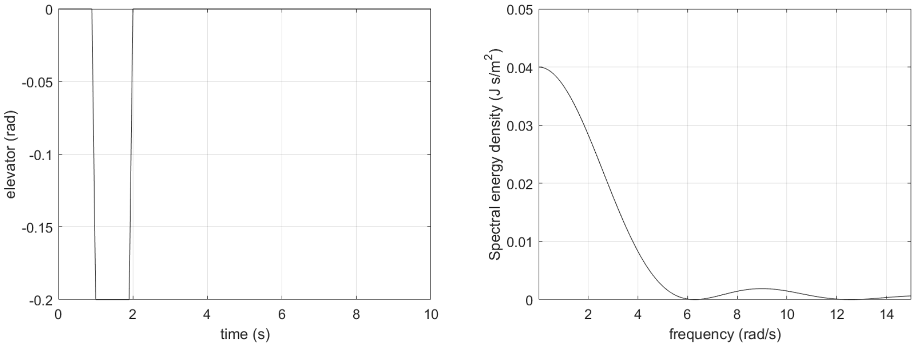

Figure 2.4: Phugoid manoeuvre - elevator (left) and energy spectrum (right)

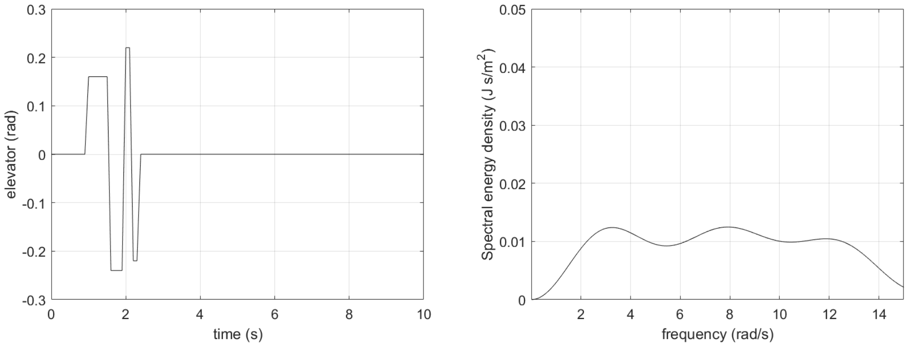

Figure 2.5: Short period manoeuvre - elevator (left) and energy spectrum (right)

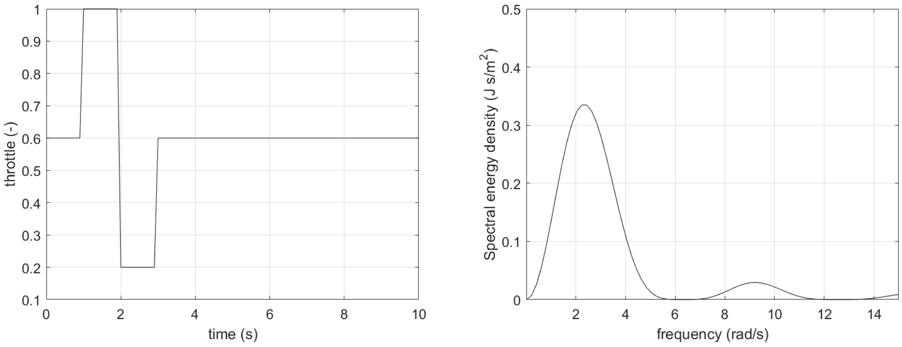

Figure 2.6: Thrust variation manoeuvre - throttle (left) and energy spectrum (right)

During the flight test the aircraft is first manually trimmed by the pilot at cruise speed under 1 km altitude. Designed control inputs are applied in open loop for the longitudinal motion. All the manoeuvres namely phugoid, short period and thrust variation are executed multiple times each in order to mitigate effects of variations in atmospheric conditions and offsets in the initial conditions. In total 3 phugoid, 2 short period and 4 thrust variation manoeuvres could be gathered. Subsets of the data are discarded based on an analysis of the influence of lateral motion on longitudinal motion. Other subsets of the data are discarded due to wrong trim settings (in case of all thrust variation manoeuvres) and wrong shape in control inputs (in case of 3211 manoeuvre). Note that deviations from the exact planned execution of the time steps of input signals can be tolerated but the shape of the signal must be kept as accurate as possible [12]. In conclusion two phugoid manoeuvres were used each, to identify and validate the locally identified model and the rest of the data set have been discarded due to inadequacy.

In summary 2 phugoid motions could be gathered for the identification and thus, the ratio between training and validation set was 5:5. This ratio is far from the ideal where the author expected to use 60% to 80% of the data for the parameter identification and 20% to 40% of the data for the model validation. Use of more data is recommended as it can attribute to more robustness in parameter identification with respect to atmospheric conditions.

Furthermore the data gathering procedure must be improved for Elektra 1. Firstly, it is recommended to turn on the autopilot to stabilize lateral motion while executing longitudinal system identification manoeuvres in open loop. This is to reduce the influence of lateral motion on longitudinal motion. Secondly, use of automation for the execution of designed input signals must be considered. Although [12, 10] recommends the manual execution of manoeuvres by the pilot the team concluded that use of autopilot is favourable for this size of manned aircraft. One of the possible solution can be a procedure where the aircraft is first manually trimmed by the pilot with a graphical assistance and a button to automatically execute the input signals is pressed.

## 2.2 Nonlinear flight path reconstruction

Flight path reconstruction or data compatibility check has three purposes namely (1) estimation of aerodynamic force and moment from measurements, (2) correction of the measurements due to sensor bias and drift, and (3) smoothing of the measurements. Since least squares for parameter identification is susceptible to noises [10] and parameters to be identified are typically aircraft stability and control derivatives that are anticipated by physical phenomena, fulfilling the above mentioned purposes is a key step to the two step method. The approach taken is called estimation-before-modelling [10, 16, 17] with optimal filtering that accounts noises in both input and output variables. In this study EKF with backward kalman smoothing (EKS), iterative EKF with backward smoothing (offline IEKS) and iterative EKF (online IEKS) have been implemented and compared. Note that the algorithms for the nonlinear flight path reconstruction is performed on the data in batch. Here, the data in batch refers to the data sets where different system identification manoeuvres (e.g phugoid 1, phugoid 2, short period 1 and so on) with slight different trim conditions. In this way the correlation between various instrumentation errors can be avoided in practice [10].

### 2.2.1 Process and measurement models

The implementation of EKF requires process and measurement model in the form of the equation 2.1 where $x(t)$ is the vector of relevant states, $u(t)$ is the vector of measured inputs, $y(t)$ and $z(t_k)$ is the vector of observations in continuous and discrete settings respectively. Lastly, $\mathfrak{w}(t)$ and $\mathfrak{v}(t_k)$ are the noises from process and measurement models at continuous time variable t and discrete time $t_k$ at step k.

$$\begin{array}{rcl} \dot{x}(t) & = & f(x(t), u(t), \mathfrak{w}(t)), \quad x(t_0) \\ y(t) & = & g(x(t)) \\ z(t_k) & = & y(t_k) + \mathfrak{v}(t_k) \end{array} \tag{2.1}$$

The relevant state vector is defined as $x(t) = [x_{ac}(t),\ \mathfrak{A}(t),\ \Theta]^T$ where the aircraft states are defined as $x_{ac}(t) = [u,\ v,\ w,\ p,\ q,\ r,\ \phi,\ \theta,\ \psi,\ h]^T$. $\mathfrak{A}(t) = [\mathfrak{A}_0,\ \mathfrak{A}_1,\ \mathfrak{A}_2]^T$ represents the vector of force and moment as the third order Gauss-Markov process where $\mathfrak{A}_0 = [X,\ Y,\ Z,\ L,\ M,\ N]^T$, $\mathfrak{A}_1 = \dot{\mathfrak{A}}_0$ and $\mathfrak{A}_2 = \dot{\mathfrak{A}}_1$. Furthermore the instrumentation error vector is $\Theta = [\Delta a_x,\ \Delta a_y,\ \Delta a_z,\ \Delta p,\ \Delta q,\ \Delta r,\ \Delta\alpha,\ \Delta\beta,\ K_{V_a}\ ]^T$ which includes biases and scaling factors for the sensors. No wind vane or 5 hole probe were attached in Elektra 1 to measure the angle of attack $\alpha$ and side slip angle $beta$. Yet an effort to make the system identification tool box as universal as possible was made and therefore, possible use of wind vane and 5 hole probe is taken into account even for Elektra 1.

The aircraft states $x_{ac}(t)$ are governed by aircraft equation of motion described in equation 2.2. The aircraft is assumed to be a rigid-body with no wind and also, equation 2.2 is expressed in the body fixed frame with its origin in the center of gravity. Elaboration on the notation is as follows: $[u, v, w, p, q, r]$ denote body axis linear and angular velocities along and about the $X_b$, $Y_b$, $Z_b$ axes at the center of gravity. The Euler angles are the orientation of aircraft (body axes) with respect to the Earth-fixed inertial reference frame (north-east-down) and are $[\phi, \theta, \psi]$ or roll, pitch and yaw angles. $h$ is the altitude from GPS which is the inertial position above the WGS84 ellipsoid or mean sea level.

$$
\begin{array}{rcl}
\dot{u} & = & -qw + rv - g\sin\theta + C_{F_x} \\
\dot{v} & = & -ru + pw + g\cos\theta\sin\phi + C_{F_y} \\
\dot{w} & = & qu - pv + g\cos\theta\cos\phi + C_{F_z} \\
\dot{p} & = & pqC_{11} + qrC_{12} + qC_{13} + C_{M_x} + C_{M_z}C_{14} \\
\dot{q} & = & prC_{21} + (r^2 - p^2)C_{22} - rC_{23} + C_{M_y} \\
\dot{r} & = & pqC_{31} + qrC_{32} + qC_{33} + C_{M_x}C_{34} + C_{M_z} \\
\dot{\phi} & = & p + q\sin\phi\tan\theta + r\cos\phi\tan\theta \\
\dot{\theta} & = & q\cos\phi - r\sin\phi \\
\dot{\psi} & = & q\sin\phi\sec\theta + r\cos\phi\sec\theta \\
\dot{h} & = & u\sin\theta - v\cos\theta\sin\phi - w\cos\theta\cos\phi
\end{array}
\tag{2.2}
$$

In the above equations $[C_{F_x}, C_{F_y}, C_{F_z}, C_{M_x}, C_{M_y}, C_{M_z}]$ are normalized force and moment with respect to mass and appropriate moment of inertia in the above equation. Note the inclusion of additional differential equations for the angular rates p, q, and r. See [18, 16, 17] for the derivation and use of such differential equations for the angular rates. Unlike the widely used equations of motion [19, 10] for angular rates the numerical differentiation of angular rates is avoided. The coefficients $C_{ij}$ for $i = 1, 2, 3$ and $j = 1, 2, 3, 4$ can be found in equation 2.3.

$$
\begin{array}{rclrcl}
C_{11} & = & \frac{I_{xz}(I_z+I_x-I_y)}{I_xI_z-I_{xz}^2} & C_{12} & = & \frac{I_z(I_y-I_z)-I_{xz}^2}{I_xI_z-I_{xz}^2} \\
C_{13} & = & 0 & C_{14} & = & \frac{I_{xz}}{I_x} \\
C_{21} & = & \frac{I_z-I_x}{I_y} & C_{22} & = & \frac{I_{xz}}{I_y} \\
C_{23} & = & 0 & & & \\
C_{31} & = & \frac{I_x(I_x-I_y)+I_{xz}^2}{I_xI_z-I_{xz}^2} & C_{32} & = & \frac{I_{xz}(I_y-I_z-I_x)}{I_xI_z-I_{xz}^2} \\
C_{33} & = & 0 & C_{34} & = & \frac{I_{xz}}{I_z}
\end{array}
\tag{2.3}
$$

In an estimation-before-modelling approach the force and moment are modeled as a third order Gauss-Markov process as shown in equation 2.4 which yields a quadratic interpolation polynomial as a function of time. One can imagine an auto-regressive process of order 3 where its polynomial coefficients are updated by the recursive algorithm at each time step. An advantage of such approach is tolerance to low measurement sampling rate and sensor noise for the construction of force and moment [20]. In equation 2.4 $\omega_{\mathfrak{A}_0}$, $\omega_{\mathfrak{A}_1}$ and $\omega_{\mathfrak{A}_2}$ are Gaussian white noises.

$$
\begin{bmatrix} \dot{\mathfrak{A}}_0 \\ \dot{\mathfrak{A}}_1 \\ \dot{\mathfrak{A}}_2 \end{bmatrix} = \begin{bmatrix} 0 & 1 & 0 \\ 0 & 0 & 1 \\ 0 & 0 & 0 \end{bmatrix} \begin{bmatrix} \mathfrak{A}_0 \\ \mathfrak{A}_1 \\ \mathfrak{A}_2 \end{bmatrix} + \begin{bmatrix} \mathfrak{w}_{\mathfrak{A}_0} \\ \mathfrak{w}_{\mathfrak{A}_1} \\ \mathfrak{w}_{\mathfrak{A}_2} \end{bmatrix}
\tag{2.4}
$$

As shown in equations 2.5 and 2.6 accelerometer biases are modelled as Markov process whereas the other instrumentation errors are assumed to be constants. Sources of biases and scaling factors for the sensors can be due to the wrong mounting of IMU and air probe, manufacturing errors, calibration errors and measurement drift from inherent characteristics of the sensors. These biases and scaling factors for the IMU and air probe are included as states of the EKF. In this way unbiased and minimum mean squared estimation of sensor biases and scaling factors is achieved where deviation of left and right hand side of equation 2.2 with respect to measurements are stochastically attributed to instrumentation errors.

$$
\begin{array}{rcl}
\dot{\mathit{\Delta} a}_x & = & -\frac{1}{\tau}\mathit{\Delta} a_x + \mathfrak{w}_{\mathit{\Delta} a_x} \\
\dot{\mathit{\Delta} a}_y & = & -\frac{1}{\tau}\mathit{\Delta} a_y + \mathfrak{w}_{\mathit{\Delta} a_y} \\
\dot{\mathit{\Delta} a}_z & = & -\frac{1}{\tau}\mathit{\Delta} a_z + \mathfrak{w}_{\mathit{\Delta} a_z}
\end{array}
\tag{2.5}
$$

In equation 2.5 $\tau$ are time constants and typically chosen between 1 and 10. The value 10 has been chosen for the current implementation. $\mathfrak{w}_{\Delta a_x}$, $\mathfrak{w}_{\Delta a_y}$ and $\mathfrak{w}_{\Delta a_z}$ are white noises associated with Markov processes. Modelling of accelerometer biases as Markov process is motivated from observability or reconstructibility analysis. See [21, 22] for the applicability of both linear and nonlinear observability analysis in selecting the instrumentation errors.

$$\dot{\Theta} = 0 \tag{2.6}$$

The vector of constant instrumentation errors $\Theta$ contain biases related to angular velocities $\Delta p$, $\Delta q$, $\Delta r$, scaling factor for true airspeed $K_{V_a}$ and biases for angle of attack and side slip angle $\Delta\alpha$ and $\Delta\beta$. All the instrumentation errors are included in the measurement equations listed below.

Define $y(t) = [u_m,\ v_m,\ w_m,\ p_m,\ q_m,\ r_m,\ \phi_m,\ \theta_m,\ \psi_m,\ h_m,\ V_{a_m},\ \alpha_m,\ \beta_m,\ a_{x_m},\ a_{y_m},\ a_{z_m}]^T$ and consequently $z(t_k) = [u_{\mathrm{GPS}},\ v_{\mathrm{GPS}},\ w_{\mathrm{GPS}},\ p_{\mathrm{IMU}},\ q_{\mathrm{IMU}},\ r_{\mathrm{IMU}},\ \phi_{\mathrm{KF}},\ \theta_{\mathrm{KF}},\ \psi_{\mathrm{KF}},\ h_{\mathrm{GPS}},\ V_{a_{\mathrm{AP}}},\ \alpha_{\mathrm{est}},\ \beta_{\mathrm{est}},\ a_{x_{\mathrm{IMU}}},\ a_{y_{\mathrm{IMU}}},\ a_{z_{\mathrm{IMU}}}]^T$. The Euler angles $\phi_{\mathrm{KF}}$, $\theta_{\mathrm{KF}}$, $\psi_{\mathrm{KF}}$ are estimated using a Kalman filter (KF) where the inherent drawbacks of accelerometer and gyroscope can be mitigated. The $\alpha_{\mathrm{est}}$ and $\beta_{\mathrm{est}}$ are estimated using their geometrical relation to body axes linear velocities assuming no wind. The works presented in [23] can also be used for computing $\alpha_{\mathrm{est}}$ and $\beta_{\mathrm{est}}$. The measurement model can be found in equations 2.7, 2.8 and 2.9.

$$\begin{array}{rcl@{\qquad}rcl}
u_m(t) & = & u(t), & u_{\mathrm{GPS}}(t_k) & = & u_m(t_k) + \mathfrak{v}_u(t_k) \\
v_m(t) & = & v(t), & v_{\mathrm{GPS}}(t_k) & = & v_m(t_k) + \mathfrak{v}_v(t_k) \\
w_m(t) & = & w(t), & w_{\mathrm{GPS}}(t_k) & = & w_m(t_k) + \mathfrak{v}_w(t_k) \\
p_m(t) & = & p(t) + \Delta p, & p_{\mathrm{IMU}}(t_k) & = & p_m(t_k) + \mathfrak{v}_p(t_k) \\
q_m(t) & = & q(t) + \Delta q, & q_{\mathrm{IMU}}(t_k) & = & q_m(t_k) + \mathfrak{v}_q(t_k) \\
r_m(t) & = & r(t) + \Delta r, & r_{\mathrm{IMU}}(t_k) & = & r_m(t_k) + \mathfrak{v}_r(t_k) \\
\phi_m(t) & = & \phi(t), & \phi_{\mathrm{KF}}(t_k) & = & \phi_m(t_k) + \mathfrak{v}_\phi(t_k) \\
\theta_m(t) & = & \theta(t), & \theta_{\mathrm{KF}}(t_k) & = & \theta_m(t_k) + \mathfrak{v}_\theta(t_k) \\
\psi_m(t) & = & \psi(t), & \psi_{\mathrm{KF}}(t_k) & = & \psi_m(t_k) + \mathfrak{v}_\psi(t_k) \\
h_m(t) & = & h(t), & h_{\mathrm{GPS}}(t_k) & = & h_m(t_k) + \mathfrak{v}_h(t_k)
\end{array} \tag{2.7}$$

Equation 2.8 assumes zero atmospheric disturbances. Additionally the biases and scaling factors are on the measurements of airdata probe (AP), estimated angle of attack and side-slip angle.

$$\begin{array}{rcl}
V_{a_m}(t) & = & K_{v_a}\sqrt{u(t)^2 + v(t)^2 + w(t)^2} \\
V_{a_{\mathrm{AP}}}(t_k) & = & V_{a_m}(t_k) + \mathfrak{v}_{v_a}(t_k) \\
 & & \\
\alpha_m(t) & = & \arctan\frac{w(t)}{u(t)} + \Delta\alpha \\
\alpha_{\mathrm{est}}(t_k) & = & \alpha_m(t_k) + \mathfrak{v}_\alpha(t_k) \\
 & & \\
\beta_m(t) & = & \arctan\frac{v_a(t)}{\sqrt{u(t)^2+v(t)^2+w(t)^2}} + \Delta\beta \\
\beta_{\mathrm{est}}(t_k) & = & \beta_m(t_k) + \mathfrak{v}_\beta(t_k)
\end{array} \tag{2.8}$$

In equation 2.9 the accelerometer measurements are expressed. The bias terms are included and the offset in the location of IMU ($x_{\mathrm{IMU}}, y_{\mathrm{IMU}}$ and $z_{\mathrm{IMU}}$) with respect to the center of gravity is corrected.

$$
\begin{array}{lcl}
a_{x_m}(t) & = & \frac{F_x(t)}{m} - (q(t)^2 + r(t)^2)x_{\mathrm{IMU}} + (p(t)q(t) - \dot{r(t)})y_{\mathrm{IMU}} \\
 & & +(p(t)r(t) + \dot{q}(t))z_{\mathrm{IMU}} + \mathit{\Delta} a_x \\
a_{x_{\mathrm{IMU}}}(t_k) & = & a_{x_m}(t_k) + \mathfrak{v}_{a_x}(t_k) \\
 & & \\
a_{y_m}(t) & = & \frac{F_y(t)}{m} - (p(t)q(t) + \dot{r}(t))x_{\mathrm{IMU}} + (p(t)^2 + r(t)^2)y_{\mathrm{IMU}} \\
 & & +(q(t)r(t) + \dot{p}(t))z_{\mathrm{IMU}} + \mathit{\Delta} a_y \\
a_{y_{\mathrm{IMU}}}(t_k) & = & a_{y_m}(t_k) + \mathfrak{v}_{a_y}(t_k) \\
 & & \\
a_{z_m}(t) & = & \frac{F_z(t)}{m} - (p(t)r(t) - \dot{q}(t))x_{\mathrm{IMU}} + (q(t)r(t) + \dot{p}(t))y_{\mathrm{IMU}} \\
 & & +(p(t)^2 + q(t)^2)z_{\mathrm{IMU}} + \mathit{\Delta} a_z \\
a_{z_{\mathrm{IMU}}}(t_k) & = & a_{z_m}(t_k) + \mathfrak{v}_{a_z}(t_k)
\end{array}
\tag{2.9}
$$

The state equations are presented where $x(t) \in \mathbb{R}^{37\times 1}$ and $y(t) \in \mathbb{R}^{16\times 1}$.

### 2.2.2 Forward and backward extended Kalman filter

A weighted combination of estimates from forward and backward Kalman filter results in smoothed estimate. In this way signals are both filtered and smoothed while reducing the inherent bias of the forward EKF estimates [24, 25]. An algorithm to combine both filtering and smoothing using EKF is addressed here. For the interested readers more details about optimal filtering and smoothing in the context of path reconstruction can be found in [10] and references therein.
In Kalman filter and smoothing the terms *a priori* and *a posteriori* refer to the estimation step k before the measurement and after the measurement k respectively in the context of forward passing. The term *smoothed* here refers to the backward pass estimation from the step N to 1. The following variables are defined.

1. A *priori* estimate of the states $\bar{x}(k) \in \mathbb{R}^{37\times 1}$.
2. A *priori* covariance $\bar{\boldsymbol{P}}(k) \in \mathbb{R}^{37\times 37}$.
3. A *posteriori* estimate of the states $\hat{x}(k) \in \mathbb{R}^{37\times 1}$.
4. A *posteriori* covariance $\hat{\boldsymbol{P}}(k) \in \mathbb{R}^{37\times 37}$.
5. A *smoothed* estimate of the states $\boldsymbol{x}^S(k) \in \mathbb{R}^{37\times 1}$.
6. A *smoothed* covariance $\boldsymbol{P}^S(k) \in \mathbb{R}^{37\times 37}$.

The Kalman filter starts with *initialization.* Then *a posteriori* followed by *a priori* is successively repeated at each time step k for all k from 1 to N. After completion of forward Kalman filter, *smoothed* is executed backward for time step k from N to 1.

#### Initialization

At time step k=0 the estimate of the states and covariance is initialized with equation 2.10 where in the formulation of Bayesian tracking problems $x_0$ is a stochastic variable with an unknown probability density function.

$$
\begin{aligned}
\hat{x}(0) =& E[x(0)] \\
\hat{\boldsymbol{P}}(0) =& E\left[(x(0) - \hat{x}(0))(x(0) - \hat{x}(0))^T\right]
\end{aligned}
\tag{2.10}
$$

In practice, initial measurements without any pre-filtering and averaging have been used for the initialization of the EKF states. These initial measurements correspond to the first data point under the trim conditions for all the system identification manoeuvres. Apart from aircraft states, the force and moment were initialized using the aircraft equations of motion (see equation 2.2). Derivatives of the force and moment, and all the measurement biases were initialized as zero. The initial covariance matrix is given in equation 2.11.

$$\hat{\boldsymbol{P}}(0) = \text{diag}\left(0.2\boldsymbol{I}_3, 0.01\boldsymbol{I}_3, 0.001\boldsymbol{I}_3, 1, 0.001\boldsymbol{I}_6, 0.01\boldsymbol{I}_6, 0.01\boldsymbol{I}_6, \boldsymbol{I}_{12}, \right) \tag{2.11}$$

### A Priori

The dynamics of state estimate $\bar{x}$ and error covariance $\bar{\boldsymbol{P}}$ at *a priori* is given by the equations 2.12 and 2.13. See equation 2.13 for the definitions.

$$\bar{x}(k+1) = \hat{x}(k) + \int_{k}^{k+1} f(\hat{x}(t), u_m(t), \theta, t)dt \tag{2.12}$$

$$\bar{\boldsymbol{P}}(k+1) = \boldsymbol{\Phi}(k+1)\hat{\boldsymbol{P}}(k)\boldsymbol{\Phi}^T(k+1) + \boldsymbol{\Psi}(k+1)\boldsymbol{B}(k)\boldsymbol{Q}(k)\boldsymbol{B}^T(k)\boldsymbol{\Psi}^T(k+1) \tag{2.13}$$

Typically the state and covariance dynamics at *a priori* is integrated from k to k+1 where the state and covariance estimate of *a posteriori* is used. MATLAB's ode45 function is utilized for the numerical integration of state and covariance dynamics. The function ode45 is based on an explicit Runge-Kutta of order (4,5) and is a single step solver. Details on numerical integration methods can be found in [10] and the references therein.

$$\begin{array}{lclclcl}
\boldsymbol{A}(k) & := & \left.\frac{\partial f(x(t),u_m(t),0)}{\partial x(t)}\right|_{x=\hat{x}(k),u_m=u(k)}, & \boldsymbol{\Phi}(k) & := & e^{\boldsymbol{A}(k)\Delta t} \\
\boldsymbol{B}(k) & := & \left.\frac{\partial f(x(t),u_m(t),0)}{\partial u(t)}\right|_{x=\hat{x}(k),u_m=u(k)}, & \boldsymbol{\Psi}(k) & := & \int_0^{\Delta t} e^{\boldsymbol{A}(k)\tau}d\tau \\
\boldsymbol{C}(k) & := & \left.\frac{\partial g(x(t))}{\partial x(t)}\right|_{x=\hat{x}(k)} & & &
\end{array} \tag{2.14}$$

In equation 2.14 the matrix $\boldsymbol{A}(k) \in \mathbb{R}^{37\times 37}$ is Jacobian matrix of the process model which is linearized around $x = \hat{x}(k)$ whereas the matrix $\boldsymbol{\Phi}(k) \in \mathbb{R}^{37\times 37}$ is the state transition matrix of the linearized model. The matrix $\boldsymbol{B}(k) \in \mathbb{R}^{37\times 37}$ is called noise input matrix and $\boldsymbol{\Psi}(k) \in \mathbb{R}^{37\times 37}$ is integral of the state transition matrix. MATLAB's c2d function is utilized to compute $\boldsymbol{\Psi}(k)$ and $\boldsymbol{\Psi}(k)$ from $\boldsymbol{A}(k)$ and $\boldsymbol{B}(k)$ with respect to the sample time $\Delta t$. The matrix $\boldsymbol{c}(k) \in \mathbb{R}^{16\times 37}$ is the Jacobian matrix of the measurement model and is used to compute estimated state and covariance at *a posteriori*.

### A Posteriori

The measurements are updated at *posteriori* and the equation 2.15 can be used to compute the EKF estimate and covariance. Kalman filter outputs the unbiased estimates with minimum mean squared error. Intuitively Kalman Filter determines the weight between its measurements and process model by solving an optimization problem or Algebraic Riccati Equation where such weight is embedded in gain matrix $\boldsymbol{K}(k)$ in equation 2.15. Since the process model assumes no process noise for aircraft equation of motion and bias dynamics, the resulting EKF estimate $\hat{x}(k)$ for k from 0 to N corrects for sensor biases. Lastly the optimal properties of the Kalman Filter are lost in EKF. The linearization of the nonlinear system must approximate the nonlinear system for EKF to resemble the optimal properties of the Kalman Filter.

$$
\begin{aligned}
\boldsymbol{K}(k) =&\bar{\boldsymbol{P}}(k)\boldsymbol{C}^T(k)(\boldsymbol{C}(k)\bar{\boldsymbol{P}}(k)\boldsymbol{C}^T(k)+\boldsymbol{R}(k))^{-1}\\
\hat{x}(k) =&\bar{x}(k)+\boldsymbol{K}(k)(z(k)-g(\bar{x}(k)))\\
\hat{\boldsymbol{P}}(k) =&(\boldsymbol{I}-\boldsymbol{K}(k)\boldsymbol{C}(k))\bar{\boldsymbol{P}}(k)(\boldsymbol{I}-\boldsymbol{K}(k)\boldsymbol{C}(k))^T+\boldsymbol{K}(k)\boldsymbol{R}(k)\boldsymbol{K}^T(k)
\end{aligned}
\tag{2.15}
$$

The process and measurement covariance matrices $\boldsymbol{Q}(k) \in \mathbb{R}^{37\times 37}$ and $\boldsymbol{R}(k) \in \mathbb{R}^{16\times 16}$ in equations 2.13 and 2.15 are the parameters of EKF where higher values of $\boldsymbol{Q}(k)$ and $\boldsymbol{R}(k)$ damps the weight of the process and measurement models respectively. The matrix $\boldsymbol{Q}(k)$ is defined positive semi-definite whereas the matrix $\boldsymbol{R}(k)$ must be positive definite. In practice the noises are assumed decoupled and diagonal matrices are used for $\boldsymbol{Q}(k)$ and $\boldsymbol{R}(k)$. See equations 2.16 and 2.17.

$$
\boldsymbol{Q}(k) = \operatorname{diag}\left(\mathbf{0}_{10}, 100\boldsymbol{I}_3, \mathbf{0}_3, 100\boldsymbol{I}_3, \mathbf{0}_3, 1000\boldsymbol{I}_3, 1000\boldsymbol{I}_3, 1000\boldsymbol{I}_3, \mathbf{0}_6\right)^2 \tag{2.16}
$$

$$
\boldsymbol{R}(k) = \operatorname{diag}\left(0.05\boldsymbol{I}_3, 0.2\frac{\pi}{180}\boldsymbol{I}_3, 0.3\frac{\pi}{180}\boldsymbol{I}_3, 2, 0.05, 5\frac{\pi}{180}\boldsymbol{I}_2, 0.03\boldsymbol{I}_3\right)^2 \tag{2.17}
$$

As rule of thumb, the matrix $\boldsymbol{R}(k)$ is set to the variances of the measurements using the standard deviations of the on-board sensors provided by the manufacturer. Innovation and the sequence of normalized innovations squared metrics were used to assist the tuning of the matrix $\boldsymbol{Q}(k)$ to avoid incorrect application of the process and measurement noise co-variance that results in either underestimation or overestimation. Such metrics are used to check the consistency of the Kalman filter by ensuring unbiasedness and correct error variation of the estimates. Read [26, 27] for more details on normalized innovations squared testing.

#### Kalman smoothing

The smoothed state estimates and the error covariance matrix propagation can be computed using the equation 2.18 which runs backward for k from N to 0. See [10] and references therein for more information about the algorithm and their derivation.

$$
\begin{aligned}
\boldsymbol{K}_S(k) =&\hat{\boldsymbol{P}}(k)\boldsymbol{\Phi}^T(k+1)\bar{\boldsymbol{P}}^{-1}(k+1)\\
x^S(k) =&\hat{x}(k)+\boldsymbol{K}_S(k)(x^S(k+1)-\bar{x}(k+1))\\
\boldsymbol{P}^S(k) =&\hat{\boldsymbol{P}}(k)+\boldsymbol{K}_S(k)(\boldsymbol{P}^S(k+1)-\bar{\boldsymbol{P}}(k+1))\boldsymbol{K}_S^T(k)
\end{aligned}
\tag{2.18}
$$

Similar to the optimal filtering which typically gives an estimate that maximizes its conditional probability given the measurements up-to time step k, the optimal smoothing results in estimates that maximizes its conditional probability given all the measurements. Note that path reconstruction with EKF filtering and smoothing is done offline in batch (the sequence of log data at different times stitched together). Applying path reconstruction simultaneously for all the collected manoeuvres in batch mode provides decoupled estimates of the scale factors and biases by avoiding the correlations between these parameters [10].

### 2.2.3 Iterative extended Kalman smoothing - offline

One of the drawbacks of EKF is linearzation where significant nonlinearities can affect the accuracy of the estimation. [22] and references therein presents an Iterative Extended Kalman Filter (IEKF) which is based on local iterations of linearization in each sample interval. These local iterations improves the reference trajectories for linearization in the presence of nonlinearity. The iterator algorithm is presented in equation 2.19. Note that parenthesis for the time step k has been moved the subscript ($\boldsymbol{K}(k) = \boldsymbol{K}_k$ as an example) for the definitions provided in section 2.2.2.

$$\begin{aligned} \xi_{i+1} =& \bar{x}_k + \boldsymbol{K}_k(\xi_i)[z_m - g_k(\xi_i) - \boldsymbol{C}_k(\xi_i)(\bar{x}_k - \xi_i)] \\ \hat{\boldsymbol{P}}_k =& [I - \boldsymbol{K}_k(\xi_l)\boldsymbol{C}_k(\xi_l)]\bar{\boldsymbol{P}}_k[I - \boldsymbol{K}_k(\xi_l)\boldsymbol{C}_k(\xi_l)]^T + \boldsymbol{K}_k(\xi_l)\boldsymbol{Q}\boldsymbol{K}_k^T(\xi_l) \end{aligned} \tag{2.19}$$

Note the notations $i = 1, 2, ..., l$, $\xi_1 = \bar{x}_k$ and $\hat{x}_k = \xi_l$. In IEKF the iterator algorithm presented above is repeated at each sample interval. The gain matrix $K_k$, the measurement equation $g_k$ and its linearization matrix $\boldsymbol{C}$ are computed during these iterations. The iterations are terminated when $\|\xi_{i+1} - \xi_i\|_2 < \varepsilon$. In this way the reference trajectory where the measurement equations are linearized are updated in each iterations within the same sample interval. This improves the estimation error resulting from linearization errors. The process covariance $\boldsymbol{Q}$ is given in equation 2.20 whereas the measurement covariance $\boldsymbol{R}$ is given in equation 2.17.

$$\boldsymbol{Q}(k) = \operatorname{diag}(\boldsymbol{0}_{10}, 100\boldsymbol{I}_3, \boldsymbol{0}_3, 100\boldsymbol{I}_3, \boldsymbol{0}_3, 1000\boldsymbol{I}_3, 1000\boldsymbol{I}_3, 1000\boldsymbol{I}_3, \boldsymbol{0}_6) \tag{2.20}$$

Furthermore IEKF is combined with backward Kalman smoothing presented in the equation 2.18. Since the backward Kalman smoothing is an offline procedure this algorithm is called offline iterative extended Kalman smoothing (offline IEKS).

### 2.2.4 Iterative extended Kalman smoothing - online

The offline IEKS algorithm reduces the effects of non-linearity present in the measurement equations. In the online IEKS algorithm effects of non-linearity in the process equations are also reduced by updating the reference trajectory for the linearization of process equations. The online IEKS algorithm is presented in the equation 2.21. [22] and references therein presents the online IEKS algorithm.

$$\begin{aligned} \xi_{i+1} =& \bar{x}_k + \boldsymbol{K}_k(\xi_i)[z_m - g_k(\xi_i) - \boldsymbol{C}_k(\xi_i)(\bar{x}_k - \xi_i)] \\ \zeta_{i+1} =& \hat{x}_{k-1} + \boldsymbol{W}_k(\zeta_i)[\xi_{i+1} - \bar{x}_k] \end{aligned} \tag{2.21}$$

Note the notations $i = 1, 2, ..., l$, $\xi_1 = \bar{x}_k$ and $\zeta_1 = \hat{x}_{k-1}$. Please refer to equation 2.22 for the definitions used in the equation 2.21.

$$\begin{aligned} \widetilde{x}_k(\zeta_i) =& \zeta_i + \int_{t_{k-1}}^{t_k} f(\widetilde{x}(\tau), u_m(\tau), \tau)\mathrm{d}\tau \\ \bar{x}_k =& \widetilde{x}_k(\zeta_i) + \boldsymbol{\Phi}_k(\zeta_i)(\hat{x}_{k-1} - \zeta_i) \\ \bar{\boldsymbol{P}}_k =& \boldsymbol{\Phi}_k(\zeta_i)\hat{\boldsymbol{P}}_{k-1}\boldsymbol{\Phi}_k^T(\zeta_i) + \boldsymbol{\Psi}(\zeta_i)\boldsymbol{Q}\boldsymbol{\Psi}^T(\zeta_i) \\ \boldsymbol{K}_k(\zeta_i, (\xi_i)) =& \bar{\boldsymbol{P}}_k\boldsymbol{C}_k^T(\xi_i)[\boldsymbol{C}_k(\xi_i)\bar{\boldsymbol{P}}_k\boldsymbol{C}_k(\xi_i)^T + \boldsymbol{R}]^{-1} \\ \boldsymbol{W}_k =& \hat{\boldsymbol{P}}_k\boldsymbol{\Phi}_k^T\hat{\boldsymbol{P}}_k^T \end{aligned} \tag{2.22}$$

Within each time step k the equation 2.21 is iterated until $\|\xi_{i+1} - \xi_i\|_2 < \varepsilon$ and $\|\zeta_{i+1} - \zeta_i\|_2 < \varepsilon$. Then the estimate and the covariance matrix are updated using equation 2.23.

$$\begin{aligned} \hat{x}_k =& \xi_l \\ \hat{\boldsymbol{P}}_k =& [I - \boldsymbol{K}_k(\xi_l, \zeta_l)\boldsymbol{C}_k(\xi_l, \zeta_l)]\bar{\boldsymbol{P}}_k[I - \boldsymbol{K}_k(\xi_l, \zeta_l)\boldsymbol{C}_k(\xi_l, \zeta_l)]^T \\ &+ \boldsymbol{K}_k(\xi_l, \zeta_l)\boldsymbol{Q}\boldsymbol{K}_k^T(\xi_l, \zeta_l) \end{aligned} \tag{2.23}$$

Note that the process covariance $\boldsymbol{Q}$ is given in equation 2.24 whereas the measurement covariance $\boldsymbol{R}$ is given in equation 2.17.

$$\boldsymbol{Q}(k) = \operatorname{diag}(\boldsymbol{0}_{10}, \boldsymbol{0}_3, \boldsymbol{0}_3, \boldsymbol{0}_3, \boldsymbol{0}_3, 10\boldsymbol{I}_3, 10\boldsymbol{I}_3, 1000\boldsymbol{I}_3, \boldsymbol{0}_6) \tag{2.24}$$

Three different nonlinear path reconstruction methods have been discussed and implemented as part of the local system identification tool chain. An advantage of the online IEKS is its online capabilities. For example the online IEKS can be used for online system identification. Yet it takes about 15 iterations to converge which is computationally expensive. For the following sections offline IEKS will be used as it only requires about 4 iterations in each time step while providing better performance than EKS algorithm.

### 2.2.5 Results of flight path reconstruction

The results of flight path reconstruction are shown in figures 2.7, 2.8, A.1 and 2.9 where two phugoid manoeuvres are shown in batch. The vertical line separates them. In figure 2.7 the measured longitudinal states of the aircraft are compared to the IEKS estimates. The estimates of offline IEKS do not deviate from the measured flight test data. Furthermore the x-axis and z-axis accelerations are smoothed. The mean innovation for p,q,r are $4.8{\cdot}10^{-6}$, $2.1{\cdot}10^{-5}$ and $6.9{\cdot}10^{-6}$ respectively while the mean innovation for $a_x$,$a_y$,$a_z$ show -0.022, 0.005 and -0.009 respectively. These values indicates that the estimation is unbiased with given initialization and the choice of process and measurement covariance matrices.

Figure 2.8 compares the IEKS estimate of longitudinal forces and moments to the longitudinal force and moment constructed using the direct substitution of raw measurements into the aircraft dynamics in equation 2.2. From visual inspection the smoothed estimate of force and moment smooth the noise in measurements.

In figure A.1 the estimation of bias and scaling factors is shown. The bias from inertial measurements are $\Delta a_x = 0.012$ m/$s^2$, $\Delta a_y = 9.72 \cdot 10^{-5}$ m/$s^2$, $\Delta a_z = -0.0082$ m/$s^2$ for linear accelerations and $\Delta p = -1.21 \cdot 10^{-4}$ rad/$s$, $\Delta q = -4.971 \cdot 10^{-4}$ rad/$s$, $\Delta r = -6.428 \cdot 10^{-4}$ rad/$s$ for angular velocities. The scaling factor for true airspeed is estimated as $K_{va} = 1.5$ whereas the bias for angle of attack and angle of side-slip are estimated as zero. In fact the difference between the magnitude of ground speed from GPS and true airspeed from airdata probe in this experiment is found to be the same as estimated scaling factor $K_{va} = 1.5$. Furthermore Elektra 1 is not equipped with wind sensors to measure the angle of attack and side-slip and consequently no bias is found as their estimated values were derived under the assumption of no wind and constructed from ground speed. Note that the angle of attack and angle of side-slip could be removed from EKF. Their inclusion was to make the tool chain universal.

To prove the validity of the aerodynamic force and moment estimation from EKF longitudinal states of the aircraft namely $u$, $w$, $q$ and $\theta$ are reconstructed using the aircraft equations of motion. The input to the numerical integration is the time history of longitudinal force and moment. Initial conditions are chosen as the trim states.

The result is shown in figure 2.9 where the sensor measurements of the longitudinal states are compared to the trajectories obtained from solving the aircraft equations of motion using the IEKS estimate of the aerodynamic force and moment. In parallel the longitudinal states were also reconstructed from the raw inertial measurements and plotted. It can be seen that the direct substitution of the raw inertial measurements into the aircraft equation of motion results in considerable drift whereas reconstructed states using the IEKS estimates of force and moment show correction for the drift. Such large drift can result from noise and biases present in the inertial measurements. Note that the small drift in the dotted black line can be attributed to a small mismatch in the initial values which were only roughly specified and held fixed. Furthermore estimating a single set of biases for the two flight maneuvers can also cause this drift.

Overall the objectives of data compatibility check have been met. The estimated

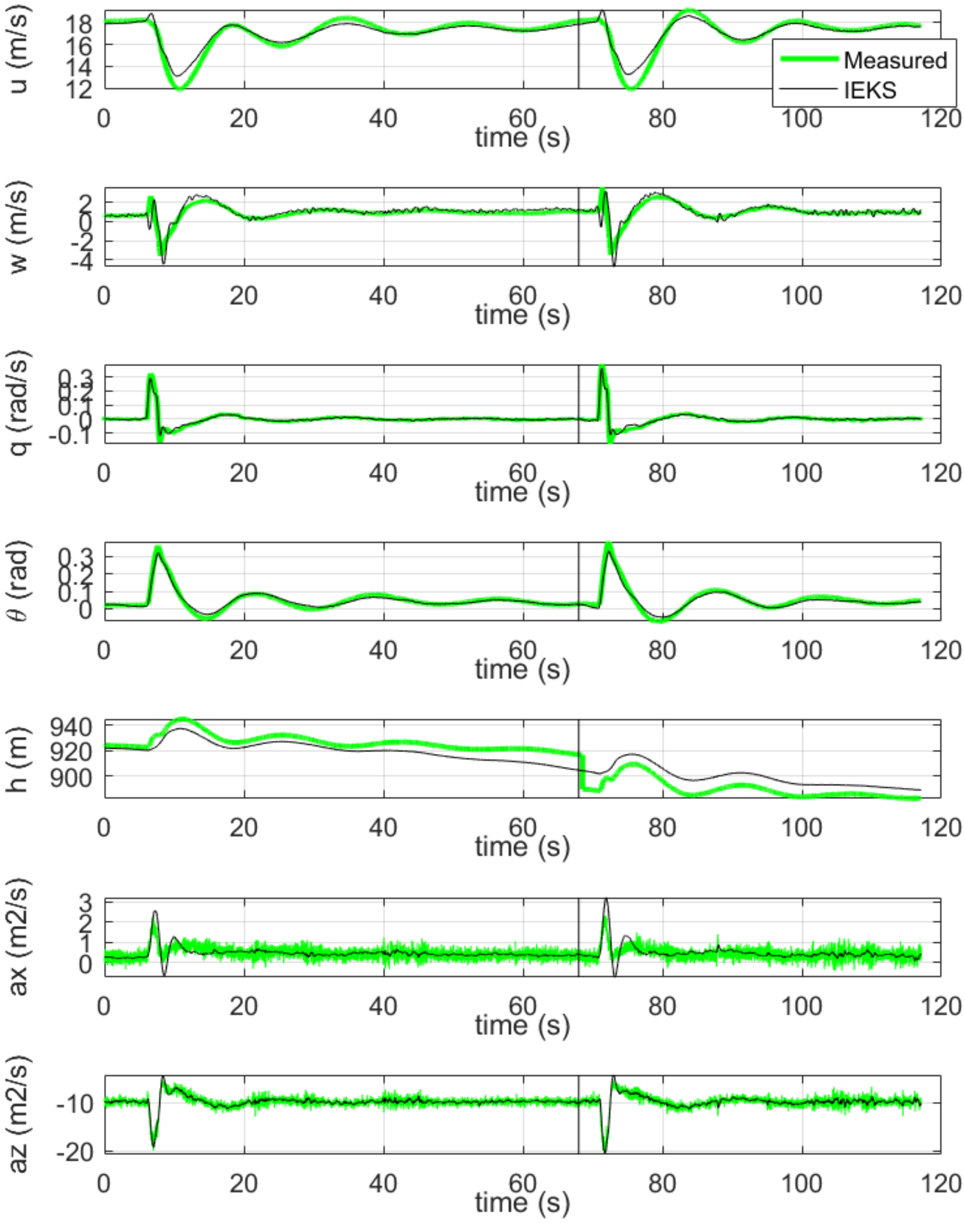

Figure 2.7: A comparison between the measured and the IEKS estimated aircraft responses.

states show good alignment with the ground truth. Measurement biases and scaling factors for IMU and air data probe are determined. Finally, the smoothed estimation of force and moment are computed. The validity of estimated biases, and the smoothed estimation of force and moment have been checked through their substitution into the numerical integration of the aircraft equations of motion. The main differences to other applications of the two step method (e.g [9]) is the smoothing of IEKF estimates in estimation-before-modelling approach with Kalman smoothing. Its advantage becomes evident in applying the method of least squares which is prone to noises [10].

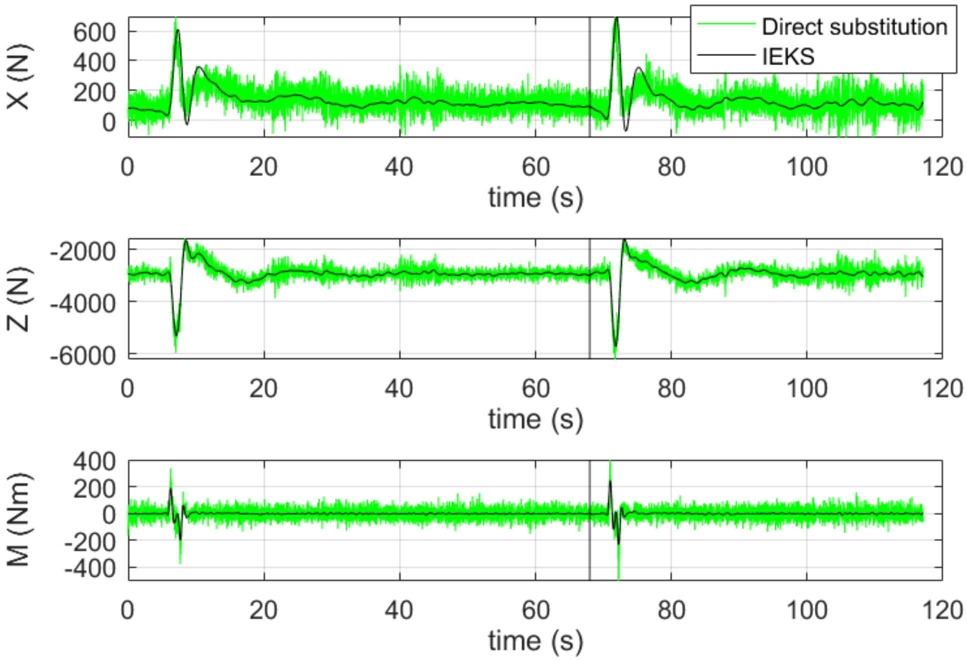

Figure 2.8: A comparison of the forces & moments reconstructed from inertial measurements and forces & moments estimation from the offline IEKS.

## 2.3 Aerodynamic model identification

The second step of the two step method is identification of parameters. The aerodynamic model identification involves (1) determination of aerodynamic model structure or parameters to be identified, and (2) identification of parameters through an optimization.

### 2.3.1 Linear aerodynamic model identification

The identification of the linear aerodynamic model represents a grey box approach. Linearizing the nonlinear equations of motion around a trim point (called also an equilibrium) and assuming that the longitudinal states have a negligible influence on the lateral force and moment, and vice versa, the state space representation for the longitudinal states of an aircraft is shown in equation 2.25. The derivations of the state space representation can be found in literature such as [10, 14, 19]

$$\begin{aligned} \boldsymbol{M}\dot{x} &= \boldsymbol{A}x + \boldsymbol{B}u \\ x &= \begin{bmatrix} u & w & q & \theta \end{bmatrix}^T \\ u &= \begin{bmatrix} de & dt \end{bmatrix}^T \end{aligned} \tag{2.25}$$

The matrices $\boldsymbol{M}$, $\boldsymbol{A}$ and $\boldsymbol{B}$ are shown in equations 2.26, 2.27 and 2.28 respectively. Note that $u_0$, $w_0$ and $\theta_0$ correspond to equilibrium points.

$$\boldsymbol{M} = \begin{bmatrix} m & 0 & 0 & 0 \\ 0 & m & 0 & 0 \\ 0 & 0 & I_{yy} & 0 \\ 0 & 0 & 0 & 1 \end{bmatrix} \tag{2.26}$$

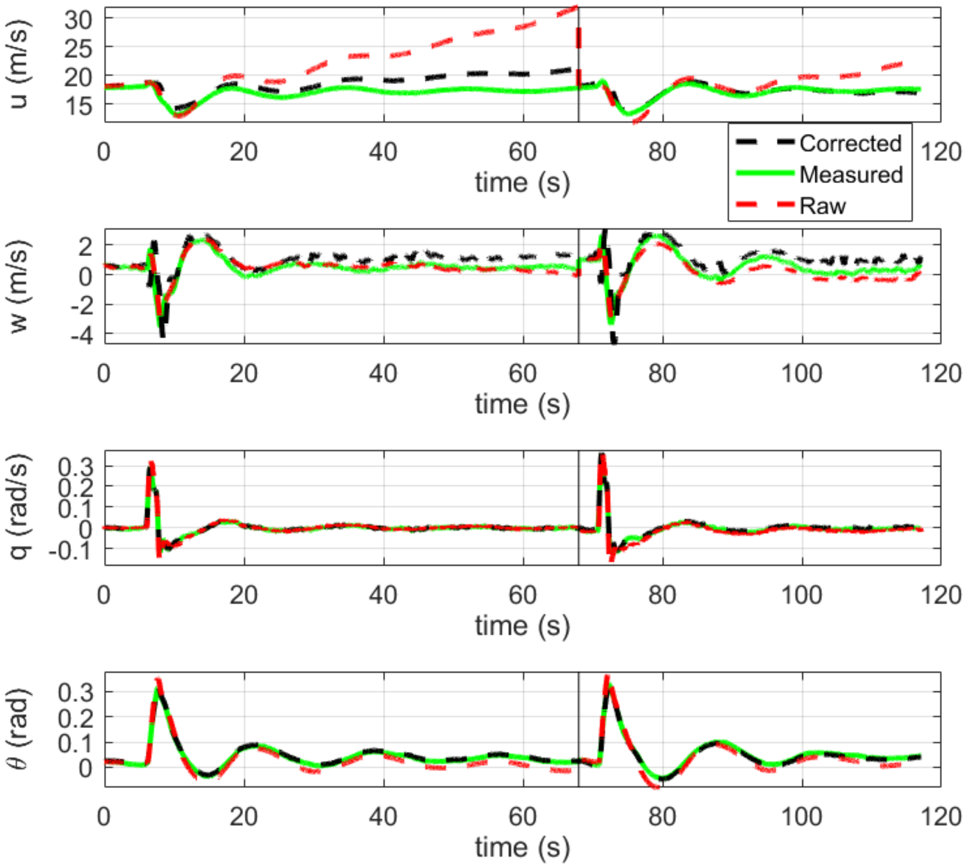

Figure 2.9: Validation of offline IEKS estimation using aircraft equations of motion.

$$\boldsymbol{A} = \begin{bmatrix} X_u & X_w & X_q - mw_0 & -mgcos\theta_0 \\ Z_u & Z_w & Z_q + mu_0 & -mgsin\theta_0 \\ M_u & M_w & M_q & 0 \\ 0 & 0 & 1 & 0 \end{bmatrix} \tag{2.27}$$

$$\boldsymbol{B} = \begin{bmatrix} X_{de} & X_{dt} \\ Z_{de} & 0 \\ M_{de} & 0 \\ 0 & 0 \end{bmatrix} \tag{2.28}$$

The elements of $\boldsymbol{A}$ and $\boldsymbol{B}$ are called stability and control derivatives and they are derived by applying first order multivariate Taylor series approximation to the aerodynamic force and moment around an equilibrium. The linear model structure is shown in equation 2.29. The parameters $X_0$, $Z_0$ and $M_0$ are biases and typically cancelled out when deriving the state space representation shown in equation 2.25.

$$\begin{aligned} X &= X_0 + X_u u + X_w w + X_q q + X_{de} de + X_{dt} dt \\ Z &= Z_0 + Z_u u + Z_w w + Z_q q + Z_{de} de \\ M &= M_0 + M_u u + M_w w + M_q q + M_{de} de \end{aligned} \tag{2.29}$$

Using equation 2.29 the optimization problem can be formulated as a least squares problem which is equivalent to a maximum likelihood estimate of the parameters. Analytical solutions exist for least squares and convergence to global minimum is guaranteed. The MATLAB function mldivide can be used for the ordinary least squares method. See [13] for details on the least squares method for system identification. One of the challenges in system identification is finding the set of parameters that can represent the physical phenomena in aircraft. Depending on the data set the optimal solution that gives optimal value may not represent the physical phenomena. To check the robustness of the data set, codes for the weighted least squares, nonlinear least squares and constrained least squares have been implemented. Here, the constrained least squares is applied using the priori knowledge of the aerodynamic parameters (the sign and approximate magnitude). These methods must provide similar parameters and otherwise, the possible cause had to be found. One can imagine a data set where the damped oscillations in phugoid is perturbed by the wind. The parameters that result in a global minimum would be incorrect as it would give positive signs for the stability parameters related to the damping. In this case, the parameters obtained from the ordinary least squares method would deviate from the parameters obtained from the constrained least squares method.

Table 2.1: Aerodynamic parameters for the linear model

| **Term** | **Value** | **Term** | **Value** | **Term** | **Value** |
|---|---|---|---|---|---|
| $X_0$ | 848.6782 | $Z_0$ | -3.4686E3 | $M_0$ | -335.9959 |
| $X_u$ | -82.5606 | $Z_u$ | 12.6203 | $M_u$ | 13.2402 |
| $X_w$ | 8.3085 | $Z_w$ | -91.5232 | $M_w$ | -1.5825 |
| $X_q$ | 2.8088E3 | $Z_q$ | -1.0522E4 | $M_q$ | -1.0818E3 |
| $X_{de}$ | 4.8189E3 | $Z_{de}$ | -1.4559E4 | $M_{de}$ | -4.0732E3 |
| $X_{dt}$ | 1.2004E3 | | | | |

See table 2.1 for the identified parameters.

### 2.3.2 Nonlinear aerodynamic model identification

The identification of nonlinear aerodynamic models requires a selection of model structure as the parameters of nonlinear aerodynamic model can vary depending on the aircraft and data gathered. Essentially tools from linear regression can be used to select the nonlinear aerodynamic model structure. The feature or regressor selection was based on (1) correlation analysis and (2) significance testing. General explanation about linear regression can be found in [28] whereas [9, 10, 8] explain their extension to the aircraft system identification.

Correlation analysis is performed to quantify the association between two continuous variables. Since significant dependencies between the features can perturb the identification result to be non-meaningful (identified parameters to deviate from actual stability and control derivatives although the identified parameters fit the data optimally with respect to certain cost function) correlation analysis is a crucial step in linear regression. The correlation levels can be calculated using equation 2.30 with the equation 2.31 representing covariance between two random variables.

$$R(x_i, x_j) = \frac{C(x_i, x_j))}{\sqrt{C(x_i, x_i), C(x_j, x_j)}} \tag{2.30}$$

$$C(x_i, x_j) = \mathrm{E}[(x_i - \mathrm{E}(x_i))(x_j - \mathrm{E}(x_j))] \tag{2.31}$$

Generally the value of $R = 0.9$ serves as a threshold. R values higher than 0.9 indicate significant correlation between two features and must be avoided.

The t-statistic is a form of significance testing for each features. This is used to eliminate insignificant features in order to avoid over-fitting of the data. See equation 2.32 where $\hat{\theta}_i$ indicates a single model term and $s(\hat{\theta}_i)$ denote its standard deviation which can be computed using the error residual and diagonal elements of co-variance matrix.

$$t_0 = \frac{\hat{\theta}_i}{s(\hat{\theta}_i)} \tag{2.32}$$

Large values of t-statistics indicate high significance of the feature whereas low values of t-statistics indicate low significance of the feature [9].

$$\begin{aligned} X &= X_0 + X_u u + X_w w + X_q q + X_{de} de + X_{dt} dt \\ &+ X_{wq} wq + X_{wde} wde + X_{w^2} w^2 \\ Z &= Z_0 + Z_u u + Z_w w + Z_q q + Z_{de} de \\ &+ Z_{wq} wq + Z_{wde} wde + Z_{w^2} w^2 \\ M &= M_0 + M_u u + M_w w + M_q q + M_{de} de \\ &+ M_{wq} wq + M_{wde} wde + M_{w^2} w^2 \end{aligned} \tag{2.33}$$

Following an extensive analysis and evaluations with various combination of features the model structure shown in equation 2.33 has been selected as the nonlinear aerodynamic model.

Table 2.2: Aerodynamic parameters for the nonlinear model

| **Term** | **Value** | **Term** | **Value** | **Term** | **Value** |
|---|---|---|---|---|---|
| $X_0$ | 909.5517 | $Z_0$ | -3.8864E3 | $M_0$ | -338.7066 |
| $X_u$ | -85.4185 | $Z_u$ | 22.9396 | $M_u$ | 12.5911 |
| $X_w$ | -121.5265 | $Z_w$ | 279.3562 | $M_w$ | 28.2114 |
| $X_q$ | 3.0593E3 | $Z_q$ | -1.1500E4 | $M_q$ | -1.1159E3 |
| $X_{de}$ | 7.151E3 | $Z_{de}$ | -2.3309E4 | $M_{de}$ | -4.5261E3 |
| $X_{dt}$ | 1.2982E3 | | | | |
| $X_{wq}$ | -443.7352 | $Z_{wq}$ | 583.6403 | $M_{wq}$ | 133.1528 |
| $X_{wde}$ | -5.1432E3 | $Z_{wde}$ | 1.5717E4 | $M_{wde}$ | 1.1687E3 |
| $X_{w^2}$ | -18.9805 | $Z_{w^2}$ | 52.707 | $M_{w^2}$ | 3.069 |

Using the method of least squares the parameters of the nonlinear aerodynamic model parameters presented in table 2.2 have been found.

## 2.4 Aerodynamic model validation

The identified parameters must be validated. Note that the data set used for identification of parameters have been strictly separated from the data set used for validation.

Figure 2.10 shows the time history of control inputs for the phugoid manoeuvre (a pulse in elevator). In all the figures hereafter in this section the training data set is plotted from 0s to 65s while the range from 65s to 110s depicts the validation data set. In figure 2.10 rudder signal dr show a constant zero over time as there was no encoder to measure rudder deflections and is also not used during the flight test.

### 2.4.1 Linear model validation

In figure 2.11 the offline IEKS estimate of the longitudinal force and moment (dependent variable) is compared to the model prediction of the longitudinal force and moment. The vertical black line at approximately 65 separates training set (left) and validation set (right).

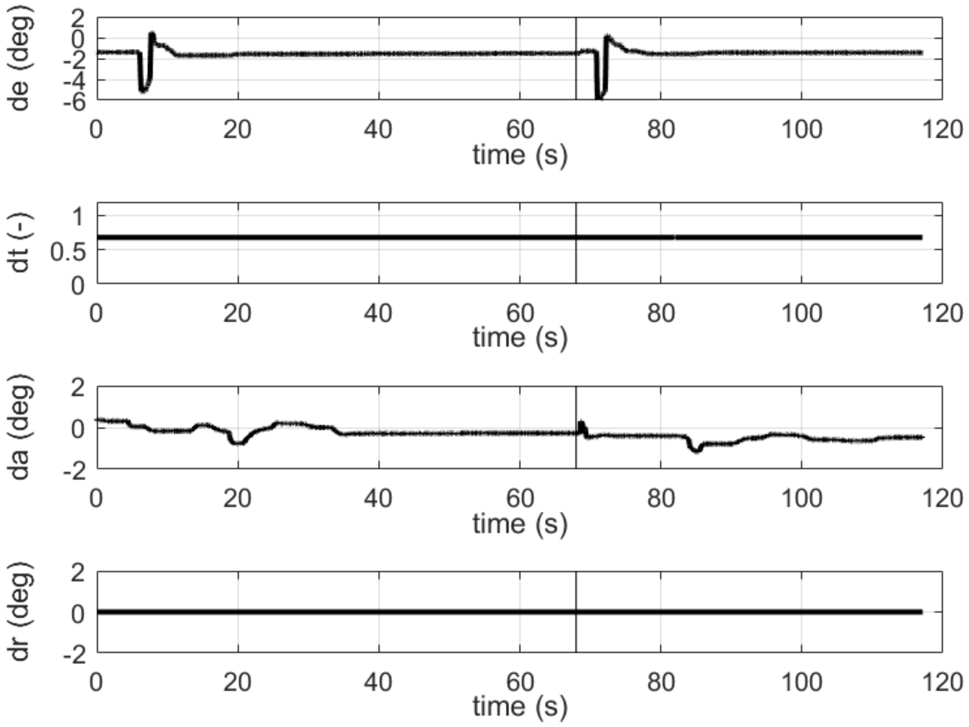

Figure 2.10: Control inputs during an exemplary system identification manoeuvre

See table 2.3 for the quantitative assessment of the identified linear model. The coefficient of determination ($R^2$ value), the root mean square error (RMSE) and the normalized root mean squared error (NRMSE) are presented for each longitudinal aerodynamic force and moment. NRMSE is chosen as the ratio between RMSE and range of the dependent variable. The coefficient of determination is defined in equation 2.34 where $y_i$ is the dependent variable at the step i, $f_i$ is the prediction of the dependent variable at the step i, and $\overline{y}$ is the mean of the dependent variable. $R^2$ is related to the fraction of unexplained variance or a ratio between unexplained variance over the total variance of the data.

$$R^2 = 1 - \frac{\sum_i (y_i - f_i)^2}{\sum_i (y_i - \overline{y})^2} \tag{2.34}$$

The RMSE is defined using equation 2.35 whereas the NRMSE is defined as shown in equation 2.36. $y_{max}$ and $y_{min}$ are the maximum and minimum values of the dependent variable y. The RMSE is a measure of accuracy while the NRMSE is an indicative measure of prediction error with respect to the total range of the data in percentage.

$$\text{RMSE} = \sqrt{\frac{\sum_i^n (y_i - f_i)^2}{n}} \tag{2.35}$$

$$\text{NRMSE} = \frac{\text{RMSE}}{y_{max} - y_{min}} \tag{2.36}$$

All the statistical values presented in table 2.3 do not vary significantly between the identification set and the validation set. As a significant increase in RMSE between the two sets, for example, can infer over-fitting of the data it can be concluded that identified model show no sign of over-fitting.

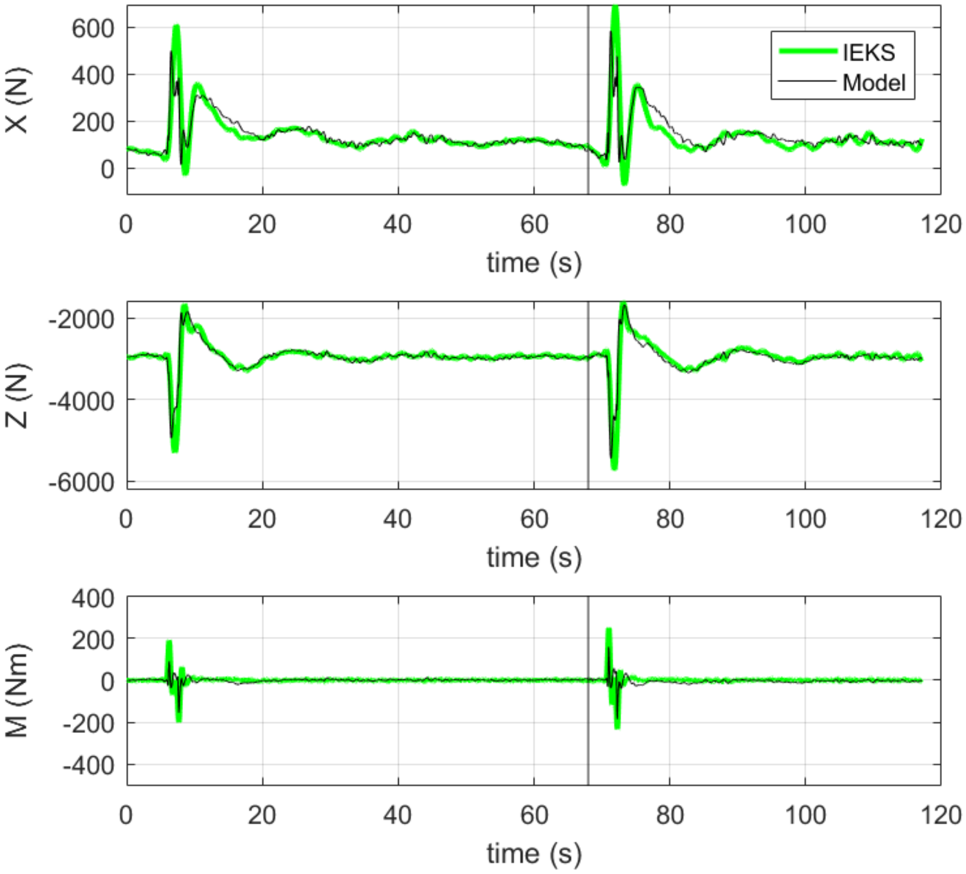

Figure 2.11: Estimated and model predicted force and moment comparison for the linear model.

Table 2.3: R-squared, RMSE and NRMSE for force and moment prediction of linear model.

| Identification | | | | Validation | | | |
|---|---|---|---|---|---|---|---|
| Coef | $X$ | $Z$ | $M$ | Coef | $X$ | $Z$ | $M$ |
| $R^2$ | 0.69 | 0.79 | 0.30 | $R^2$ | 0.65 | 0.77 | 0.29 |
| RMSE | 41.89 | 153.7 | 15.89 | RMSE | 49.15 | 178.5 | 19.29 |
| NRMSE | 0.065 | 0.042 | 0.041 | NRMSE | 0.063 | 0.043 | 0.039 |

The identified parameters are further validated using forward simulation based on the aircraft equations of motion. Initial conditions and time histories of the control inputs from the measurements were used to simulate the longitudinal states where the force and moment acting on the aircraft are computed at each time step using the model parameters. Runge-Kutta of 4th order was the numerical integration method found to be adequate and initial conditions here refer to the trim states. Figure 2.12 show the results of the forward simulation. From visual inspection the obtained model parameters show good alignment with the measurements.

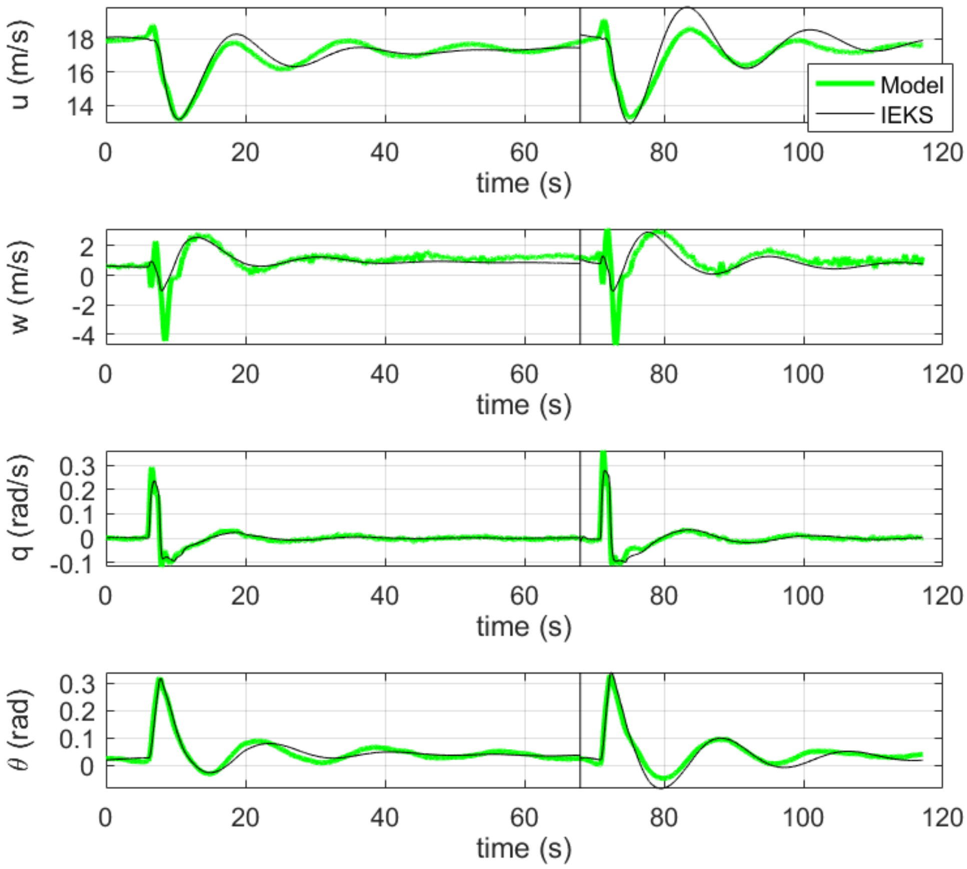

Figure 2.12: A comparison between estimated and simulated responses of aircraft using the linear model.

The performance of the forward simulation is quantified using the goodness-of-fit (GOF) as well as Theil's inequality coefficient (TIC). These metrics have been proposed in [10] to analyze the discrepancy between measurements and simulation. The GOF is defined in equation 2.37. Note that the cost function is selected as normalized mean square error and thus, is equivalent to $R^2$ in equation 2.34. The GOF value of 1 indicates a perfect match between the measurement and prediction of the model whereas -Inf is an indication of bad fit. If the GOF is equal to 0, then the prediction is no better than a straight line at matching the dependent variable. Higher its value, better the performance of the model.

$$\text{GOF} = \sqrt{\frac{\sum_i^n (y_i - f_i)^2}{n}} \tag{2.37}$$

On the other hand, TIC ranges from 0 to 1 where the value of 0 indicate a perfect match between the measurement and prediction. The TIC is defined in equation 2.38 where $y_m \in \mathbb{R}^n$ is the measurements (dependent variable) and $y_p \in \mathbb{R}^n$ is its prediction. According to [10] TIC values between 0.25-0.3 is an indication of a satisfactory model match in aircraft system identification. The computed GOF and TIC values are reported in table 2.4.

$$\text{TIC} = \frac{\sqrt{\frac{1}{n}(y_m - y_p)^T(y_m - y_p)}}{\sqrt{\frac{1}{n}y_m^T y_m} + \sqrt{\frac{1}{n}y_p^T y_p}} \tag{2.38}$$

Table 2.4: TIC and GOF values for forward simulation using identified linear model.

| **Nonlinear**: | | | | | | | | | |
|---|---|---|---|---|---|---|---|---|---|
| Identification | | | | | Validation | | | | |
| State | u | w | q | $\theta$ | State | u | w | q | $\theta$ |
| GOF | 0.9037 | 0.5856 | 0.8959 | 0.9323 | GOF | 0.7156 | 0.5119 | 0.8765 | 0.8981 |
| TIC | 0.0094 | 0.2154 | 0.1660 | 0.0971 | TIC | 0.1872 | 0.2626 | 0.1753 | 0.1239 |

Based on the values reported in table 2.4, u, q and $\theta$ are represented well by the identified model with GOF values between 0.7 and 0.94, and TIC values all below 0.2 which is a clear indication that the dynamic behaviors of the aircraft for both training and validation set are reproducible by the model. Yet, w is the only longitudinal state with relatively poor values of GOF and TIC. This might be attributed to the discrepancies of the model during the initial phase of the excitation where the error up-to 4m/s is found in figure 2.12. The cause for such discrepancies must be thoroughly analyzed in future works.

Federal Aviation Administration (FAA) is an organization that regulate all aspects of aviation [29]. FAA also defines the certification regulations for the flight simulators which can be found in [30]. According to [30] a flight simulation is a high fidelity if the tolerances for the pitch angle $\theta$ and the pitch rate $q$ lies with the tolerances of ±1.5 degrees and ±2 degree/s respectively.

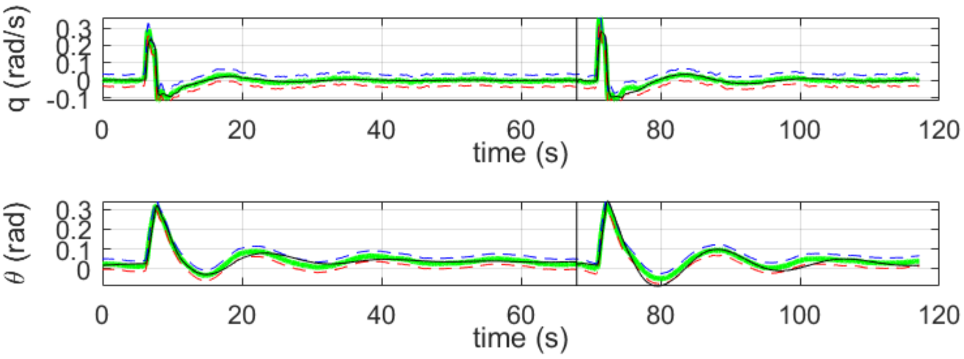

Figure 2.13: FAA standards on high fidelity model.

Figure 2.13 is shown to check whether the obtained linear model satisfies the standards of high fidelity model set by FAA. The IEKS estimates (the green line) of $\theta$ and $q$ are compared against the model predictions (the black line) of $\theta$ and $q$. The dotted blue and dotted red line indicate the upper bound and the lower bound to satisfy the FAA standards of the high fidelity model. The bounds are computed using the tolerances defined by [30]. From figure 2.13 the model predictions of $\theta$ and $q$ fall inside these tolerances and therefore, the model is of high fidelity.

### 2.4.2 Nonlinear model validation

The nonlinear model can be validated using the same approach where force and moment between IEKS estimation and model prediction can be compared and quantitatively analyzed for both the training and the validation sets. See figure 2.14.

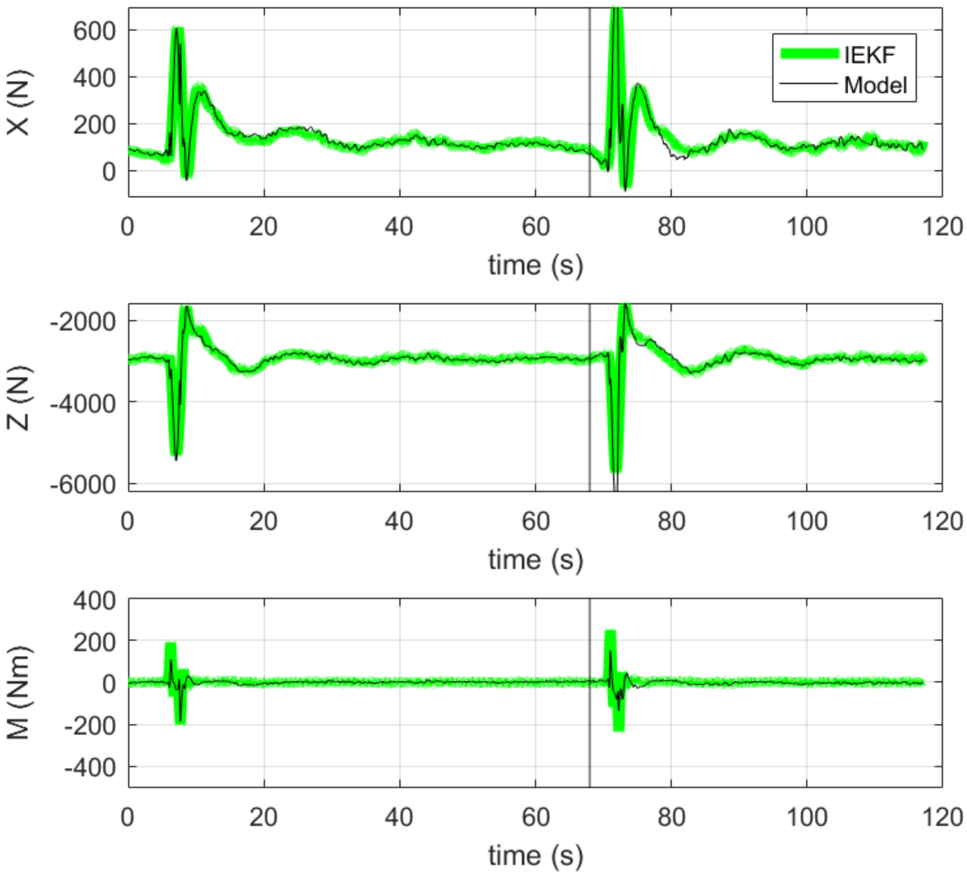

Figure 2.14: Estimated and model predicted force and moment comparison.

The nonlinear aerodynamic model is able to accurately predict the initial phases of the system identification manoeuvre for the force X and Z. The initial phases correspond to the time histories between 0s and 20s, and 65s and 80s approximately. Please compare figures 2.11 and 2.14. Yet, no such improvements were found in predicting the pitching moment M.

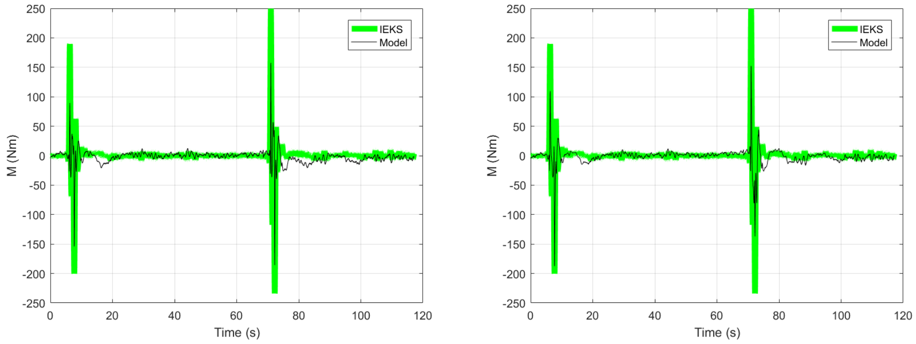

Figure 2.15: Linear model (left) and Nonlinear model (right).

For better visibility the pitching moment predictions with both linear and nonlinear model are shown in separate figures (see figure 2.15). Perhaps the nonlinearities in pitching moment derivatives were absent. It is recommended to thoroughly study the aerodynamics of Elektra 1 in order to quantify the regions or sets of states were the linear approximation of stability and control derivatives would be valid.

Table 2.5: Statistical metrics on force and moment prediction of nonlinear model.

| Identification | | | | Validation | | | |
|---|---|---|---|---|---|---|---|
| Coef | $X$ | $Z$ | $M$ | Coef | $X$ | $Z$ | $M$ |
| $R^2$ | 0.921 | 0.937 | 0.443 | $R^2$ | 0.847 | 0.883 | 0.418 |
| RMSE | 21.01 | 82.56 | 14.11 | RMSE | 32.44 | 127.1 | 17.32 |
| NRMSE | 0.027 | 0.020 | 0.0292 | NRMSE | 0.042 | 0.031 | 0.036 |

The table 2.5 quantifies the statistical metrics on forces and model prediction using nonlinear aerodynamic model. For the training data set the nonlinear model shows high fidelity prediction capabilities with significant improvement with respect to the linear model. The RMSE typically found to be twice as small while the $R^2$ for forces are above 0.9 which is an indication of high fidelity. Yet, the accuracy decrease in the validation set. This is an indication of over-fitting although significant improvement comparing to the linear model is still found.

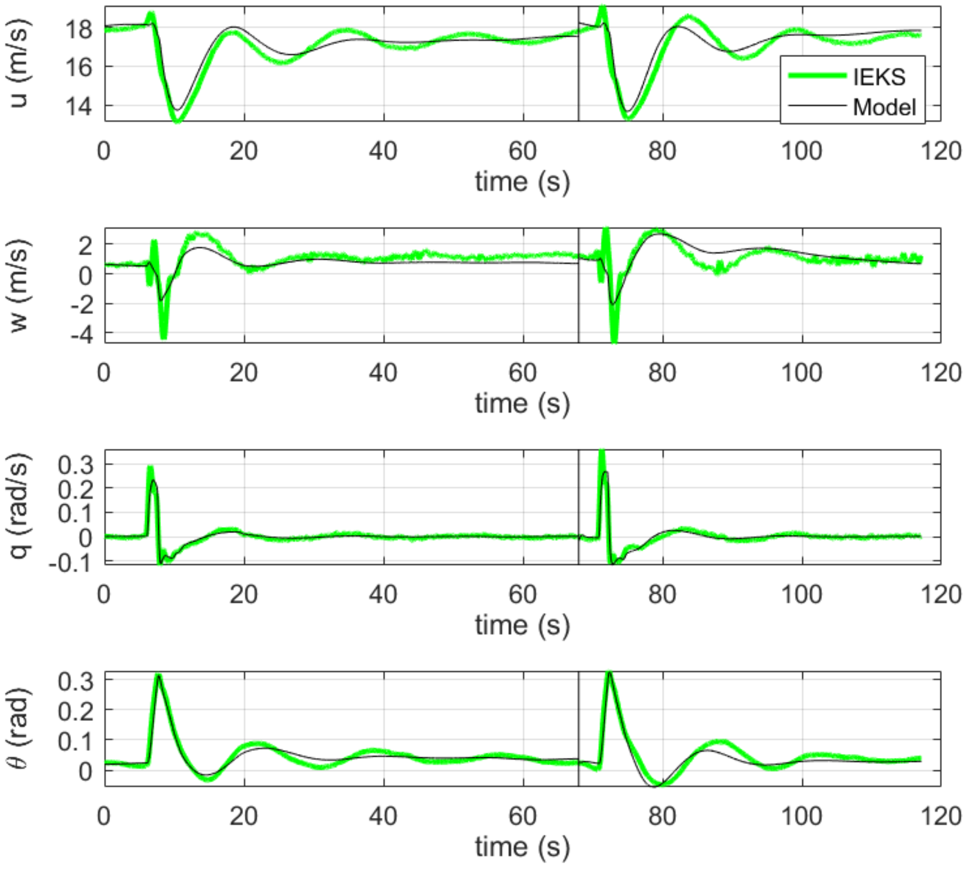

Figure 2.16: A comparison between measured and simulated responses of aircraft using nonlinear model.

Table 2.6: TIC and GOF values for forward simulation using identified nonlinear model.

| | | | | | | | | | |
|---|---|---|---|---|---|---|---|---|---|
| **Linear**: | | | | | | | | | |
| Identification | | | | | Validation | | | | |
| State | u | w | q | $\theta$ | State | u | w | q | $\theta$ |
| GOF | 0.8821 | 0.5789 | 0.8834 | 0.9279 | GOF | 0.8569 | 0.5576 | 0.8507 | 0.9061 |
| TIC | 0.0104 | 0.2390 | 0.1764 | 0.1023 | TIC | 0.0133 | 0.2201 | 0.1985 | 0.1289 |

The results of the forward simulation for the nonlinear aerodynamic model is shown in figure 2.16 whereas the statistical metrics are presented in table 2.6. In forward simulations no significant differences are found between the linear and nonlinear model. Improvements with respect to linear model has been found in fitting of forces and moments for both training and validation set. The NRMSE has decreased from 0.063 to 0.042, 0.043 to 0.031, and 0.039 to 0.036 for X, Z and M respectively.
Figure 2.17 has been plotted to evaluate the model according to the FAA standards of high fidelity. Again the nonlinear model satisfies the FAA standards of high fidelity.

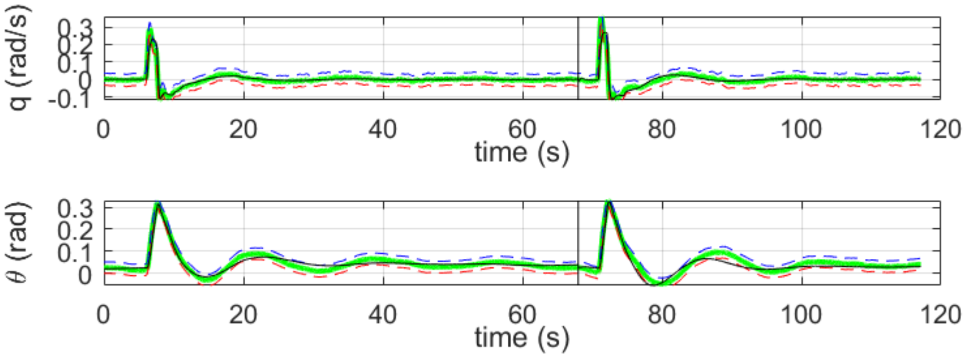

Figure 2.17: FAA standards on high fidelity model.

## 2.5 Limitations and future works

The two step method has been applied to obtain both linear and nonlinear aerodynamic model for the longitudinal dynamics of Elektra 1 aircraft. In summary control inputs that excites the modes of aircraft has been designed and applied in flight test. The criteria of parameter identifiability were applied to ensure that data contains sufficient information about the stability and control derivatives. Techniques from nonlinear reconstruction of path have been applied to process the data for the parameter search based on the least squares method. With linear regression the parameters of both linear and nonlinear aerodynamic model were found. Statistical metrics on validation set has shown that identified parameters represent the aircraft dynamics in high accuracy. Furthermore the standards of FAA for certifying flight simulators were compared and it is concluded that the model meets the criteria of high fidelity.
One of the limitations of the current work is the data set limited to only phugoid data. Currently two elevator pulse manoeuvre (phugoid) are used for identification and validation. The data set with other control inputs such as DLR3211 elevator and doublet with throttle have been collected. However, these data set have been discarded after the quality check. Since the aircraft system identification and model validation with various types of aircraft manoeuvres can add more reliability to the

results, it is recommended to collect data set for not only DLR3211 elevator and throttle doublet, but also chirp and PRBS elevator and throttle signals.

The local system identification presented in this chapter has been limited to longitudinal dynamics. Since the same methods can be applied to model the lateral dynamics it can be one of the future works to perform system identification experiments for lateral dynamics.

Further investigation is required for the overall identification procedures. The offsets in magnitude and phase of the model prediction of longitudinal states, and the discrepancies found in the simulation of z-axis velocity $w$ must be mitigated. It would require rigorous analysis to identify the causes and several iterations.

# Chapter 3

# System identification tool box and its application to Penguin BE

In this chapter system identification tool box based on two step method is presented and its exemplary application to Penguin BE UAV is demonstrated.

## 3.1 Overview of two step method

The figure 3.1 shows an overview of the system identification procedure using the two step method. As shown in figure 3.1 the aircraft system identification overall involves data gathering, parameter identification and model validation. For data gathering, a priori model is used for the input design to guarantee the identifiability of the parameters. In other words the multi-step input signals are designed with a specific time step such that the contribution of all aerodynamic derivatives on force and moment is maximized in the dynamic manoeuvre. The designed multi-step input signals are used in flight test to collect the data.

An important first step in parameter identification is the flight path reconstruction where the compatibility of the collected data is checked with the aircraft equations of motion. The outputs of the first step are the reconstructed and smoothed forces, moments and states of the aircraft where the biases and the scaling factors of the sensors are removed from the measurements. The second step involves multi-variable regression where the aerodynamic model structure can be selected based on physical and statistical analysis and the method of least squares is applied to obtain the values of aerodynamic parameters. In parallel to standard model validation methods such as proof of match (including FAA standards of fidelity [29, 30]) and residual analysis, the identified aerodynamic model can be validated through off-line control synthesis (e.g. loop gain shaping) and testing the controller in real flight.

In this chapter detailed explanation about the methods are omitted and interested readers can read chapter 2 for more information on the methods.

Overall explanation about the system identification tool box using the two step method is presented in this chapter. Furthermore, its application to the Penguin BE UAV for the system identification of the longitudinal model is addressed. The differences in applying the two step method for identification of aerodynamic parameters between Elektra 1 and Penguin BE UAV are highlighted.

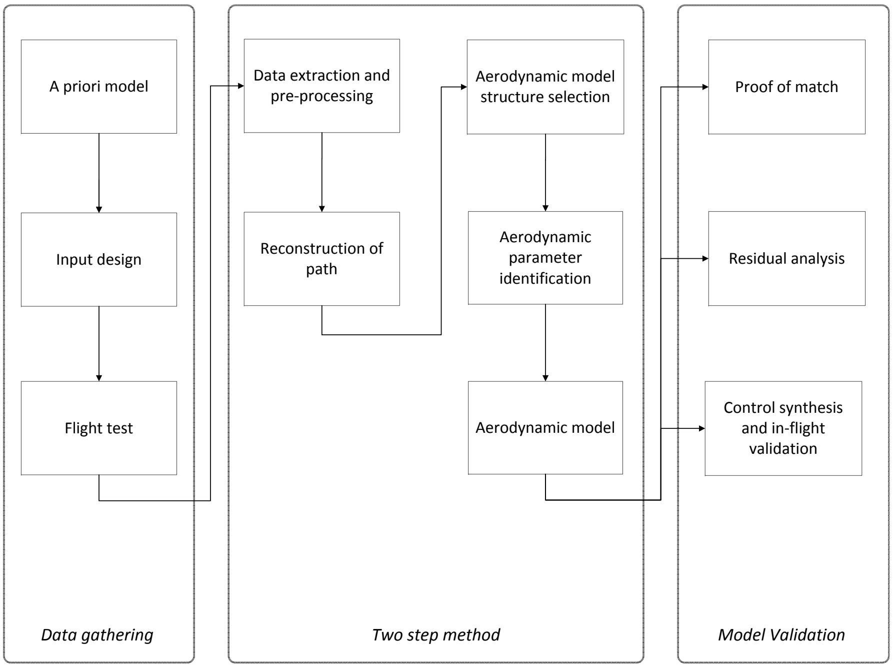
A priori model
Input design
Flight test
Data gathering
Data extraction and pre-processing
Reconstruction of path
Aerodynamic model structure selection
Aerodynamic parameter identification
Aerodynamic model
Two step method
Proof of match
Residual analysis
Control synthesis and in-flight validation
Model Validation

Figure 3.1: Overview of two step method.

## 3.2 System Identification tool box

The system identification tool chain contains following folders where all the blocks in the figure 3.1 are executed.

1. A priori model computation.
2. Input design (see table 3.1).
3. Flight test simulation.
4. Data extraction (see table 3.2).
5. Data consistency check or reconstruction of path (see table 3.3).
6. Parameter identification (see table 3.2).
7. Model validation (see table 3.5).

A priori model computation is based on the work presented in [3]. A linear state space representation which contains aerodynamic derivatives is obtained using the MATLAB's linmod function. The flight test simulation software within flying robots group is explained in [31, 32] and the step three (3. simulation of flight test) is to check whether the designed input signals result in expected manoeuvre of the aircraft (e.g maximum attitude and velocity range) which must result in safe flight conditions.

Table 3.1: Input design

| **m-file** | **Remarks** |
|---|---|
| Parameters.m | Input to the code is linearized equation of motion from AVL based simulation. |
| Identifiability.m | Outputs the bode diagrams such as figure 2.3. |
| InputGeneration.m | Outputs the input signals and their energy spectrum (see figure 2.4). The time step and magnitude of the input signals must be selected to maximize the information on specific parameters as discussed in chapter 2. |

Table 3.2: Data extraction and pre-processing

| **m-file** | **Remarks** |
|---|---|
| vis_log.m | Load the recorded data from flight test. The output is data stored in workspace variable and .mat file which is named as an example, E1_SYSID_FE1.mat for the first system identification data set of elektra 1. Such data is used as an input in DataExtraction.m. |
| DataExtraction.m | Extraction of specific manoeuvres where index of each manoeuvres must be found looking into the control inputs. Required variables including the states of the aircraft are selected and assigned. Necessary transformations are also made.. The output is DATA_ALL.mat file which is used as an input data to data compatibility check or path reconstruction. |

Table 3.3: Data compatibility check

| **m-file** | **Remarks** |
|---|---|
| ekf_calc_f.m | A function for the process model. |
| ekf_calc_h.m | A function for the measurement model. |
| ekf_calc_Fx.m | A function for the linearization process model. |
| ekf_calc_Hx.m | A function for the linearization measurement model. |
| main.m | EKF implementation with forward filtering and backward smoothing. Input to the file is DATA_ALL.mat and the output of the file is EKF_DATA_ALL.mat. Figures are generated. |
| PlotThesis.m | (a) Plots the comparison between measured and simulated responses with bias corrections for the longitudinal states. (b) Plots the comparison between force and moment computed from direction substitution in the equation of motion and EKFS implementation. (c) Plots the biases and scale factors in the sensors. |
| PlotInnovation.m | Plots the innovation for correct tuning of the EKFS. |
| PlotNIS.m | Plots the normalized innovation squared for correct tuning of the EKFS. |

Table 3.4: Parameter identification

| m-file | Remarks |
|---|---|
| ParaID.m | The main script that computes the identified parameters. The input is EKF_DATA_ALL.mat and the output is identified model parameters both stability and control derivatives. Inside the script all the data are divided into identification and validation set. Least squares algorithm is executed with sets of independent variables which represent the aerodynamics model. Then, both identification and validation plots are given which compares the force and moment from the model to the ones constructed from measurements. |
| ID_VAL_SET.m | Division of all the data into identification and validation set. |
| ID_VAL_SET_S.m | Division of all the data into identification and validation set with multivariate smoothing. |
| MDL_L1.m | Linear aerodynamic model in body frame. The script outputs A and b matrix ($Ax = b$) for least squares method. |
| MDL_NL1.m | Nonlinear aerodynamic model in body frame. The script outputs A and b matrix ($Ax = b$) for least squares method. Using the analysis of independent variables using correlation and t-statistics, the selection of the model in body frame can be performed. |
| LS_TU.m | Ordinary least squares algorithm. |
| LS_mldivide.m | MATLAB's ordinary least squares algorithm. |
| WLS_TU.m | Weighted least squares algorithm. |
| NLS_matlab.m | MATLAB's nonlinear least squares algorithm. |

Table 3.5: Model validation

| m-file | Remarks |
|---|---|
| EOM_Integrate.m | A main script for a forward simulation of rigid body equations of motion. With initial states from the measurements as its initial conditions and time histories of measured control inputs, the script computes the time histories of aircraft states which is being compared to measured time histories of aircraft states for validation. |
| MDL_L1.m | A function that contains the linear aerodynamic model in body frame. |
| MDL_NL1.m | A function that contains the nonlinear aerodynamic model in body frame. |
| Plot_VAL.m | Plots for comparison of measured aircraft states to estimated aircraft states from the identified model. The data set concerned is the validation set. |

## 3.3 Penguin BE local system identification

This section describes the local system identification procedure for Penguin BE UAV with the system identification tool chain described above. The differences found with respect to the Elektra 1 system identification procedures are highlighted.

### 3.3.1 Data gathering

Please find the general introduction and methodology on data gathering in chapter 2. The designed control inputs are presented in figures below together with their energy spectrum. The bode plots based on a priori model that were used to design these control inputs can be found in the section A.2, Appendix A.

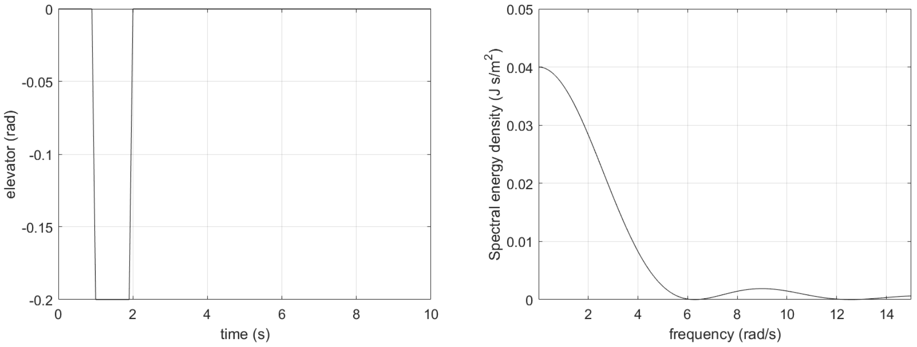

Figure 3.2: Phugoid manoeuvre - elevator (left) and energy spectrum (right)

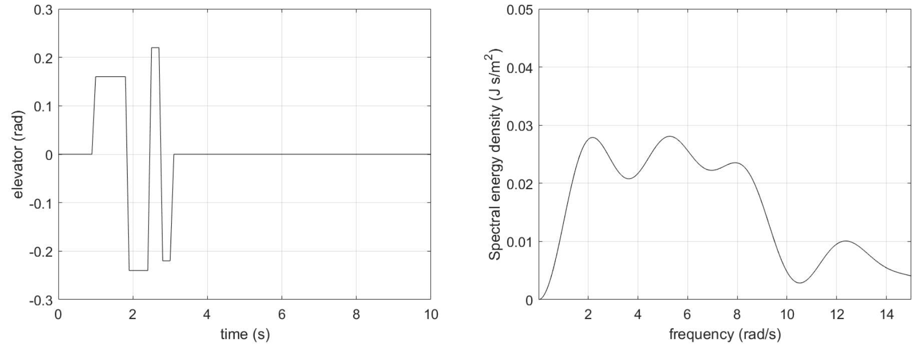

Figure 3.3: Short period manoeuvre - elevator (left) and energy spectrum (right)

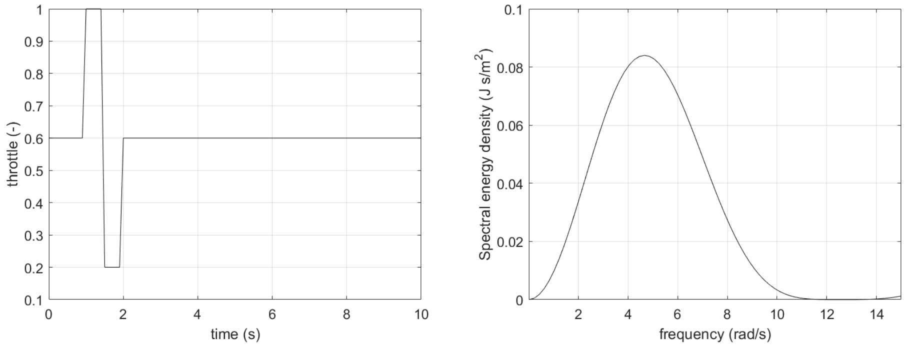

Figure 3.4: Thrust variation manoeuvre - throttle (left) and energy spectrum (right)

One of the key difference are the use of an autopilot. The experiment was performed by the manual pilot for Elektra 1 whereas the manoeuvres are activated by the operator on the ground for Penguin BE. The autopilot for Penguin BE was ready and could be used for the system identification experiments. In case the autopilot (flight control system) is not available one can first reach the trim condition via manual pilot, and then execute the system identification manoeuvres using a simple code.

One of the key advantages in using the autopilot for the data gathering can be found in a better trim condition and consistency in the applied control inputs. A key disadvantage with Penguin BE was the lack of measurements for the control surfaces. Since there existed no measurements on control signals, a low pass filter was used on commanded control signals during the system identification manoeuvres so that no rate limit saturation and delay would be visible between commanded and executed control signals. According to [12], the human pilot acts as a low pass filter with the cut off frequency of 10 rad/s. Therefore, the cut off frequency for the design of the low pass filter was also selected as 10 rad/s. In this way, possible deficiency of the data due to the lack of faster dynamics in the coefficients were avoided.

One of the other possible approach could have been manual calibration in the laboratory and also including the actuator delays in the parameters to be identified. Additionally, the actuators can be modelled as 2nd order systems. Of course, the installation of encoders would have been the best option. It is recommended to investigate further on solving the issues related to the lack of measurements for the control surfaces.

Overall three system identification test campaigns have been performed where each campaign had improvements in data gathering procedures. During the final flight test 15 manoeuvres were performed with 5 elevator pulses, 5 elevator DLR-3211 manoeuvres and 5 throttle doublets. After the analysis of the data, 9 manoeuvres were selected. Among them 3 manoeuvres were selected as the validation set (one each for different input signals: pulse, DLR3211 and doublet) and the rest of the manoeuvres were used for training or identification.

### 3.3.2 Reconstruction of path

The results of nonlinear reconstruction of path for Penguin BE UAV is included in this section. Offline IEKS which combines a forward iterative extended Kalman filter with backward Kalman smoothing have been used to (1) estimate instrumentation errors, (2) obtain the smoothed estimates of aerodynamic force and moment from noisy inertial measurements, and (3) check the consistency of the sensor measurements using the 6DOF rigid body equations of motion for an aircraft. The method for nonlinear reconstruction of path can be found in chapter 2 while results of bias estimation and its validation can be found in appendix A.

The main difference to Elektra 1 flight path reconstruction lies in the choice of the process and measurement covaraince matrices for the offline IEKS. The measurement covariance matrix $\boldsymbol{R}$ and the process covariance matrix $\boldsymbol{Q}$ can be found below. Following the rules of thumb, sensor specifications were used to select the values for $\boldsymbol{R}$. The initial states have been chosen as average of 50 measurements points that correspond to the trim condition. The initial co-variance matrix $\boldsymbol{P}_0$ can be found in the equation 2.11.

$$\boldsymbol{Q}(k) = \operatorname{diag}\left(\mathbf{0}_{10}, 0\boldsymbol{I}_3, \mathbf{0}_3, 0\boldsymbol{I}_3, \mathbf{0}_3, 100\boldsymbol{I}_3, 1000\boldsymbol{I}_3, 0.1\boldsymbol{I}_3, \mathbf{0}_6\right)^2 \tag{3.1}$$

$$\boldsymbol{R}(k) = \operatorname{diag}\left(0.05\boldsymbol{I}_3, 0.25\frac{\pi}{180}\boldsymbol{I}_3, 0.3\frac{\pi}{180}\boldsymbol{I}_3, 2, 10, 10\frac{\pi}{180}\boldsymbol{I}_2, 0.02\boldsymbol{I}_3\right)^2 \tag{3.2}$$

Furthermore a wind vane (WV) has been attached to the airdata probe for the last two system identification flights of Penguin BE. Therefore measurements on angle of attack and angle of side-slip have been obtained. The measurement equations were changed as shown in the equation below.

$$
\begin{aligned}
V_{a_m}(t) &= K_{v_a}\sqrt{u(t)^2+v(t)^2+w(t)^2} \\
V_{a_{\mathrm{AP}}}(t_k) &= V_{a_m}(t_k) + \mathfrak{v}_{v_a}(t_k) \\
\\
\alpha_m(t) &= \arctan\frac{w(t)}{u(t)} + \mathit{\Delta}\alpha \\
\alpha_{\mathrm{WV}}(t_k) &= \alpha_m(t_k) + \mathfrak{v}_{\alpha}(t_k) \\
\\
\beta_m(t) &= \arctan\frac{v_a(t)}{\sqrt{u(t)^2+v(t)^2+w(t)^2}} + \mathit{\Delta}\beta \\
\beta_{\mathrm{WV}}(t_k) &= \beta_m(t_k) + \mathfrak{v}_{\beta}(t_k)
\end{aligned}
\tag{3.3}
$$

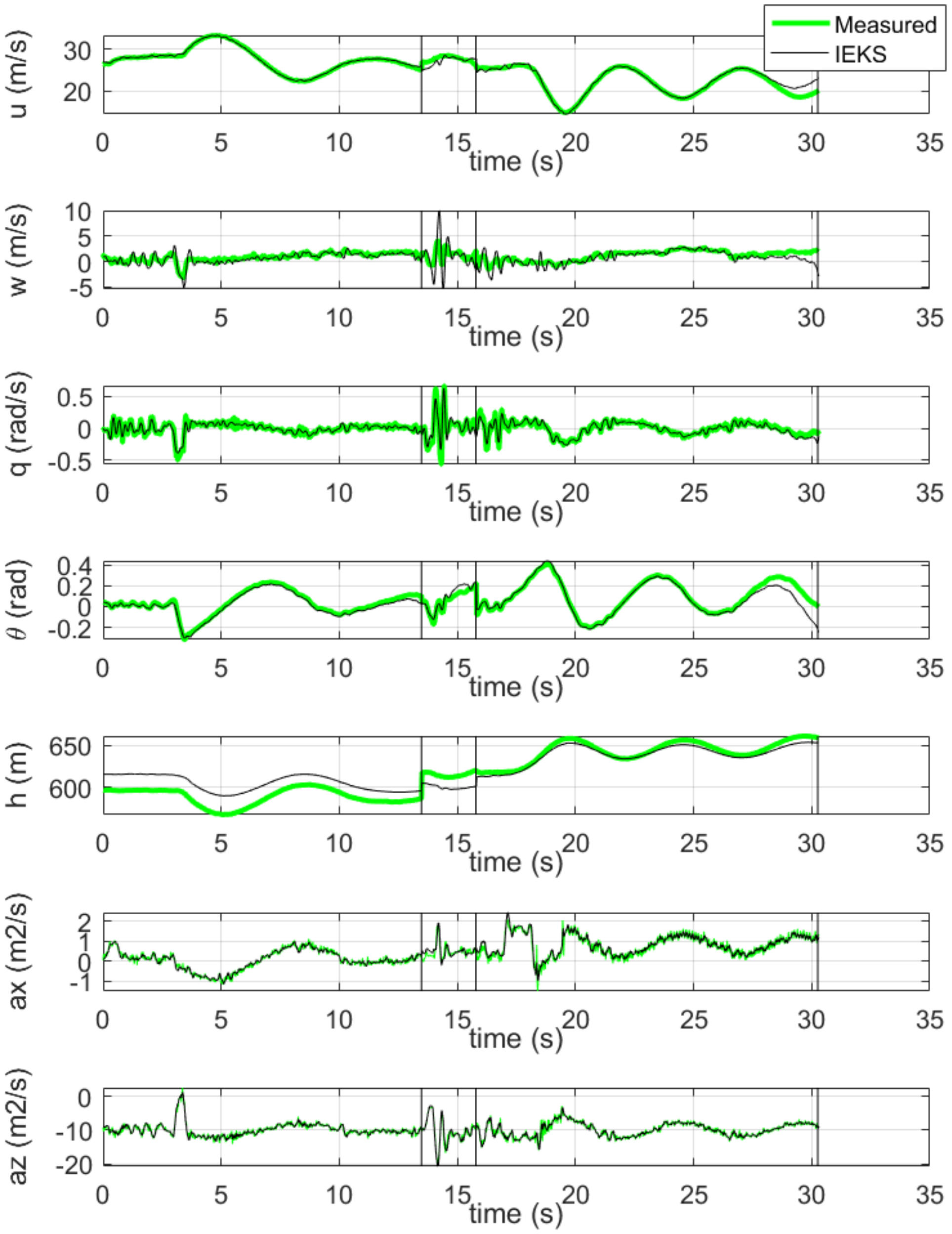

Figure 3.5: Measured vs estimated aircraft responses.

Figure 3.5 compares the IEKS estimation of aircraft responses with the measurements. From visual inspection, the IEKS estimates of aircraft responses are in good alignment with the measurements. Figure 3.6 depicts IEKS estimation of aerodynamic force and moment in solid black line. The force and moment reconstructed from direct substitution of inertial measurements are shown in green line. Clearly they are in good alignment and the IEKS estimation smoothed the noisy measurements. In figure 3.5 the discontinuity of the signals can be found after the black vertical line. This is because the flight path reconstruction is performed on the data set which is comprised of different system identification manoeuvres from different times combined together.

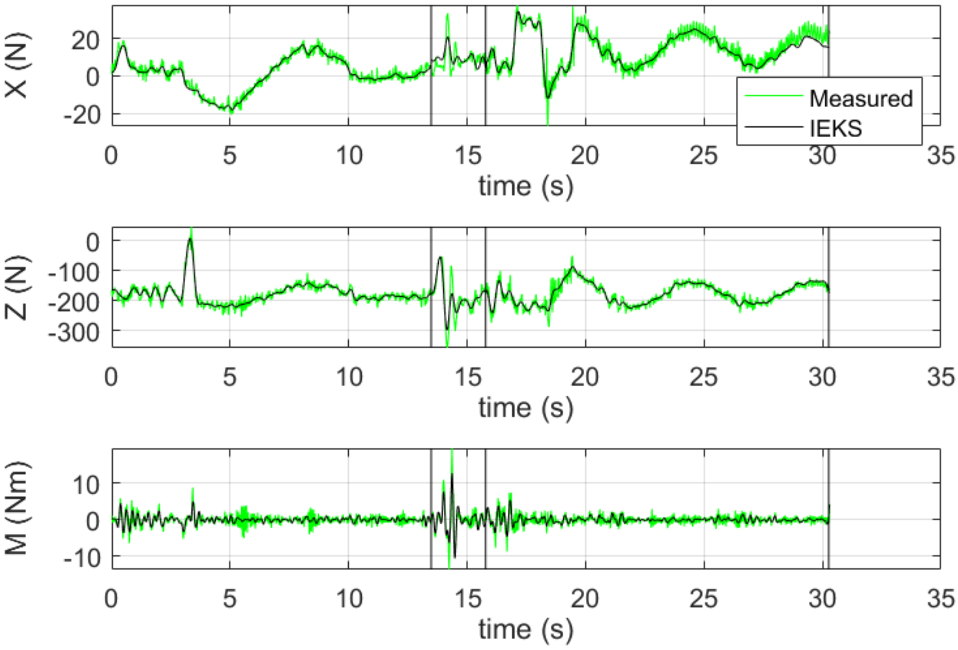

Figure 3.6: Force and moment reconstructed from inertial measurements vs force and moment from offline IEKS estimation.

In figure 3.6 the IEKS estimate of force and moment is plotted with force and moment reconstructed from the inertial measurements and their direct substitution into the equations of motion. It can be observed that the IEKS estimate smoothed the force and moment reconstructed from the inertial measurements. In comparison to Elektra 1 the IMU seemed to give less noisy measurements. This might be attributed to smaller engine which causes comparably less vibrations.

Overall the objectives of the data compatibility check have been met. Inclusion of the wind vane is advantageous as both ground speed and true airspeed can be known in 3 dimensions.

### 3.3.3 Parameter identification and validation

The second part of the two step method is the parameter identification step where the least squares method is applied to the chosen aerodynamic structure. While the linear aerodynamic model can be used for all conventional aircraft the non-linear aerodynamic model structure must be selected using techniques from linear regression such as correlation analysis and t-test for features [9, 8]. See chapter 2 for more detailed explanation. Note that the maximum values for $\alpha_m$ and $\beta_m$ during the flight test did not exceed $\pm 10^\circ$ and also, the designed input signals for

the elevator did not exceed ±7°. This indicates the aerodynamic phenomena could have been restricted to the linear region and therefore, identification and validation of a nonlinear aerodynamic model has not been necessary.
The validation and analysis of the identified aerodynamic model has been approached with (1) strict separation between training and validation data sets, and (2) applying statistical metrics for evaluation. The determinant coefficient $R^2$, root mean squared error (RMSE) and normalized root mean squared error (NRMSE) with the range (max - min) have been utilized to evaluate the prediction capabilities of the aerodynamic model. The forward simulation with the linear model was evaluated using Goodness-of-fit (GOF) and Theil's inequality coefficient (TIC).
The key differences to the Elektra 1 local system identification are found to be in the selected data-sets where several iterations of flight tests with improvements resulted in (1) correction execution of DLR 3211 manoeuvres and (2) achievement of similar trim conditions for all manoeuvres. In this section all the included plots show works related to the validation set. As an example figure 3.7 shows the control inputs used to obtain the validation data set where Pulse-elevator ($t = 0$s to $t = 10$s), DLR3211-elevator ($t = 10$s to $t = 18$s) and doublet-throttle ($t = 18$s to $t = 30$s) are combined in batch. For further plotting of results these different manoeuvres are separated by a vertical black line.

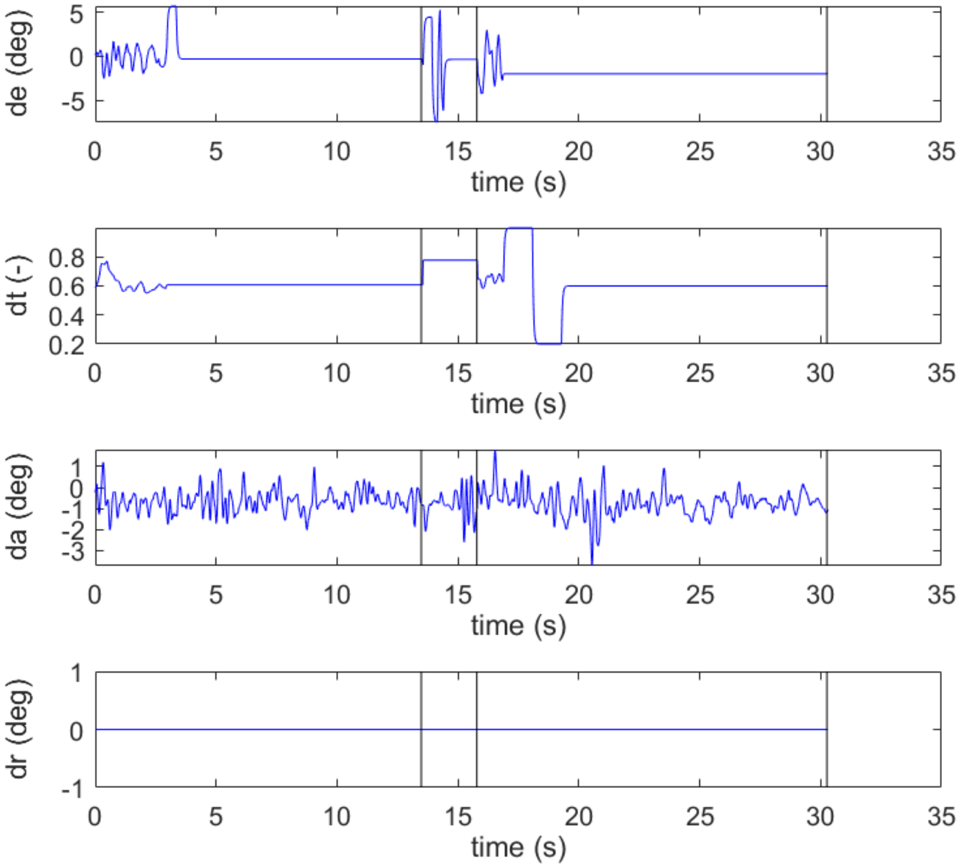

Figure 3.7: Control inputs during the system identification manoeuvre.

The identified aerodynamic parameters for the linear aerodynamic model are presented in the table 3.6. The corresponding eigenvalues for phugoid and short period are found as shown below.

| | |
|---|---|
| **Short period:** | $-1.95 \pm 2.77i$ |
| **Phugoid:** | $-0.043 \pm 0.42i$ |

The values presented above are the dominant pole time constants and damping ratios for the longitudinal dynamics.

Table 3.6: Aerodynamic parameters for linear model

| Term | Value | Term | Value | Term | Value |
|---|---|---|---|---|---|
| $X_0$ | 9.2587 | $Z_0$ | -0.4544E2 | $M_0$ | -2.1589 |
| $X_u$ | -2.2797 | $Z_u$ | -0.0474E2 | $M_u$ | 0.0928 |
| $X_w$ | 1.3422 | $Z_w$ | -0.0904E2 | $M_w$ | -0.5579 |
| $X_q$ | -1.3519 | $Z_q$ | -0.8821E2 | $M_q$ | -6.8804 |
| $X_{de}$ | 27.3732 | $Z_{de}$ | 3.3388E2 | $M_{de}$ | -48.9397 |
| $X_{dt}$ | 51.4792 | | | | |

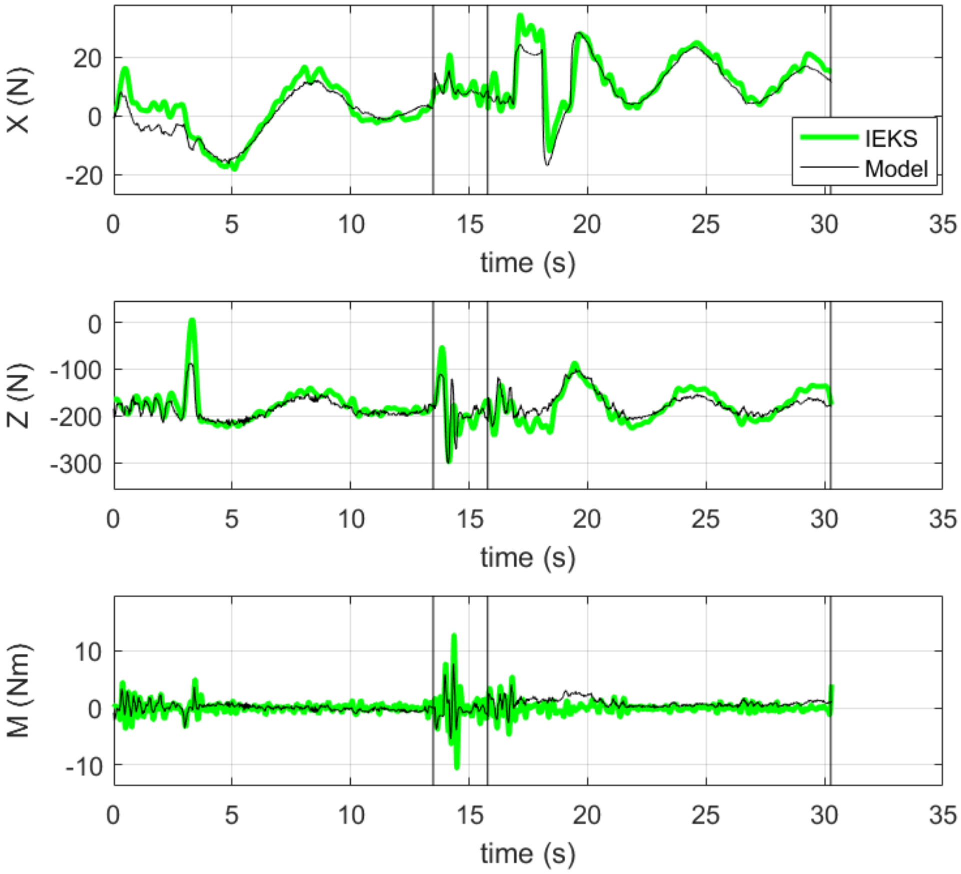

Figure 3.8: Estimated Vs modelled force and moment comparison.

Figure 3.8 compares the IEKS estimate of force and moment to the output of the identified linear aerodynamic model for the validation data set. The statistical metrics for the linear regression on force and moment are presented in table 3.3.3. Overall the $R^2$ values of 0.848, 0.655 and 0.136 are found for X, Z and M respectively with corresponding RMSE values of 4.1 N, 20.63 N and 1.239 Nm. Normalizing over the entire range of the data results in the NRMSE values of 0.078, 0.067 and 0.053

respectively. In conclusion the linear aerodynamic model produces sufficient fit with small NRMSE.

Table 3.7: Averaged R-squared, RMSE and NRMSE for force and moment prediction of linear model.

| Identification | | | | Validation | | | |
|---|---|---|---|---|---|---|---|
| Coef | $X$ | $Z$ | $M$ | Coef | $X$ | $Z$ | $M$ |
| $R^2$ | 0.868 | 0.616 | 0.422 | $R^2$ | 0.848 | 0.665 | 0.1359 |
| RMSE | 3.109 | 19.779 | 1.0899 | RMSE | 4.10 | 20.63 | 1.239 |
| NRMSE | 0.071 | 0.067 | 0.045 | NRMSE | 0.078 | 0.067 | 0.053 |

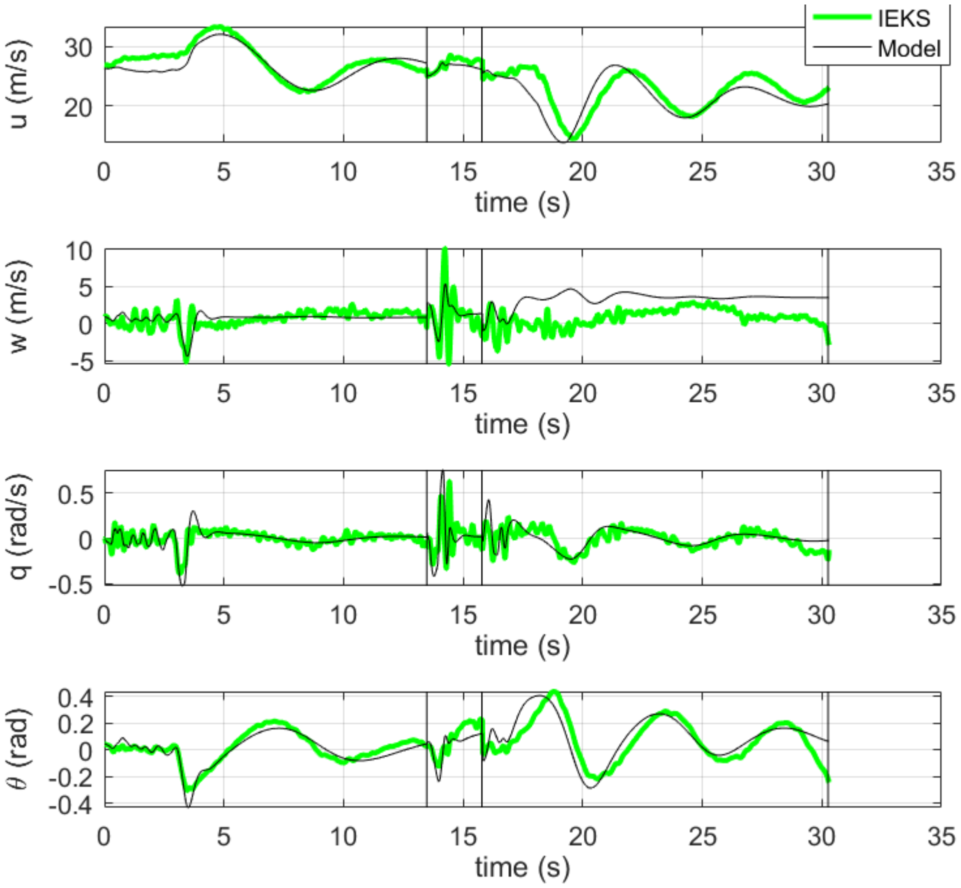

Figure 3.9: Measured vs simulated (linear) responses of aircraft.

In figure 3.9 the measured responses of the aircraft is compared to the simulated responses of the aircraft for the validation data set. The simulated responses are obtained using forward simulation and identified model where inputs were initial conditions and the time history of control inputs. The relevant statistical metrics are presented in the table 3.3.3. TIC values above 0.3 are found in simulation of pitch rate q and z-axis ground velocity w for validation. These are the indications of model deficiency.

Note that the large discrepancies are typically found during the thrust variation manoeuvre where the time lag of the measured responses to the simulated responses lead to an overall mismatch in the period of two signals. Possibly the representation of thrust with a single coefficient using first order Taylor series approximation

Table 3.8: TIC and GOF values for forward simulation with linear model.

| Identification | | | | | Validation | | | | |
|---|---|---|---|---|---|---|---|---|---|
| State | u | w | q | $\theta$ | State | u | w | q | $\theta$ |
| GOF | 0.77 | 0.72 | 0.514 | 0.688 | GOF | 0.76 | 0.52 | 0.52 | 0.72 |
| TIC | 0.03 | 0.28 | 0.355 | 0.254 | TIC | 0.038 | 0.453 | 0.345 | 0.236 |

for the combination of different manoeuvres attribute to errors. In fact TIC and GOF values without the thrust variation manoeuvre indicates a sufficiently accurate model with all TIC $< 0.3$.

## 3.4 Limitations and recommendations

In summary the system identification tool-chain using the two step method is introduced in this chapter. Additionally the application of the tool chain to the Penguin BE UAV is presented while the differences to the Elektra 1 system identification procedures are highlighted. The identified linear model for the longitudinal dynamics of Penguin BE show adequacy in representing phugoid and short period excited with the elevator. However, the identified aerodynamic model show deficiency in fully representing the phugoid excited with thrust variation. Further analysis on instrumentation during sudden changes in also throttle is required.

With direct measurements of angle of attack and side-slip the stability and control derivatives could also be expressed in aerodynamic frame of reference. To the best of author's knowledge, model parameters expressed in the aerodynamic frame of reference are widely used in the aerospace community. It could be one of the future tasks to identify the aerodynamic model parameters using true airspeed, angle of attack and side-slip instead of ground velocities.

Lastly the actuator and the thrust dynamics should be modelled. The actuator dynamics can be modelled as the 2nd order transfer function whereas the thrust dynamics from throttle can be modelled as a 1st order system with time delays. The thrust can also be modelled using the data sheet from the manufacturer as shown in [31].

# Chapter 4

# Global Aircraft System Identification for Elektra 1

Detailed aerodynamic models play a crucial role for flight control systems design. The application of the two step method for local aircraft system identification in chapter 2 resulted in a model valid over a region in the flight envelope close to where the data is collected for aerodynamic parameter identification. A natural further step for modelling is an expansion of this region to the entire flight envelope. The Identification process of such global model is called global aircraft system identification. Note that within the context of the current project the flight envelope is referred to as performance envelope of the aircraft in terms of only altitude and mach number.

A typical global aircraft system identification program in the industry requires an extensive flight test campaign for the collection of data at various points of the flight envelope and repetition of parameter identification locally [10]. Yet, such extensive flight test campaign for stratospheric flight can be costly and time consuming. Extensive wind-tunnel tests and high fidelity CFD based aerodynamic database generation for the entire flight envelope is also not feasible both in cost and time within the scope of the current master thesis project. Furthermore, numerical estimates such as CFD suffer from validity and inadequate theory to represent the complex aerodynamic phenomena while the model scaling, Reynold's number, dynamic derivatives, cross coupling, aero-servo-elastic effects are the typical challenges in producing highly accurate wind-tunnel predictions. Therefore, the method of incremental model update has gained attention since the 1990s.

The incremental model update involves the modelling of correction factors by combining available flight test data and an aerodynamic database where the functional dependencies are mapped through the polynomial expressions. The aircraft model is then updated using such correction factors. Some notable examples of such method can be found in [33, 34]. In [33] the wind tunnel data base for the X-31A research aircraft is supplemented with flight test data by increment to update the aerodynamic coefficients depending on angle of attack and Mach number. The incremental model update was also applied to the Phoenix RLV demonstrator in [34] where landing gear effects was included in addition to the correction of wind-tunnel data. The key idea underling incremental model update is data fusion between wind tunnel derived aerodynamic database with available flight test data. Other works on the incremental model update scheme can be found in [35, 36, 37, 38, 39, 40, 41, 42, 43, 44, 45, 46].

However, the creation of an aerodynamic database for a flying vehicle is a time consuming procedure. As an example the generation of the aerodynamic data base for the phoenix landing experiment required series of wind tunnel experiments which lasted from 1999 to 2003 [34]. Furthermore aerodynamic database generation using wind-tunnels and high fidelity CFD tools are often outside the expertise of the robotics community. Therefore the aim of the current investigation is the preliminary study in applying the method of incremental model update using low fidelity aerodynamic computation tools such as VLM and 3D panel. Note that the scope is limited to low altitude flights in this master thesis project.

A description of incremental model update, collection of data, force and moment estimation and comparison using VLM, correction factor modelling and global aerodynamic model identification using obtained correction model are presented in sections 4.1, 4.2, 4.3, 4.4 and 4.5. The limitations and recommendations for the future work will presented in section 4.6.

## 4.1 Incremental model update scheme

The identification of globally aerodynamic parameters via the incremental model update scheme requires modelling of correction factors (see figure 4.1) and then the aircraft system identification with corrected synthetic or virtual data for various points of flight envelope (figure 4.3). A scheme for computing the aerodynamic parameters from numerical aerodynamic computation tools by applying system identification tools is shown in figure 4.2. Note that aerodynamic data base for dynamic manoeuvres have been developed by other student in the team.

In figure 4.1 the block diagram for modelling of correction factors is depicted. The system identification of correction model involves the direct comparison of force and moment or equivalently the aerodynamic parameters from the flight test data and computed aerodynamic database (see the figure 4.1). The outputs of the block *Parameters from the flight test data* are the aerodynamic parameters from the local system identification and consequently, the model estimate of force and moment. The block *Parameters from the flight test data* uses the available flight test data to obtain the local aerodynamic parameters. In the block *Parameters from VLM*, the VLM computed aerodynamic parameters and also, the VLM prediction of force and moment are computed. Lastly, the block *Identification of correction model* involves the modelling of discrepancies in force and moment from two different above mentioned sources of aerodynamic models. The assumption here is that the errors in VLM estimate of force and moment have deterministic nature which is attributed to the use of potential theory and simplified mesh (a single line of singularities). The main challenge in this method is the investigation of physical parameters or snapshots for the correction model.

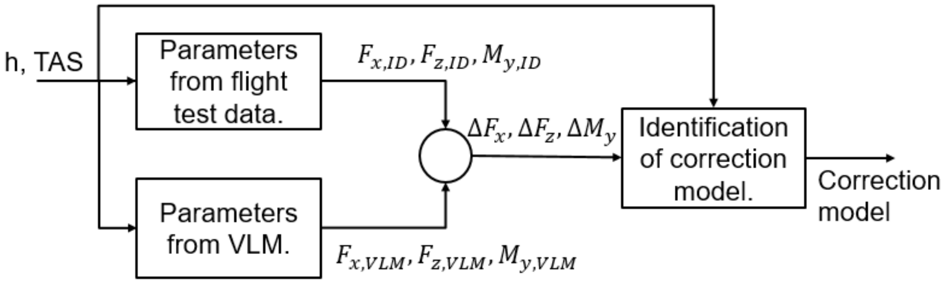
h, TAS
Parameters from flight test data.
$F_{x,ID}, F_{z,ID}, M_{y,ID}$
$\Delta F_x, \Delta F_z, \Delta M_y$
Identification of correction model.
Correction model
Parameters from VLM.
$F_{x,VLM}, F_{z,VLM}, M_{y,VLM}$

Figure 4.1: System identification of correction model.

The scheme for the simulation of system identification manoeuvre with the aerodynamic computational tools is shown in figure 4.2 where the key idea is an attempt to reduce the computational effort by applying system identification techniques to dynamic CFD simulation. In other words the computation of aerodynamic force and moment are restricted to the states that describe the virtual system identification manoeuvre. In figure 4.2 the block *rigid body equation of motion* refers to the simulation of aircraft states via numerical integration of aircraft rigid body equations of motion. For such simulation of the aircraft states the external force and moment acting on the aircraft must be provided. The External force and moment due to propulsion are computed using the performance data provided by the propeller's manufacturer which requires rotational speeds as an input to the look up tables of $C_T$ and $C_P$ [31]. In parallel the aerodynamic force and moment can be computed from either VLM, 3D panel or CFD where control inputs and aircraft states must be provided. Overall the virtual system identification manoeuvre is generated using such scheme where specific control inputs and initial aircraft states corresponding to the trim conditions are provided and, computation of aerodynamic force and moment and numerical integration of rigid body equations are repeated in each time step. More technical details and validation results of the proposed method can be found in [47].

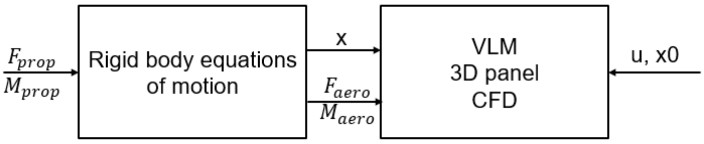

Figure 4.2: Simulation of system identification manoeuvre with the aerodynamic computational tools and the aircraft equations of motion.

The global aircraft system identification can be performed with the scheme shown in figure 4.3. The block *VLM simulation* refers to the scheme shown in figure 4.2 in which the simulation of the aircraft system identification manoeuvres are generated. The outputs of the block *VLM simulation* are the aircraft state, and aerodynamic force and moment. Parameter identification using the tools from the linear regression theory can then be applied to obtain the aerodynamic parameters. This step is performed in the block *Parameter identification.* With this method the aerodynamic parameters over all the operating points of an aircraft can be obtained. However, its drawback is the inaccuracy when the aerodynamic computational tool is limited to VLM, 3D panel method or even low fidelity CFD. Therefore, the correction model can be applied to increase the accuracy. The expected outcome is a global aerodynamic model for different altitudes and speeds.

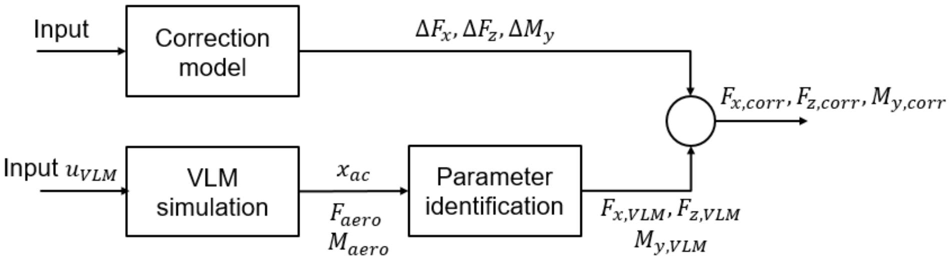

Figure 4.3: Scheme for global system identification.

## 4.2 Flight test design and data gathering

The goal of flight testing is the implementation and validation of the new incremental model update scheme presented in section 4.1. As a first step to achieving the current goal, the scope of the data gathering campaign has been limited to low altitude symmetric flight conditions at different trim settings with four different velocities as shown in figure 4.4.

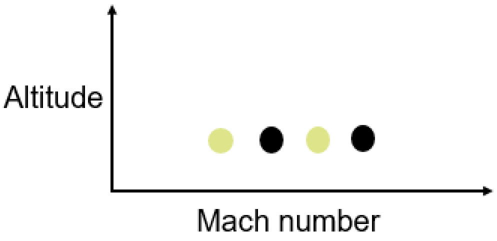

Figure 4.4: Selected flight envelope for the preliminary study on incremental update

The selected trim velocities were 22 m/s, 26 m/s, 28 m/s and 30 m/s whereas the altitude was set to 1000 m above the mean sea level. This results in collection of data at four different trim conditions. In this way the trim conditions (h,TAS) = (1000,22) and (h,TAS) = (1000,28) can be used for modelling of correction factors which are denoted as green dots in figure 4.4. On the other hand the trim conditions (h,TAS) = (1000,26) and (h,TAS) = (1000,30) can be used for the validation of the correction factors. These trim conditions are denoted as black dots in figure 4.4. Consequently applying the schemes shown in figures 4.2 and 4.3 would result in stability and control derivatives of the aircraft valid over the regions around the selected trim points.

## 4.3 Parameter identification with VLM simulation

This section describes the results of parameter identification based on VLM simulation. Again, the detailed information about VLM simulation can be found in [47]. Instead of using flight test data, the data from VLM simulation has been used for parameter identification. In other words the linear regression tools were applied to the AVL [48] generated aerodynamic force and moment using the simulated states of the aircraft. The linear aerodynamic model structure has been used. The results are shown below in figure 4.5.

The $R^2$ values of 0.931, 0.98 and 0.94 have been reported which is an indication of good fit. In comparison to an identification based on real flight test data, the parameter identification with the simulated data produces better fit due to the absence of noises and external disturbances. Note that the aerodynamic force and moment shown in figure 4.5 is normalized using the equations below. $\rho$, $V$, $S$ and $c$ are air density, true airspeed, wing surface area and mean chord respectively.

$$C_x = \frac{F_x}{\frac{1}{2}\rho V^2 S} \tag{4.1}$$

$$C_z = \frac{F_z}{\frac{1}{2}\rho V^2 S} \tag{4.2}$$

$$C_m = \frac{M_y}{\frac{1}{2}\rho V^2 S c} \tag{4.3}$$

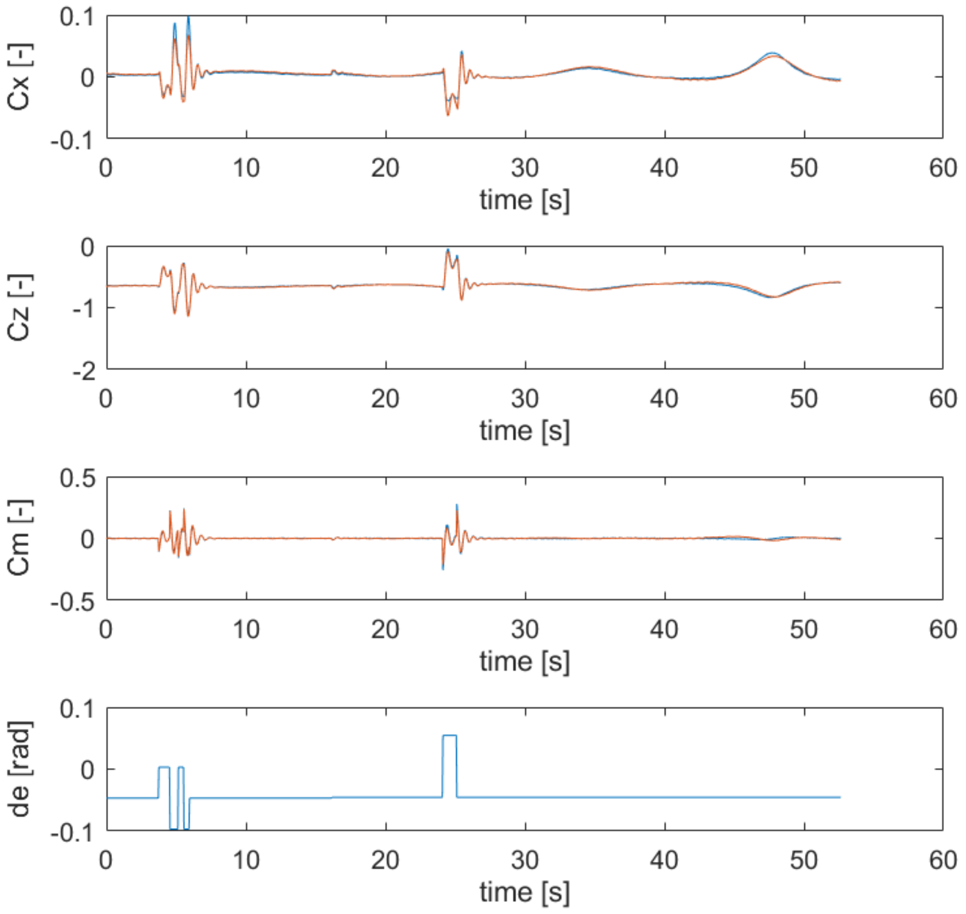

Figure 4.5: Aerodynamic force and moment from VLM compared to modelled aerodynamic force and moment where parameter identification is applied to the data from VLM simulation.

Table 4.1: Identified model parameters using VLM based simulation data (ID) compared to direct output of VLM software (AVL).

**ID:**

| **Term** | **Value** | **Term** | **Value** | **Term** | **Value** |
|---|---|---|---|---|---|
| $C_{x_u}$ | -0.004 | $C_{z_u}$ | -0.036 | $C_{m_u}$ | 0.0105 |
| $C_{x_w}$ | 0.0405 | $C_{z_w}$ | -0.231 | $C_{m_w}$ | -0.095 |
| $C_{x_q}$ | 0.0026 | $C_{z_q}$ | -0.08595 | $C_{m_q}$ | -0.196 |
| $C_{x_{de}}$ | 0.00059 | $C_{z_{de}}$ | -0.0097 | $C_{m_{de}}$ | -0.047 |

**AVL:**

| **Term** | **Value** | **Term** | **Value** | **Term** | **Value** |
|---|---|---|---|---|---|
| $C_{x_u}$ | -0.004 | $C_{z_u}$ | -0.04 | $C_{m_u}$ | 0.011 |
| $C_{x_w}$ | 0.045 | $C_{z_w}$ | -0.25 | $C_{m_w}$ | -0.105 |
| $C_{x_q}$ | 0.0029 | $C_{z_q}$ | -0.0955 | $C_{m_q}$ | -0.218 |
| $C_{x_{de}}$ | 0.00054 | $C_{z_{de}}$ | -0.0088 | $C_{m_{de}}$ | -0.0431 |

Lastly, the identified parameters have been verified using the AVL computed stability and control derivatives which are a direct output of the software. Good agreement has been found between the two (see table 4.1). In case of VLM softwares such as AVL is available to output the state space equations of the aircraft, from where stability and control derivatives could be extracted manually using the corresponding trim conditions. Yet, the current method will reduce the computational effort and time when the software is not equipped to directly output the state space representation of the aircraft.

## 4.4 Correction model identification

This section presents the identification of the correction model which must capture the deficiency of VLM in a polynomial. The following steps are taken in correction model identification.

1. Local system identification at each trim condition using the flight test data. Note that moments are neglected due to bad quality of data (e.g, low signal to noise ratio in pitch rate as the pilot executed elevator deflection less than 2 degrees and thermal up-draft during the test day).
2. Parameter identification using VLM simulation data. This step has to be repeated at each available point in the flight envelope.
3. Comparison of stability and control derivatives between the parameters obtained using flight test data (FD-ID) and the parameters obtained using VLM simulation data (VLM-ID). The differences between FD-ID and VLM-ID parameters is being modelled.
4. Identification of correction model using the least squares method. The physical snapshots or independent variable chosen here is true airspeed.

Figure 4.6 shows the results of local system identification at each trim conditions using the flight test data. The yellow line shows the IEKS estimate of forces whereas the red line depicts the estimation of forces using the identified model. The figure 4.6 is separated by 4 vertical bars for 4 trim conditions (26m/s, 23m/s, 28m/s and 30m/s sequentially).

The RMSE values for each trim conditions (called V1, V2, V3 and V4 referring 26m/s, 23m/s, 28m/s and 30m/s respectively) to as well as combining all the trim conditions (ALL). See table 4.2 Note that the reported RMSE values may depend on the portion of the data used for computation and therefore, RMSE has been used as a metrics to compare the accuracy of the different models.

Table 4.2: RMSE values corresponding to figure 4.6 or FD-ID.

| | V1 | V2 | V3 | V4 | ALL |
|---|---|---|---|---|---|
| RMSE $F_x$ | 62.2 | 89.8 | 76.5 | 38.1 | 71.5 |
| RMSE $F_z$ | 146.5 | 225.0 | 175.2 | 212.8 | 204.3 |

Similarly figure 4.7 compares the IEKS estimate of forces to the estimation of forces using VLM. The input to the VLM model is the time history of longitudinal aircraft states for the linear aerodynamic model. The discrepancy found between the two must be captured in the correction model.

In table 4.3 the RMSE values for VLM-ID model are presented. As expected larger RMSE values are found when compared to FD-ID model which is shown in the table 4.2.

These differences in RMSE values attribute to errors in the stability and control derivatives estimated from VLM-ID. These errors in the stability and control derivatives can result from various assumptions made in the potential flow theory. The

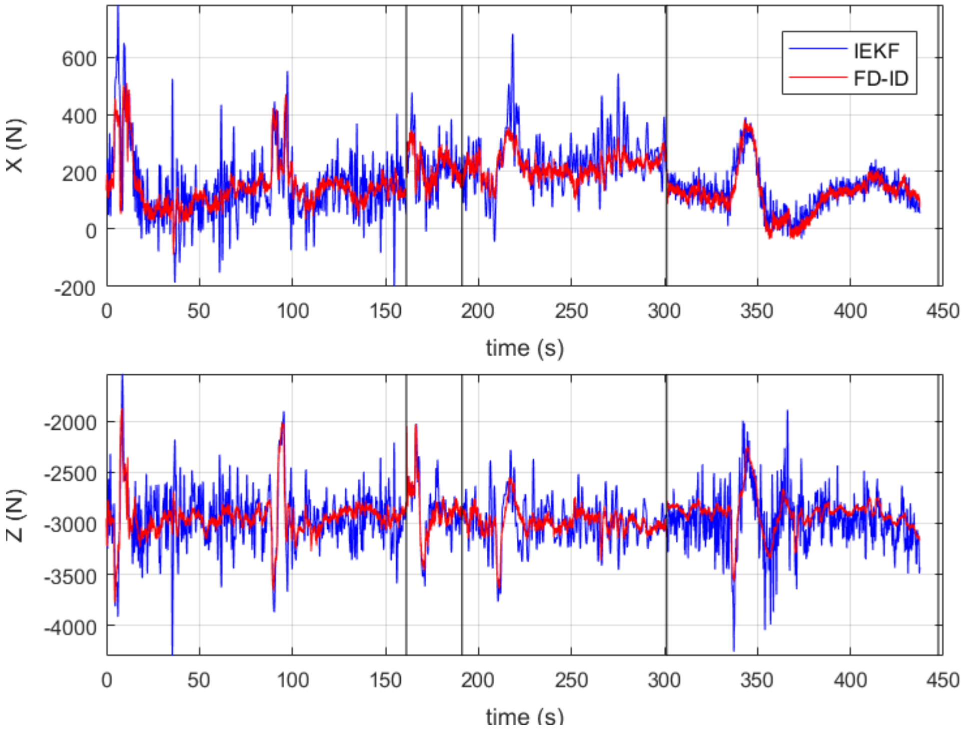

Figure 4.6: Comparison of IEKS forces and force estimation using identified model with flight test data.

Table 4.3: RMSE values corresponding to figure 4.7 or VLM-ID.

| | V1 | V2 | V3 | V4 | ALL |
|---|---|---|---|---|---|
| RMSE $F_x$ | 1.4504E2 | 1.651E2 | 1.421E2 | 1.263E2 | 1.468E2 |
| RMSE $F_z$ | 7.616E2 | 1.0827E3 | 7.818E2 | 8.879E2 | 9.329E2 |

stability and control derivatives obtained from FD-ID are the maximum likelihood estimates for the given data-set. Figures below shows the comparison of VLM-ID and FD-ID derivatives and also, their discrepancies in the function of velocity.

One of the critical assumptions of the current method is the validity of flight test data and methods in local system identification that were applied to estimate and model the aerodynamic forces and moments. In other words the IEKS estimate of forces and moments are assumed to be accurate and local parameter identification is performed correctly. Additionally the corrected VLM-ID parameters will not outperform the FD-ID parameters.

It can be seen that VLM-ID parameters scale linearly with velocity. In most of the cases, the error between VLM-ID and FD-ID coefficients are also linear with respect to the true airspeed. Note that $X_{de}$ and $X_q$ are negligible due to their small contribution to $F_x$. The error on $Z_{de}$ are quadratic with respect to true airspeed.

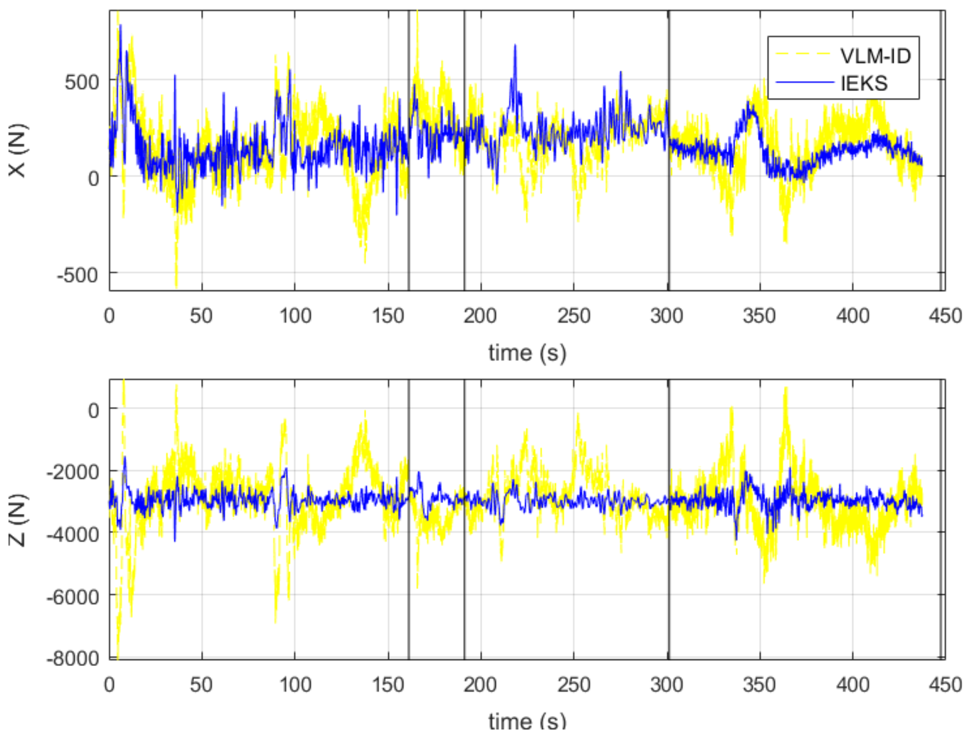

Figure 4.7: Comparison of IEKS forces and force estimation using identified model with VLM simulation.

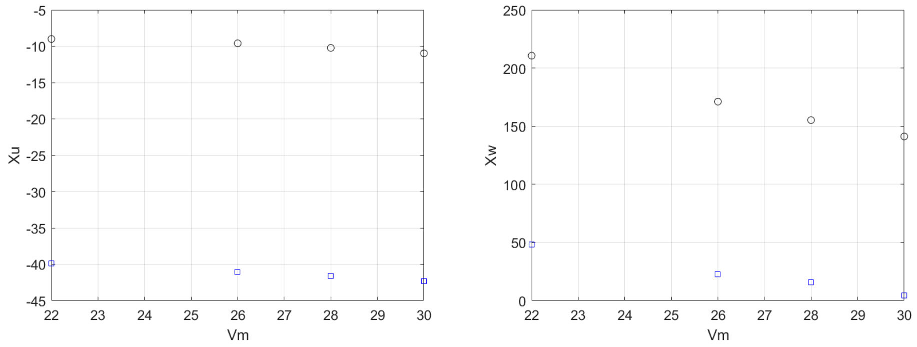

Figure 4.8: FD-ID (blue) vs VLM-ID (black) for $X_u$ and $X_w$.

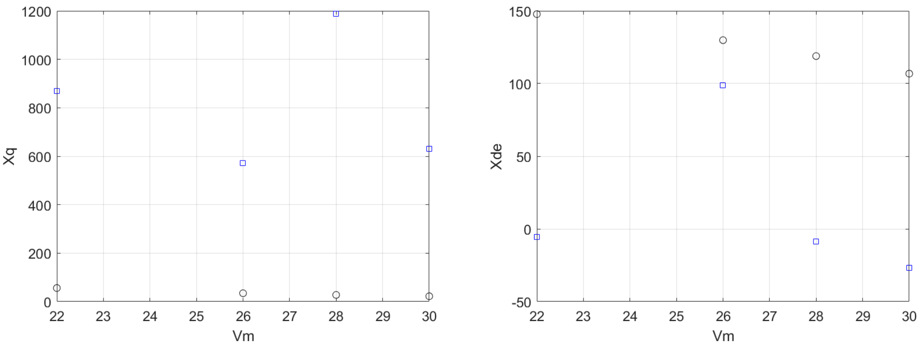

Figure 4.9: FD-ID (blue) vs VLM-ID (black) for $X_q$ and $X_{de}$.

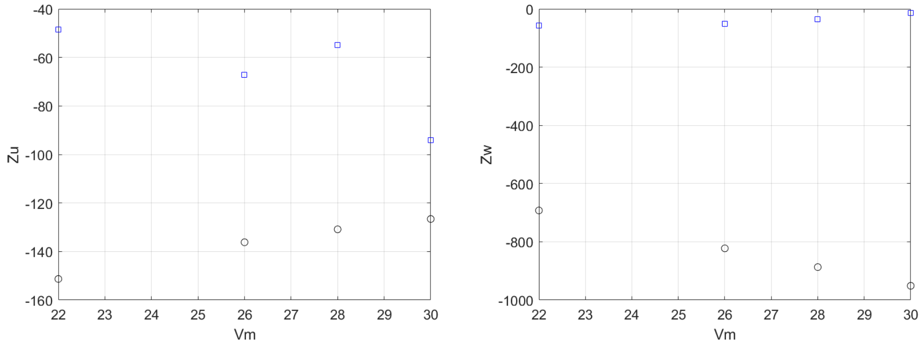

Figure 4.10: FD-ID (blue) vs VLM-ID (black) for $Z_u$ and $Z_w$.

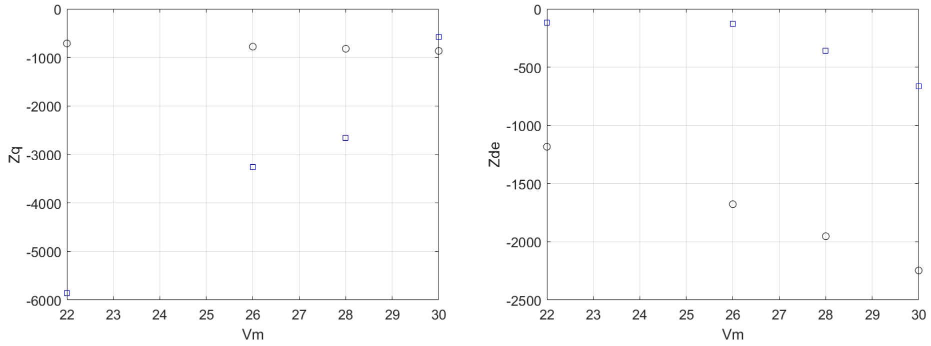

Figure 4.11: FD-ID (blue) vs VLM-ID (black) for $Z_q$ and $Z_{de}$.

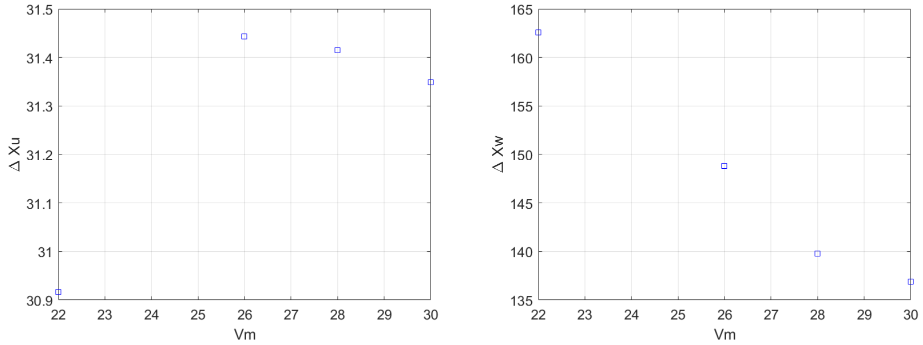

Figure 4.12: Difference between FD-ID and VLM-ID parameters for $X_u$ and $X_w$.

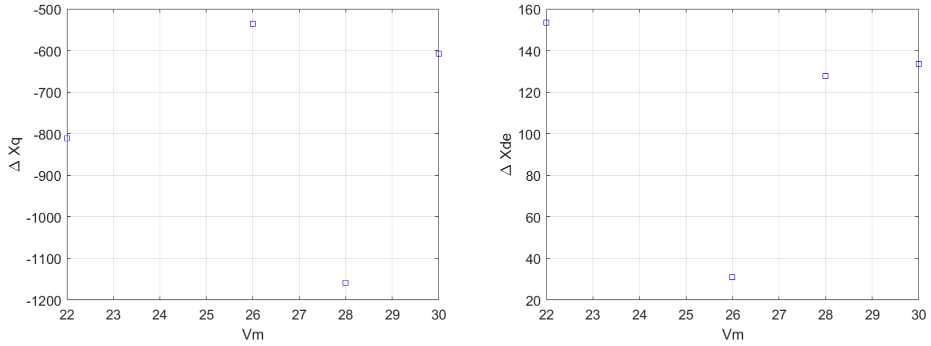

Figure 4.13: Difference between FD-ID and VLM-ID parameters for $X_q$ and $X_{de}$.

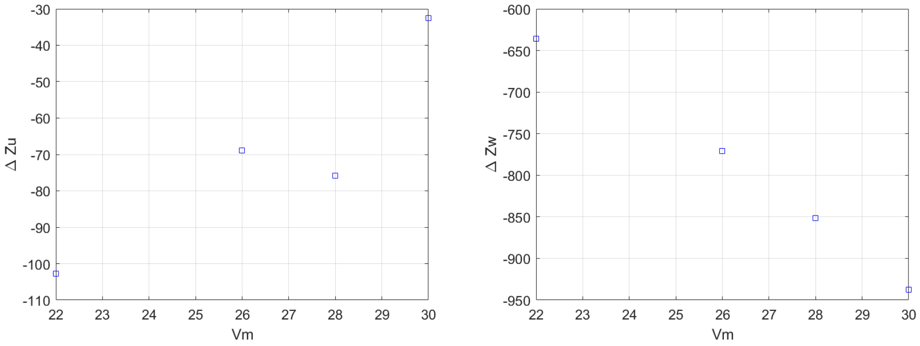

Figure 4.14: Difference between FD-ID and VLM-ID parameters for $Z_u$ and $Z_w$.

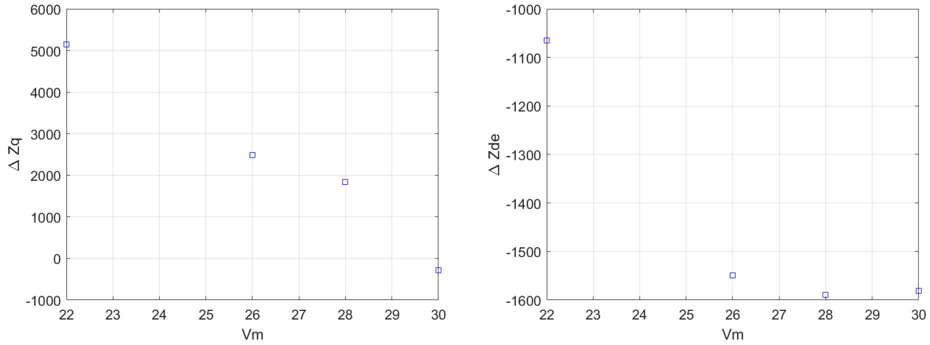

Figure 4.15: Difference between FD-ID and VLM-ID parameters for $Z_q$ and $Z_{de}$.

Note that V1 and V3 were used to compute the correction model whereas V2 and V4 were used for validation. The least squares method were applied to fit the error between FD-ID and VLM-ID parameters with only true airspeed using the training set. Equation 4.4 shows the resulting correction model.

$$\begin{aligned}
\mathit{\Delta} X_u &= 0.083 \cdot V_m + 29.088 \\
\mathit{\Delta} X_w &= -3.790 \cdot V_m + 246 \\
\mathit{\Delta} X_q &= -57.9 \cdot V_m + 462 \\
\mathit{\Delta} X_{de} &= -4.3 \cdot V_m + 248 \\
\mathit{\Delta} Z_u &= 4.4 \cdot V_m - 201.3 \\
\mathit{\Delta} Z_w &= -36 \cdot V_m + 156 \\
\mathit{\Delta} Z_q &= -552 \cdot V_m + 1729.8 \\
\mathit{\Delta} Z_{de} &= -1.39 \cdot V_m^2 - 17.82 \cdot V_m
\end{aligned} \tag{4.4}$$

The correction model presented in equation 4.4 can be used to correct the VLM-ID parameters by using them as biases.

## 4.5 Correction model validation

In figure 4.16 comparison between IEKS estimates of forces and force estimation using the corrected VLM-ID parameters are presented whereas their RMSE values are shown in table 4.4.

Note that the bias terms have not been modelled in VLM-ID parameters. The bias terms are chosen by matching the first point of the force estimation from the corrected VLM-ID parameters to the first point of the IEKS estimation. The bias term can also be corrected. However, the bias term was not corrected in this master thesis project. This is because the trim conditions were not maintained by the pilot

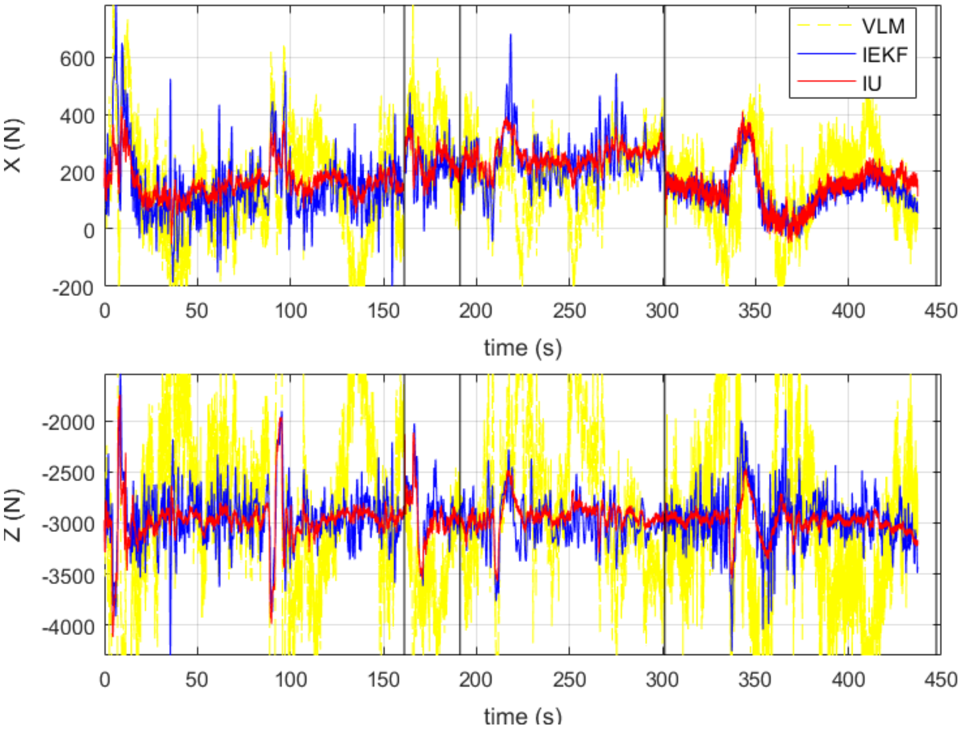

Figure 4.16: Comparison of IEKS forces and force estimation using corrected VLM-ID parameters.

for a long enough time and therefore, the author was uncertain about the exact trim force and moment. Figure 4.16 shows clear improvement of the VLM-ID parameters by adding the correction model. See figures and 4.6 and 4.7 for comparison. Improvement in corrected VLM-ID parameters can be quantified by comparing tables 4.4 and 4.3. The overall RMSE has significantly decreased for both $F_x$ and $F_z$. Furthermore the RMSE values for V2 demonstrates interpolation capabilities of the correction model whereas the RMSE values for V4 dictates extrapolation capabilities. By comparing tables 4.2, 4.3 and 4.4 it can be concluded that the correction model improves the VLM-ID parameters both at interpolation and extrapolation points.

Table 4.4: V1 and V3 as the training set and V2 and V4 as the validation set. RMSE values reported.

| | V1 | V2 | V3 | V4 | ALL |
|---|---|---|---|---|---|
| RMSE $F_x$ | 86.6 | 97.9 | 74.2 | 43.0 | 75.4 |
| RMSE $F_z$ | 169.7 | 238.4 | 188.4 | 209.1 | 212.8 |

This method of incremental model update scheme can be further tested by using different combinations of training and validation sets as listed below.

1. **V2 and V4 for training the correction model and V1 and V3 for validation.** This is to verify the direction of the correction model. (Case study A)
2. **V1 and V2 for training the correction model and V3 and V4 for validation.** This is to verify the pure extrapolation capabilities of the correction

model. (Case study B)

3. **V2 and V3 for training the correction model and V1 and V4 for validation.** This is to verify the pure extrapolation capabilities and direction of the extrapolation. (Case study C)

4. **V1 and V4 for training the correction model and V2 and V3 for validation.** This is to verify the pure interpolation capabilities of the correction model. (Case study D)

The results are summarized in table 4.5 and comparison plots can be found in figures 4.17, 4.18, 4.19 and 4.20.

Table 4.5: Case studies with various choice of training and validation set.

| **Case A** | V1 | V2 | V3 | V4 | ALL |
|---|---|---|---|---|---|
| RMSE $F_x$ | 81.6 | 90.6 | 73.8 | 37.2 | 70.8 |
| RMSE $F_z$ | 227.3E | 226.2 | 205.7 | 204.5 | 215.1 |
| **Case B** | V1 | V2 | V3 | V4 | ALL |
| RMSE $F_x$ | 80.8 | 99.3 | 78.7 | 50.7 | 77.4 |
| RMSE $F_z$ | 169.7 | 226.2 | 223.6 | 240.6 | 225.7 |
| **Case C** | V1 | V2 | V3 | V4 | ALL |
| RMSE $F_x$ | 86.8 | 97.7 | 74.2 | 37.2 | 74.1 |
| RMSE $F_z$ | 371.0 | 235.9 | 188.4 | 204.5 | 232.9 |
| **Case D** | V1 | V2 | V3 | V4 | ALL |
| RMSE $F_x$ | 83.7 | 99.4 | 85.4 | 83.9 | 88.1 |
| RMSE $F_z$ | 180.2 | 226.2 | 188.4 | 217.0 | 211.2 |

The results of the case study A should be compared to the results presented in table 4.4 to analyze the direction of the incremental model update scheme. By comparing the RMSE values presented in tables 4.5 and 4.4 it can be observed that the RMSE values do not change significantly. Therefore, the correction model does not depend on direction within this preliminary study of a new incremental model update scheme.

The case study B is to study the pure extrapolation capabilities of the incremental model update scheme. Overall RMSE has increased from 70.841N to 77.422N, and 2.151E2 N to 2.2257E2 N for $F_x$ and $F_z$ respectively (compared to case A). This is expected as FD-ID stability and control derivatives do not always scale linearly with velocity. The case study C can be compared to the case study B to analyze the direction of the pure extrapolation. For V1 and V2 the correction model in case B outperforms the correction model from case C slightly. At the same time, the correction model in case B is outperformed by the correction model from case C for V3 and V4. This is expected as the correction model is more accurate for trim conditions used for its training. Yet, minimal differences are found in overall RMSE and therefore, the direction does not largely influence the directional capabilities of the correction model within this preliminary study.

Lastly the results of case D show that overall RMSE has increased to 88.115 N for $F_x$ while the RMSE value for $F_z$ stayed relatively close to other cases. The results of the current study show that the prediction capabilities of the correction model in the pure interpolation deteriorate for $F_x$.

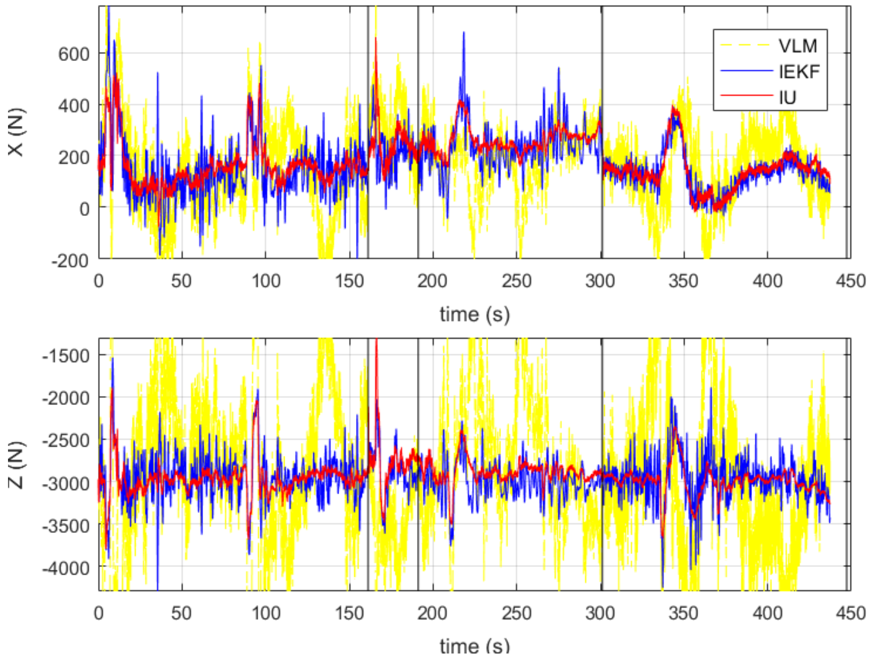

Figure 4.17: Comparison of IEKS forces and force estimation using corrected VLM-ID parameters. Case study A.

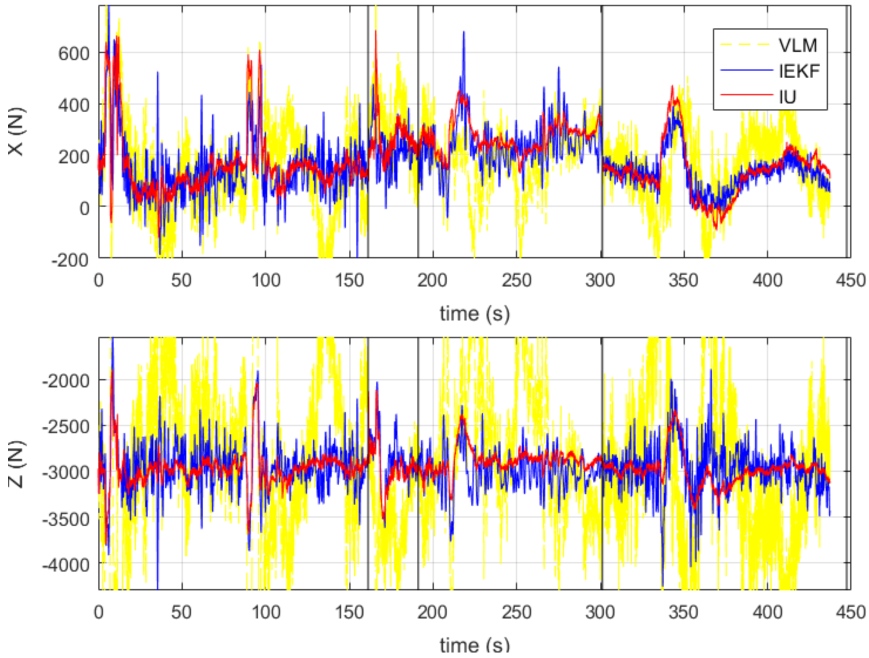

Figure 4.18: Comparison of IEKS forces and force estimation using corrected VLM-ID parameters. Case study B.

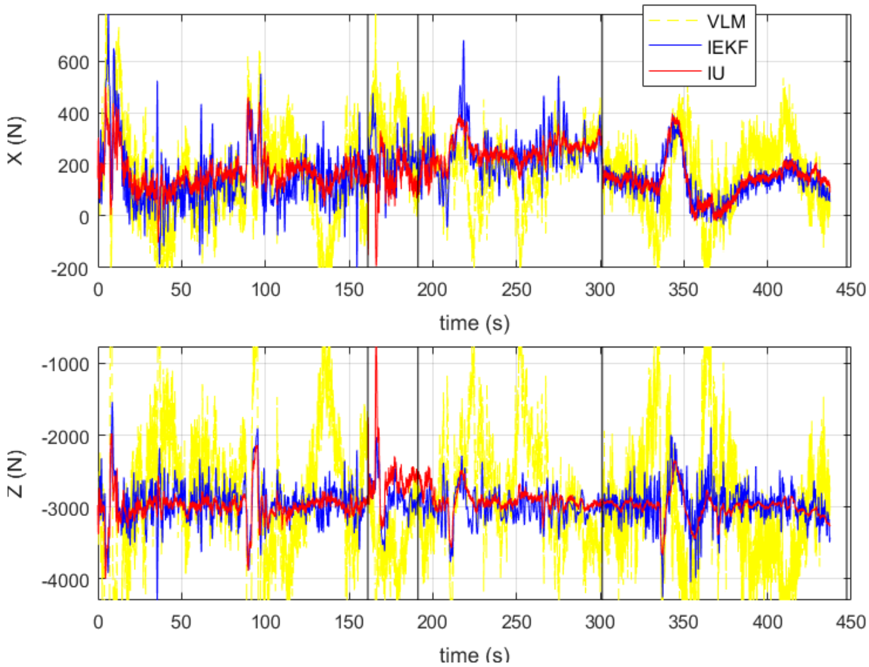

Figure 4.19: Comparison of IEKS forces and force estimation using corrected VLM-ID parameters.Case study C.

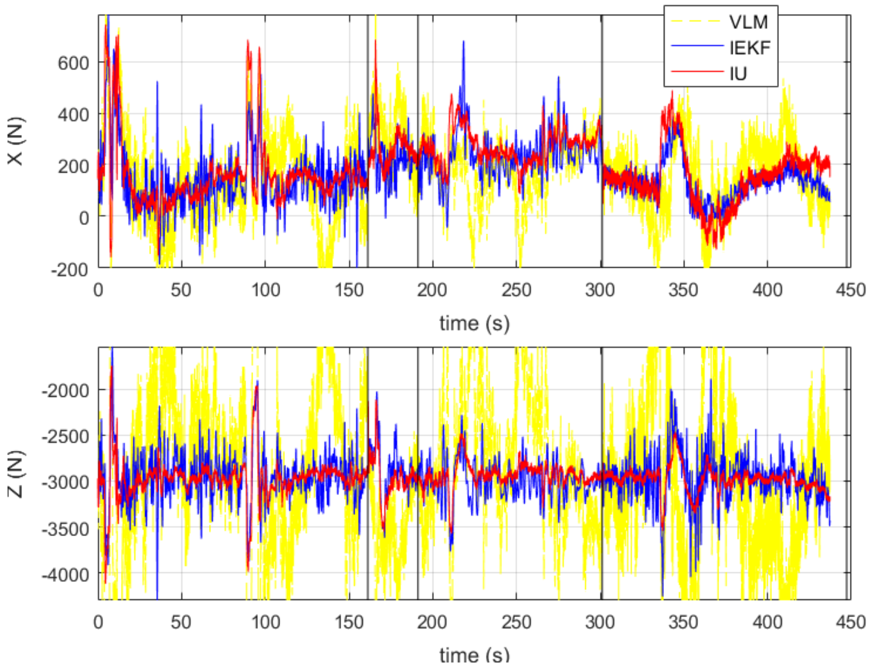

Figure 4.20: Comparison of IEKS forces and force estimation using corrected VLM-ID parameters. Case study D.

## 4.6 Limitations and future works

This chapter presents a preliminary study on the global system identification methods based on incremental model update. Firstly the aerodynamic parameters are estimated by applying system identification to VLM based simulation data which constitutes of the aerodynamic force and moment which are a direct output of AVL, and relevant states of the aircraft that represents multi-step based aircraft system identification manoeuvres. The results of parameter identification using VLM simulation data have been verified using precomputed stability and control derivatives from AVL. In the next step series of local system identification at 4 different trim conditions was performed using the two step method. These data sets were used to study the incremental model update scheme with low fidelity aerodynamic data base. The scope of the study has been limited to low altitude flights with 4 different true air speeds.

The stability and control derivatives from VLM were less accurate than the same parameters found from flight test data. A correction model were built assuming that certain discrepancies of VLM derived parameters are systematic. Least squares were applied to the errors between VLM and flight test derived parameters. The obtained correction model were used to correct VLM derived aerodynamic parameters. The corrected aerodynamic derivatives were evaluated using the flight test data and improvements on prediction accuracy have been reported. The interpolation and extrapolation capabilities of the proposed scheme was further analyzed and evaluated by choosing various combinations of training and validation set. The study has shown that the proposed scheme can be used to improve the aerodynamic model outside the point where flight test data were collected for variations of true airspeed in the region of low altitude flights.

The magnitude of the control inputs used for collection of flight test data was insufficient to clearly detect the modes of the aircraft. Furthermore significant thermal up-drifts were present during the flights. It is recommend to improve the flight test procedures for Elektra 1 system identification experiments. Larger deflections of control surfaces are required to strongly excite the modes of the aircraft. Lastly short period and thrust variation manoeuvres can be collected at each velocity and used to further study the proposed scheme at low altitude.

It is highly recommended to find existing data set to further validate the scheme, not only at low altitude but also for stratospheric flights. With vast amount of data with variations in flight condition the scope of the method can be expanded.

# Chapter 5

# Conclusion

The local aircraft system identification based on the two step method has been implemented and validated for Elektra 1. For data gathering the multi-step control inputs that excites the longitudinal modes of aircraft have been designed and executed in flight. The obtained data were processed with the iterative extended Kalman filter with backward Kalman smoothing (flight path reconstruction). This ensured that (1) the instrumentation errors are determined and (2) the smoothed estimate of the aircraft states, forces and moments are obtained. Then the method of least squares was applied to the processed data and the aerodynamic parameters could be identified. The obtained parameters and consequently, the aerodynamic model were validated by comparing their prediction capabilities of the aerodynamic forces and moments. The identified parameters were further validated using the forward simulation of the aircraft states. Evaluating the results with relevant statistical metric on the validation set, it has shown that the identified parameters represent the aircraft dynamics in high accuracy.

One of the initial goals were the development of a system identification procedure that can be applied to various fixed wing platforms in the Flying Robots Group of the Robotics and Mechatronics Center. The algorithms for the two step method have been implemented as the system identification tool chain and its applicability to Penguin BE UAV has been demonstrated. The available avionics, instrumentation and technical readiness of the system made the system identification for Penguin BE differ from Elektra 1 in practice. These differences to the local aircraft system identification for Elektra 1 were documented and therefore, a technical know-how could be accumulated.

The output of the global system identification is a model which is valid at all the operating points of the flight envelope. As High Altitude Long Endurance platforms exhibit the vast ranges of the operating points, the development of the global system identification procedures was an obvious next step. In order to reduce the cost and time associated with the conventional approaches, an incremental model update based scheme for the global system identification has been devised and implemented. The method involved the use of Vortex Lattice Method (VLM) instead of the wind-tunnel experiments and the Computational Fluid Dynamics for the prediction of the aerodynamic phenomena. Furthermore the parameter identification was applied to the data obtained from the VLM based simulation of aircraft system identification manoeuvres. As VLM lacks the accuracy, the available flight test data were used to correct the aerodynamic parameters derived using VLM. Within the scope (low altitude flights at 4 different velocities) the method proved to work with improvements in the Root Mean Squared Error values by factor 2 and 5 for forces along the x-axis and z-axis in body frame.

One of the key future work is the development of a validation method for the

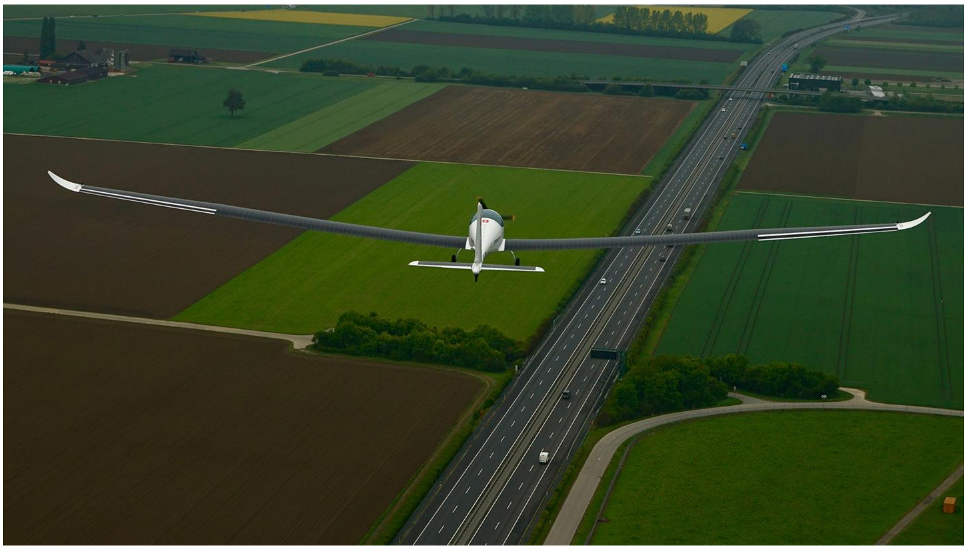

Figure 5.1: Elektra 2 - maiden flight [2].

controller synthesis. Perhaps, the flight experiments involving the step responses of the aircraft can be performed and further compared to the model predicted step responses of the aircraft. Furthermore the level of fidelity can be defined specifically for the control architecture being used in the Flying Robots Group.

The high fidelity modelling activities can be extended further. One of the possibility is the high fidelity modelling for Elektra 2 in figure 5.1 by applying the system identification tool chain based on the two step method. In case the the effects of the aero-elasticity is found to be dominant the system identification methods for the flexible aircraft could be implemented.

The aerodynamic phenomena in the stratospheric flight is characterized by a low Reynolds number and also, a high Mach number. Furthermore, VLM is based on the assumption of incompressible flow. Therefore, the method for the global system identification must be further studied by expanding the scope. It is highly recommended to further develop methods with the wider ranges of velocity and altitude.

# Bibliography

[1] A. Noth, "Design of Solar Powered Airplanes for Continous Flight," Ph.D. dissertation, Eidgenössische Polytechnische Schule Zurich, Zürich, 2008.

[2] "Project solarstratos website," https://www.solarstratos.com/en/, accessed: 2017-02-13.

[3] A. Klockner, *Geometry Based Flight Dynamics Modelling of Unmanned Airplanes*, ser. Guidance, Navigation, and Control and Co-located Conferences. American Institute of Aeronautics and Astronautics, Aug 2013, 0.

[4] T. Muskardin, G. Balmer, S. Wlach, K. Kondak, M. Laiacker, and A. Ollero, "Landing of a fixed-wing uav on a mobile ground vehicle," in *2016 IEEE International Conference on Robotics and Automation (ICRA)*, May 2016, pp. 1237–1242.

[5] T. Muskardin, G. Balmer, L. Persson, S. Wlach, M. Laiacker, A. Ollero, and K. Kondak, "A novel landing system to increase payload capacity and operational availability of high altitude long endurance uavs," *Journal of Intelligent & Robotic Systems*, pp. 1–22, 2017.

[6] "Elektrasolar gmbh website," https://www.elektra-solar.com/, accessed: 2017-02-13.

[7] "Uav factory website," http://www.uavfactory.com/prodcat/67, accessed: 2017-02-13.

[8] D. J. Grymin and M. Farhood, "Two-step system identification and trajectory tracking control of a small fixed-wing uav," *Journal of Intelligent & Robotic Systems*, vol. 83, no. 1, pp. 105–131, 2016.

[9] T. Lombaerts, *Aerodynamic Model Identification of Frauke UAV*, ser. Guidance, Navigation, and Control and Co-located Conferences. American Institute of Aeronautics and Astronautics, Aug 2012, 0.

[10] R. V. Jategaonkar, Ed., *Flight Vehicle System Identification: A Time-Domain Methodology, Second Edition.* American Institute of Aeronautics and Astronautics, Inc., 2015.

[11] J. Oliveira, Q. P. Chu, J. A. Mulder, H. M. N. K. Balini, and W. G. M. Vos, *Output Error Method and Two Step Method for Aerodynamic Model Identification*, ser. Guidance, Navigation, and Control and Co-located Conferences. American Institute of Aeronautics and Astronautics, Aug 2005, 0.

[12] V. Klein and E. Morelli, *Aircraft System Identification: Theory and Practice*, ser. AIAA education series. American Institute of Aeronautics and Astronautics, 2006.

[13] L. Ljung, Ed., *System Identification (2Nd Ed.): Theory for the User.* Upper Saddle River, NJ, USA: Prentice Hall PTR, 1999.

[14] R. Vepa, Ed., *Flight Dynamics, Simulation, and Control: For Rigid and Flexible Aircraft.* CRC Press, 2014.

[15] E. Plaetschke and G. Schulz, *Practical Input Signal Design.* AGARD LS-104, Paper 3, Nov 1979.

[16] H. Stalford, *High-alpha aerodynamic model identification of the T-2C aircraft using the EBM system identification method*, ser. Aerospace Sciences Meetings. American Institute of Aeronautics and Astronautics, Jan 1980, 0.

[17] H. L. Stalford, "High-alpha aerodynamic model identification of t-2c aircraft using the ebm method," *Journal of Aircraft*, vol. 18, no. 10, pp. 801–809, Oct 1981.

[18] J. C. Hoff and M. V. Cook, "Aircraft parameter identification using an estimation-before-modelling technique," *The Aeronautical Journal (1968)*, vol. 100, no. 997, p. 259–268, 1996.

[19] B. Stevens, F. Lewis, and E. Johnson, *Aircraft Control and Simulation: Dynamics, Controls Design, and Autonomous Systems.* Wiley, 2015.

[20] J. R. Raol, G. Girija, and J. Singh, *Modelling and Parameter Estimation of Dynamic Systems*, ser. Control, Robotics and Sensors. Institution of Engineering and Technology, 2004.

[21] B. O. Teixeira, L. A. Tôrres, P. Iscold, and L. A. Aguirre, "Flight path reconstruction – a comparison of nonlinear kalman filter and smoother algorithms," *Aerospace Science and Technology*, vol. 15, no. 1, pp. 60 – 71, 2011.

[22] J. Mulder, Q. Chu, J. Sridhar, J. Breeman, and M. Laban, "Non-linear aircraft flight path reconstruction review and new advances," *Progress in Aerospace Sciences*, vol. 35, no. 7, pp. 673 – 726, 1999.

[23] T. A. Johansen, A. Cristofaro, K. Sørensen, J. M. Hansen, and T. I. Fossen, "On estimation of wind velocity, angle-of-attack and sideslip angle of small uavs using standard sensors," in *2015 International Conference on Unmanned Aircraft Systems (ICUAS)*, June 2015, pp. 510–519.

[24] L. Ljung, "Asymptotic behavior of the extended kalman filter as a parameter estimator for linear systems," *IEEE Transactions on Automatic Control*, vol. 24, no. 1, pp. 36–50, Feb 1979.

[25] T. Westerlund and A. Tysso, "Remarks on "asymptotic behavior of the extended kalman filter as a parameter estimator for linear systems"," *IEEE Transactions on Automatic Control*, vol. 25, no. 5, pp. 1011–1012, Oct 1980.

[26] Y. Bar-Shalom and X.-R. Li, *Estimation with Applications to Tracking and Navigation.* New York, NY, USA: John Wiley & Sons, Inc., 2001.

[27] T. Kailath, "An innovations approach to least-squares estimation–part i: Linear filtering in additive white noise," *IEEE Transactions on Automatic Control*, vol. 13, no. 6, pp. 646–655, Dec 1968.

[28] A. Rencher, *Methods of Multivariate Analysis*, ser. Wiley Series in Probability and Statistics. Wiley, 2003.

[29] "Federal aviation administration website," https://www.faa.gov/about/initiatives/nsp/, accessed: 2017-05-01.

[30] FAA, "Airplane simulator qualification," FAA Advisory Circular, AC 120-40C, Tech. Rep., 1991.

[31] G. Balmer, "Modelling and Control of a Fixed-Wing UAV for Landings on the Mobile Platforms," German Aerospace Center (DLR), Robotics and Mechatronics Center, Tech. Rep., 10 2015.

[32] L. Persson, "Cooperative Control for Landing a Fixed-Wing Unmanned Aerial Vehicle on a Ground Vehicle," German Aerospace Center (DLR), Robotics and Mechatronics Center, Tech. Rep., 4 2017.

[33] NATO, *System Identification for Integrated Aircraft Development and Flight Testing (l'Identification Des Systemes Pour Le Developpement Integre Des Aeronefs Et Les Essais en Vol).* Defense Technical Information Center, 1999.

[34] R. Jategaonkar, R. Behr, W. Gockel, and C. Zorn, "Data analysis of phoenix reusable launch vehicle demonstrator flight test," *Journal of Aircraft*, vol. 43, no. 6, pp. 1732–1737, Nov 2006.

[35] D. Rohlf, "Global model approach for x-31 vector system identification," *Journal of Aircraft*, vol. 42, no. 1, pp. 54–62, Jan 2005.

[36] R. V. Jategaonkar, "Identification of actuation system and aerodynamic effects of direct-lift-control flaps," *Journal of Aircraft*, vol. 30, no. 5, pp. 636–643, Sep 1993.

[37] R. V. Jategaonkar, W. M-ograve, nnich, D. Fischenberg, and B. Krag, "Identification of speed brake, air-drop, and landing gear effects from flight data," *Journal of Aircraft*, vol. 34, no. 2, pp. 174–180, Mar 1997.

[38] A. C. Paris and M. Bonner, "Nonlinear model development from flight-test data for f/a-18e super hornet," *Journal of Aircraft*, vol. 41, no. 4, pp. 692–967, July 2004.

[39] T. L. Trankle and S. D. Bachner, "Identification of a nonlinear aerodynamic model of the f-14 aircraft," *Journal of Guidance, Control, and Dynamics*, vol. 18, no. 6, pp. 1292–1297, Nov 1995.

[40] G. Pezzella, G. Marino, and G. C. Rufolo, "Aerodynamic database development of the {ESA} intermediate experimental vehicle," *Acta Astronautica*, vol. 94, no. 1, pp. 57 – 72, 2014.

[41] J. Singh, A. Saraf, V. Patel, Basappa, and S. Tharewal, "Application of system identification techniques to tejas flight test data." *International Journal of Aerospace Innovations*, vol. 5, no. 1, pp. 11 – 18, 2013.

[42] M. Londono and B. Leonhardt, *Parameter Identification of an Executive Transport Aircraft - Simulation Update and Flight Test Results*, ser. Guidance, Navigation, and Control and Co-located Conferences. American Institute of Aeronautics and Astronautics, Aug 2012, 0.

[43] D. Kaliyari, K. N. TK, and J. Singh, "Validation and update of aerodynamic database at extreme flight regimes," in *SAE Technical Paper*. SAE International, 09 2015.

[44] O. Alaverdi and A. Paris, *Nonlinear aerodynamic model extraction from flight test data for the S-3B Viking*, ser. Guidance, Navigation, and Control and Co-located Conferences. American Institute of Aeronautics and Astronautics, Aug 2001, 0.

[45] K. Neville and A. Stephens, *Flight update of aerodynamic math model*, ser. Guidance, Navigation, and Control and Co-located Conferences. American Institute of Aeronautics and Astronautics, Aug 1993, 0.

[46] E. A. Morelli and J. Cooper, "Frequency-domain method for automated simulation updates based on flight data," *Journal of Aircraft*, vol. 52, no. 6, pp. 1995–2008, Jul 2015.

[47] C. R. Paez, "Simulation of high altitude long endurance platforms," German Aerospace Center (DLR), Robotics and Mechatronics Center, Tech. Rep., 6 2017.

[48] "Avl website," http://web.mit.edu/drela/Public/web/avl/, accessed: 2017-05-01.

# Appendix A

# Supplementary materials

This appendix includes more results.

## A.1 More results on Elektra 1 path reconstruction

This section includes the supplementary materials from Elektra 1 path reconstruction. The bias estimation from offline IEKS is shown in figure A.1.

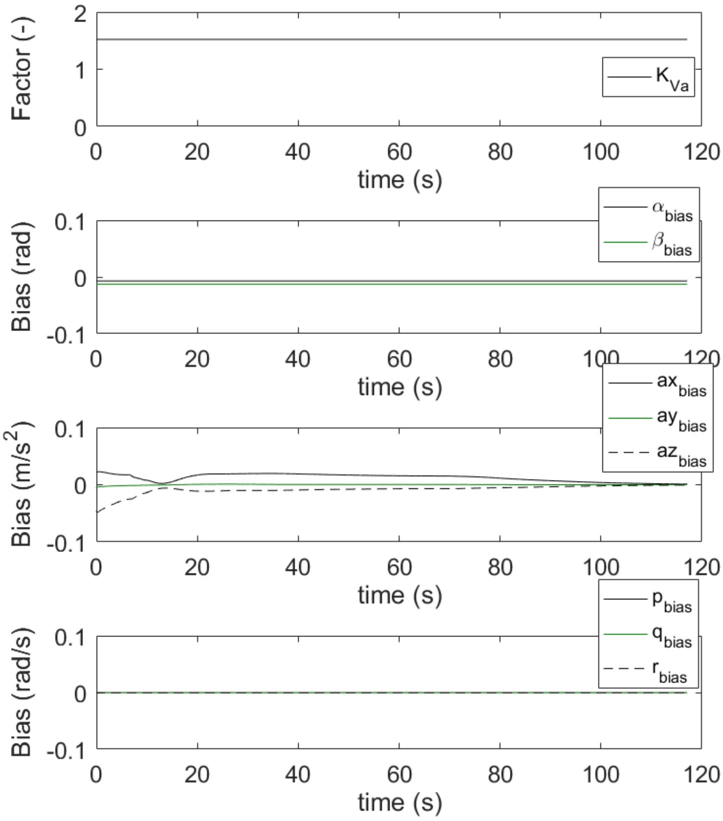

Figure A.1: Bias estimation from offline IEKS.

## A.2 Penguin BE UAV local system identification

This section includes the supplementary materials from Penguin BE local system identification.

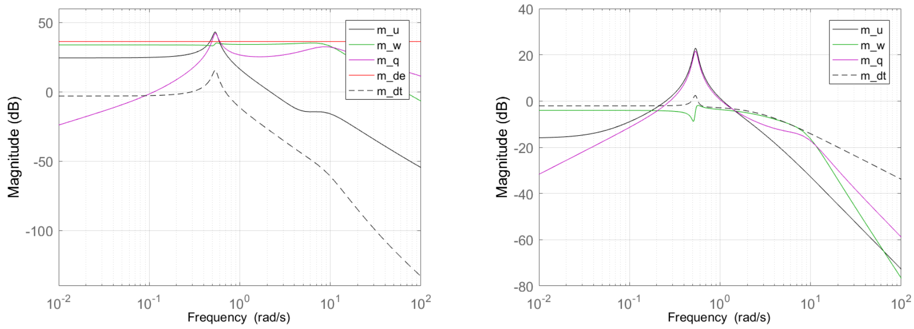

Figure A.2: Pitching moment derivatives w.r.t elevator (left) and throttle (right)

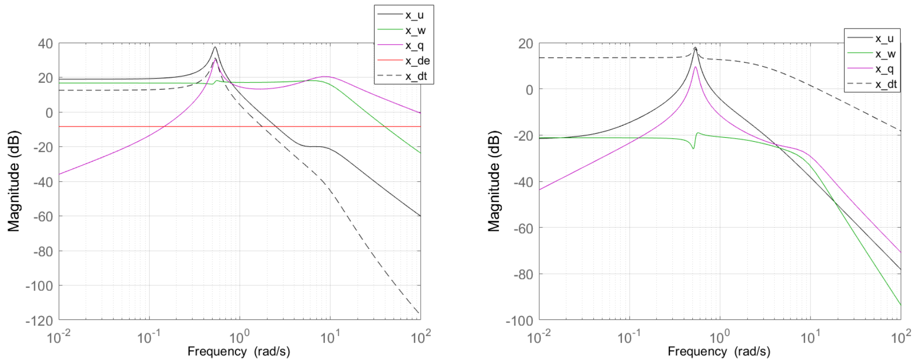

Figure A.3: X-axis force derivatives w.r.t elevator (left) and throttle (right)

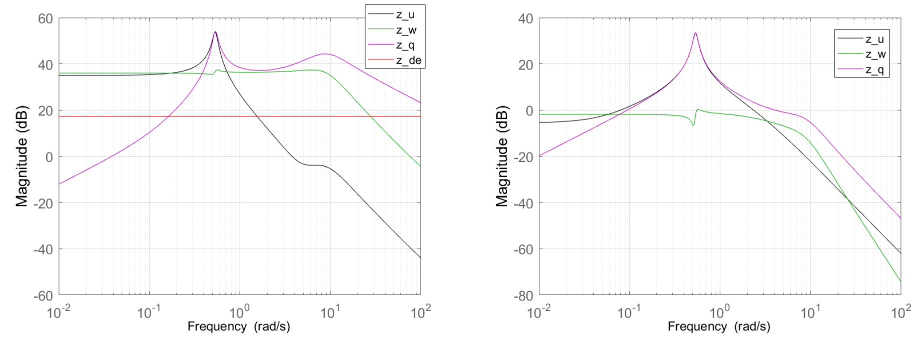

Figure A.4: Z-axis force derivatives w.r.t elevator (left) and throttle (right)

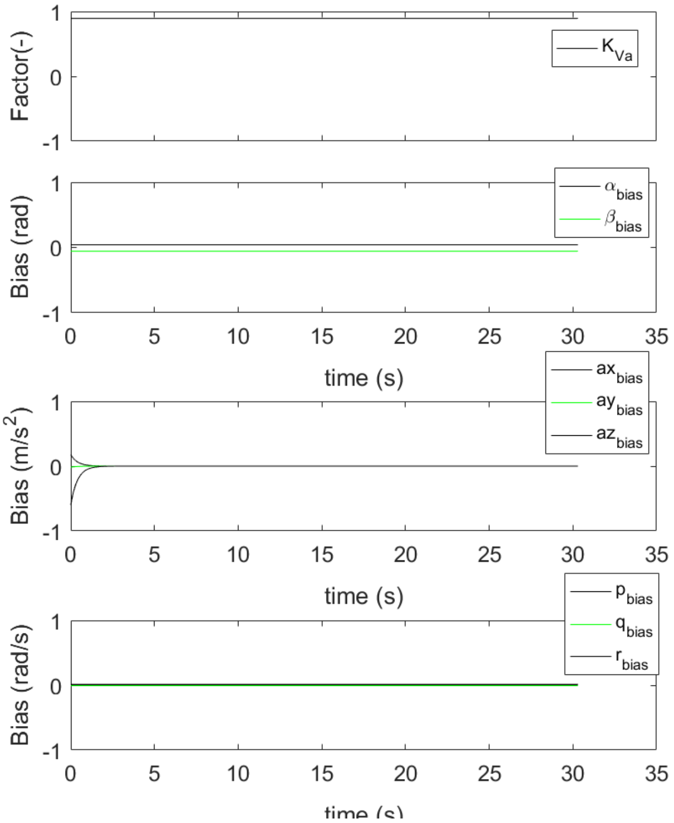

Figure A.5: Bias estimation from offline IEKS.

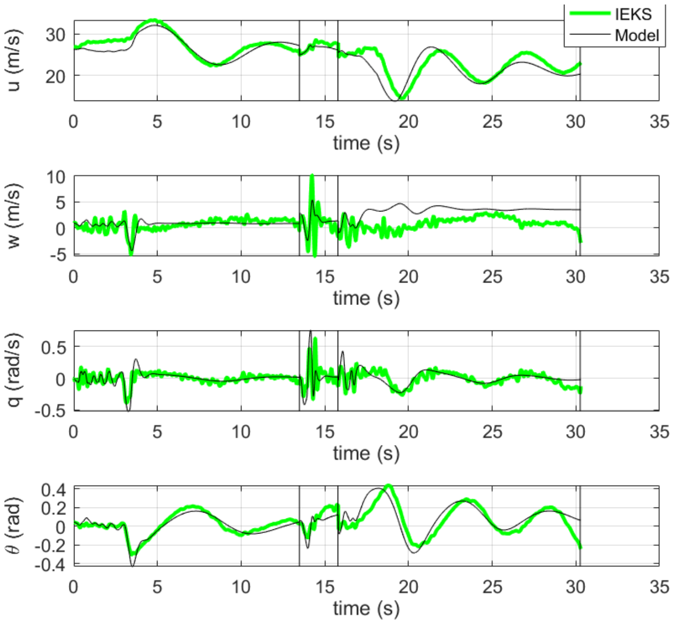

Figure A.6: Validation of offline IEKS estimation using aircraft equations of motion - nonlinear aerodynamic model.

# Appendix B

# Project definition

Within flying robots group at Institute of Robotics and Mechatronics(DLR), research has been focusing on fixed-wing solar electrical platforms capable of perpetually flying in stratosphere. These platforms, often called high altitude pseudo satellites (HAPS) have a wide range of applications ranging from mobile communication networks to long term observations and environmental measurements. This master thesis will involve aircraft system identification for such solar electrical platforms both at low and high altitude. Note that the table B.1 contains formal information about the current external master thesis.

Table B.1: General information

| | |
|---|---|
| Type | External master thesis |
| Start date | 01-10-2016 |
| End date | 15-04-2017 |
| Internal institute | Autonomous Systems Laboratory - ETH Zurich |
| External institute | Institute of Robotics and Mechatronics - DLR |
| Student | Jongseok Lee |
| Internal supervisor | Oettershagen Philipp<br>Thomas Statsny |
| External supervisor | Dr.-Ing. habil. Konstantin Kondak<br>Tin Muskardin |
| Supervising lecturer | Prof. Roland Siegwart |
| Tutor | Prof. Raffaello D'Andrea |

## Thesis description

The flying robots group is currently working in close cooperation with Elektra UAS GmbH and SolarXplorers SA (Solarstratos project) on highly efficient drives, avionics components, as well as payloads and autonomy functionalities for autonomous and optionally piloted solar high-altitude platforms and missions. Currently, these autonomy functionalities use flight dynamics model from geometry based approach where the aerodynamic database is created using the vortex lattice method(VLM) [3]. However, low fidelity of such flight dynamics model limits its usage for control synthesis and other developments of autonomy functionalities. Therefore, the top level requirement of the project is the high fidelity modelling of aircraft dynamics with the following goals.

**TR1** The aircraft model shall allow for the control synthesis.

**TR2** The aircraft model shall allow for the simulation of entire stratospheric mission (optional).

In line with above mentioned requirements the scope of the current project is defined to following work packages.

**WP1** Local aircraft system identification for three manned/unmanned aircraft - Penguin and Elektra 1 (bonus).

**WP2** Global aircraft system identification via incremental model update.

**WP3** Development of adaptable aircraft system identification procedures and tool chains for various platforms.

Note that local aircraft system identification refers to the identification of aerodynamic parameters that is valid over one point in the flight envelope where the data is collected whereas the global aircraft model is valid over the entire flight envelope.